# Characterisation of the first p-type Segmented Inverted-coaxial Germanium Detector, SIGMA

Thesis submitted in accordance with the requirements of
the University of Liverpool for the degree of Doctor in Philosophy

by

Fiona Jane Pearce

December 2020

# Abstract

The Segmented Inverted-coaxial GerMAnium (SIGMA) detector is a large volume High Purity Germanium (HPGe) gamma-ray detector that aims to demonstrate superior energy and position resolution over other large volume segmented germanium detectors. The SIGMA prototype detector is the first p-type detector of its kind to be produced. Due to the low noise of the point contact, the SIGMA detector can provide excellent energy resolution and, through the use of Pulse Shape Analysis (PSA), excellent position resolution. Accurate and precise energy and position determination are the key factors in effective gamma-ray tracking making SIGMA particularly suited for use at Radioactive Ion Beam (RIB) experiments such as DESPEC.

The SIGMA prototype detector has been characterised and tested at the University of Liverpool. SIGMA showed excellent energy resolution with the point contact achieving 0.89 keV at 122 keV and 2.21 keV at 1332 keV and a relative efficiency of 40.9%. A collimated beam of $^{241}$Am and $^{137}$Cs gamma rays were scanned across the detector in 1 mm steps to investigate the crystal size, structure and position and the active area of the individual segments. The $^{241}$Am data was used to produce a risetime matrix displaying the change in drift time across the front face of the crystal.

The detector was also operated alongside BGO detectors in coincidence mode and data acquired using the $^{137}$Cs beam to investigate pulse shape behaviour in the crystal at a range of positions. The pulses from all functioning segments were collected, including both real charge and image charge pulses, and used to produce an average response from each segment for individual x-y-z locations in the crystal. The average pulses were compared to investigate the position response of the detector. A measurable difference in pulse shape was seen in multiple segments for a separation of as little as 2 mm in one dimension.

# Contents

# List of Equations



# List of Figures

# List of Tables

# 1 Introduction

High-purity germanium detectors are a key component of gamma-ray spectroscopy for the study of nuclear structure. Following a nuclear reaction or decay, the nucleus is often left in an excited state from which it can release energy, in the form of a gamma-ray photon, to move between two quantum states and approach its ground state. Spectroscopy of these gamma rays offers information on the nuclear states, such as excitation energy, lifetime and transition probability. The development of radioactive ion beam facilities, such as the Super-FRS fragment separator [G$^+$03] at the Facility for Antiproton and Ion Research (FAIR) [FAI18a], offers the ability to study a wider range of unstable nuclei at the cost of lower production cross sections, large Doppler broadenings and high backgrounds. The lower production cross sections means detection efficiency will play a key role, requiring not only a large active volume and solid angle coverage but also additional techniques to reduce the amount of events lost. One such experiment is DESPEC, to be located on the low-energy branch of the Super-FRS facility at FAIR, which will include a germanium spectrometer array DEGAS [DCG$^+$17]. DEGAS will move through 3 design phases; Phase 1 using EUROBALL crystals, Phase 2 using AGATA type detectors and Phase 3 to be the result of ongoing development in the field of gamma-ray detection [DCM$^+$15]. Due to the rapid advancement of the field of nuclear structure, the technology involved in spectroscopy is constantly moving forward to meet the needs of research. The objective of this thesis is to evaluate a prototype Segmented Inverted-coaxial GerMAnium (SIGMA) detector, in the context of its potential application in DEGAS.

## 1.1 Germanium Detector Arrays

Large spherical detector arrays for gamma-ray spectroscopy, such as EUROBALL [Sim97] and GAMMASPHERE [Lee90], were designed as escape suppressed arrays of High-purity germanium (HPGe) detectors, surrounded by Bismuth Germanate (BGO) shields. The germanium detectors are operated in anti-coincidence with the BGOs to remove scattered events where only a fraction of the full energy of the photon is deposited in the germanium detector volume. Any events which are seen in both the germanium crystal and the BGO shields are assumed to be partial energy events and removed. This is an effective way of increasing the peak-to-total ratio, but limits the

overall efficiency of these arrays by limiting the solid angle which can be covered by germanium.

The limitation on solid angle can be overcome by the AGATA spectrometer [A$^+$12] design, which will consist of 180 electrically segmented, high-purity coaxial germanium crystals which fit together to form a $4\pi$ sphere of detectors. The detectors are housed in triple cluster cryostats, with each crystal being one of three asymmetrical, hexagonal geometries; this asymmetrical design optimises the solid angle coverage of germanium. The outer contact of each crystal is segmented into 36 regions, resulting in 37 electrical channels per crystal. AGATA uses several processing methods to improve its intrinsic characteristics such as Pulse Shape Analysis (PSA) and Gamma-Ray Tracking (GRT). PSA is used to gain position information from the shape of charge collection pulses. The location of an interaction affects the resultant pulse shape both for the charge collecting electrode and, in segmented detectors, the transient charges induced on the other contacts as the charge moves through the crystal. The expected pulse shape for each contact at each x-y-z location can be simulated using the crystal geometry to produce a pulse shape database. Experimentally measured pulses can then be compared to this database to find the closest fit and as such the position of the interaction. This can greatly improve the position resolution beyond detector segmentation alone allowing AGATA to to achieve a position resolution FWHM of 4 mm [S$^+$11].

GRT aims to reconstruct the path of a photon through the detector volume. When a gamma ray enters the active volume of a detector it may scatter multiple times before being fully absorbed. Considered individually these interactions each deposit a fraction of the full energy of the gamma ray and the event would be lost as background. By correctly identifying which interactions belong to a single event, the sequence can be reconstructed and the full energy found. This offers an increase in efficiency, particularly at energies where there is a higher probability of scattering. AGATA's closely packed crystals mean that gamma rays can be tracked both within a crystal and between neighbouring crystals, increasing its efficiency over escape suppressed arrays. This combination of PSA and tracking also gives AGATA the ability to determine the direction of origin of incident radiation, allowing the system to disregard photons from other directions, reducing the background.

There are many types of GRT algorithms such as forward tracking [LMHK$^+$04] and backtracking [vdMC99]. Many of these algorithms look at each interaction and determine the probability of scattering at the angle of the other interaction points. Using the energy deposited and the position of each iteration, the most probable path is reconstructed. As such the effectiveness of GRT depends on the position and energy resolution of the detector.

A next generation germanium detector array will need increased efficiency to cope with the lower production cross sections of radioactive ion beam facilities. This will

require maximising the germanium solid angle coverage and improving the implementation of GRT to reconstruct events. This dependence on GRT means next generation germanium detector arrays will require superior energy and position resolution. Ideally this would be achieved without increasing the number of electrical channels and complexity of the system which ultimately result in an increase in cost.

## 1.2 SIGMA Design

The Segmented Inverted-coaxial GerMAnium detector (SIGMA) is designed to offer both excellent position and energy resolution, with the goal of advancing GRT capabilities in large germanium arrays. Similar in shape to standard closed-end coaxial detectors, SIGMA has a central bore hole allowing for full depletion of the crystal volume at a reasonable voltage of a few thousand volts; though, in the case of this inverted-coaxial, the bore hole is located at the front of the crystal with a diameter of 10 mm and continues 55 mm into the crystal bulk. The crystal has a maximum diameter of 70 mm and is 80 mm long with the front end of the crystal tapered at an angle of 10° starting 20 mm from the rear. An illustration of these dimensions is given in Figure 1.1.

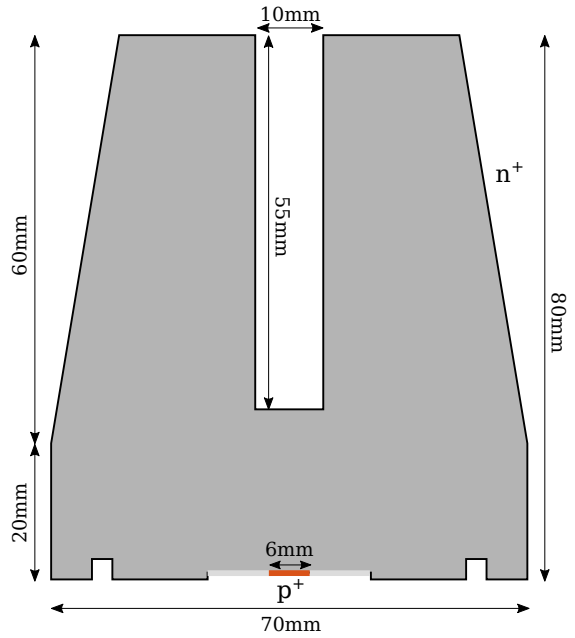


*Figure 1.1: Illustration of the dimensions of the SIGMA crystal with the point contact shown in red.*

SIGMA has a $p^+$ point-like contact in the centre of the closed end of the detector surrounded by a 9 mm passive region, with the remaining detector surfaces, including the bore, acting as the $n^+$ contact. The small physical size of the point contact offers reduced capacitance, resulting in low series noise and precision energy resolution, par-

ticularly at low energies. This unique electrode configuration gives a charge collection profile with long drift times related to gamma-ray interaction position. Whilst slow drift times increase the probability of trapping and recombination, they also allow for additional position resolution to be gained due to strong variations in drift time across the detector volume, creating measurable differences in the pulse shapes of charges created in close spatial proximity.

The electrical segmentation scheme of the outer contact has been designed to offer optimal positioning whilst keeping the number of electrical channels, and as such system complexity, minimal [CRHL11]. There are 19 segments in total, including 8 azimuthal, 8 longitudinal, 2 radial and the core, as shown in Figure 1.2. The outer contact will be used to identify gamma-ray interaction times and examine image charges. When charge is created within the detector volume it drifts towards the appropriate collecting electrodes, creating image charges in neighbouring segments. Due to the geometry of SIGMA, charges may pass by multiple segments on their way to the point contact, creating image charges in non-neighbouring longitudinal segments as well. Analysis of both drift and image charges through digital pulse processing and signal decomposition techniques allows for greater position sensitivity.

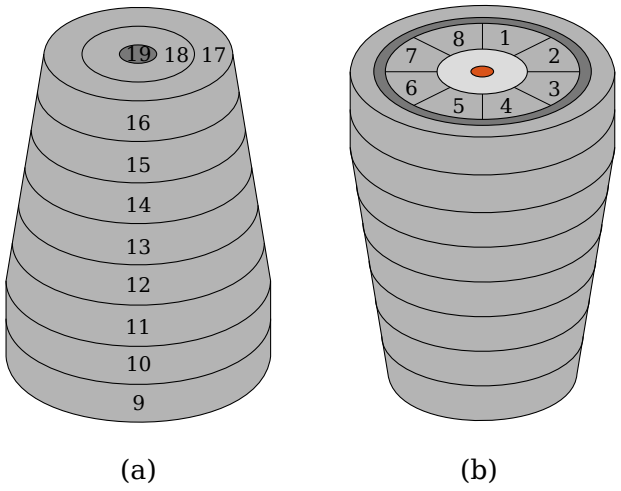


*Figure 1.2: Segmentation layout of the SIGMA crystal with (a) showing the longitudinal (9-16) and radial segments (17-18) on the front face of the crystal and the core (19) and (b) showing the azimuthal segments (1-8) at the rear of the crystal and the point contact in red.*

Simulations of the SIGMA design have been produced to estimate the position resolution that could be achieved. The simulated drift time as a function of interaction position is shown in Figure 1.3, with the isochrones representing intervals of 50 ns. At the front of the crystal the isochrones are spaced further apart indicating a slower change in drift time with position compared to areas with tighter packed isochrones, such as around the base of the well. This shows that the position resolution will

vary over the detector volume with areas of faster change resulting in better position resolution.

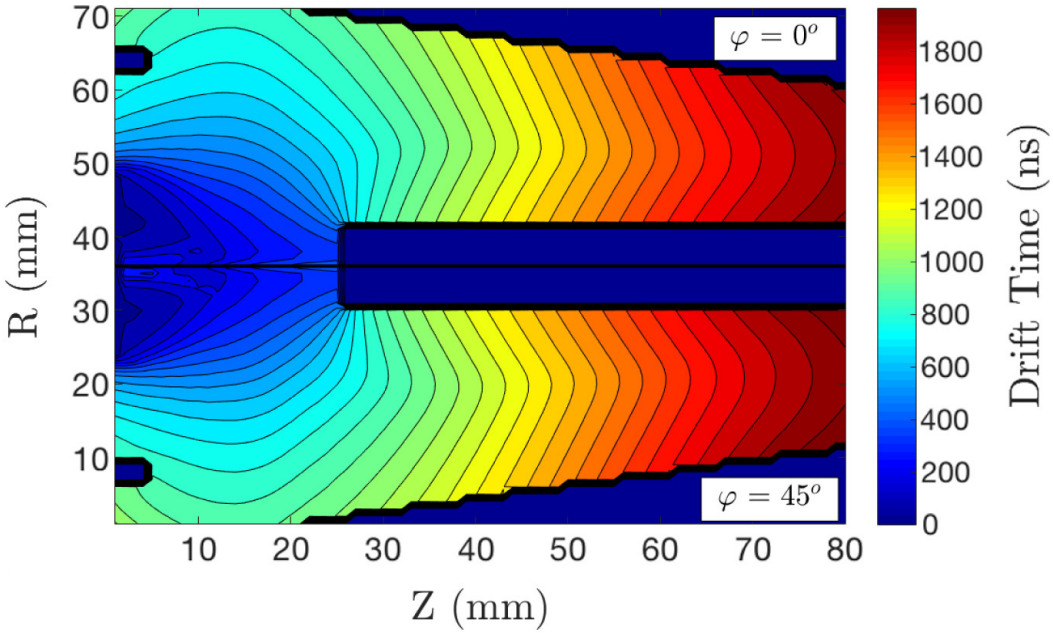


*Figure 1.3: The simulated drift time as a function of gamma-ray interaction position taken from [WHBB+18]. The lines represent 50 ns isochrones.*

### 1.2.1 SIGMA Prototype Detector

The SIGMA prototype detector is the first p-type segmented inverted-coaxial germanium detector to be produced. The crystal is housed in a cylindrical cryostat with a diameter of 100 mm, as seen in Figure 1.4. The prototype represents the first attempt at a novel detector design, as a result the manufacturing process included research and development involving multiple reprocessing cycles of the crystal. Due to this, the prototype detector differs slightly to the original design. The final prototype crystal has a reduced volume of 4.9 % from the original based on the initial and final weights. This reduction in size reduces the efficiency and the space available between segments leading to the combination of segments 18 and 19 which share a single readout referred to as segment 19; as such the detector has a total of 19 electrical channels.

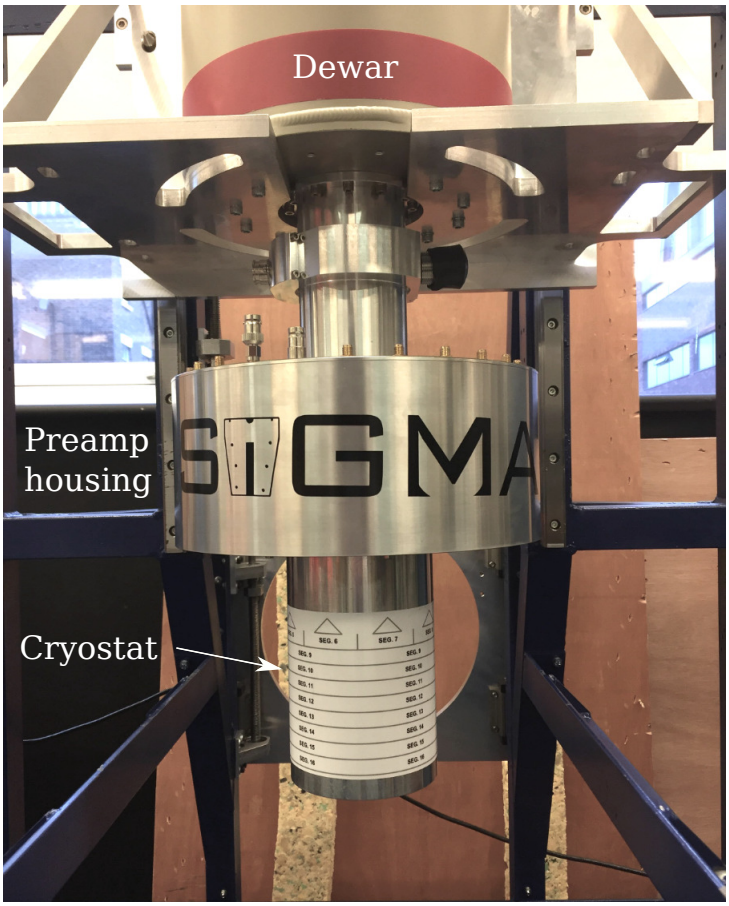


*Figure 1.4: Photograph of the SIGMA prototype detector.*

An n-type segmented Inverted Coaxial Point-Contact (ICPC) detector has been produced with a similar design to the SIGMA detector [SCC+17]. While it is also predicted to achieve sub mm position resolution, initial characterisation revealed poor intrinsic energy resolution due to charge trapping [SCC+17]. As holes are less susceptible to trapping than electrons it is predicted that trapping will have less of an effect on the energy resolution of the SIGMA detector [Koh12]. This will result in SIGMA having similar position resolution and superior energy resolution to the ICPC detector.

## 1.3 Thesis Overview

The SIGMA detector aims to improve upon currently available germanium gamma-ray detectors by combining new technology with existing methods. This work focuses on characterising the first prototype SIGMA detector. This includes quantifying the energy resolution and efficiency of the detector as well as determining the size and location of the crystal, including the active area of each segment. Data were collected to produce an experimental pulse shape database to aid in the creation of a simulation of the SIGMA detector.

Chapter 2 of this thesis focuses on the operational principles of germanium detectors in gamma-ray detection and the initial spectroscopic performance of SIGMA. Chapter 3 gives a description of the experimental scanning system and singles measurements including details of the geometry of the crystal. Chapter 4 discusses the acquisition and analysis of the coincidence measurements and finally Chapter 5 gives a summary of the overall performance of the first prototype SIGMA detector.

# 2 Operational Principles and Performance of SIGMA

In order to utilise Gamma-Ray Tracking (GRT) techniques, SIGMA needs both the energy deposited in a gamma-ray interaction and the ability to identify the position of the interaction using a pulse shape database. Pulse Shape Analysis (PSA) is reliant on different pulse shapes being produced by interactions in different areas of the detector. To determine how the pulse shapes are affected by the location of the interaction it is vital to have a thorough understanding of how a signal is produced following a gamma-ray interaction. This chapter covers the theoretical principles of charge collection in SIGMA and the first experimental gamma-ray spectroscopy measurements with the SIGMA prototype detector.

The energy resolution at 122 keV and 1332 keV was determined for each segment and compared to the pre-agreed acceptance criteria for the detector. Efforts were made to optimise the electronics to determine the best possible energy resolution performance of the detector. Detector absolute efficiency as a function of energy was also investigated.

## 2.1 Interaction of Gamma Rays with Matter

One of the potential applications of SIGMA is in nuclear decay experiments, such as DESPEC [Rub06], in which the gamma-ray energy range of interest lies between 100 keV to 2 MeV. In this energy range, three main mechanisms dominate gamma-ray interactions; these are photoelectric absorption, Compton scattering and pair production, as depicted in Figure 2.1.

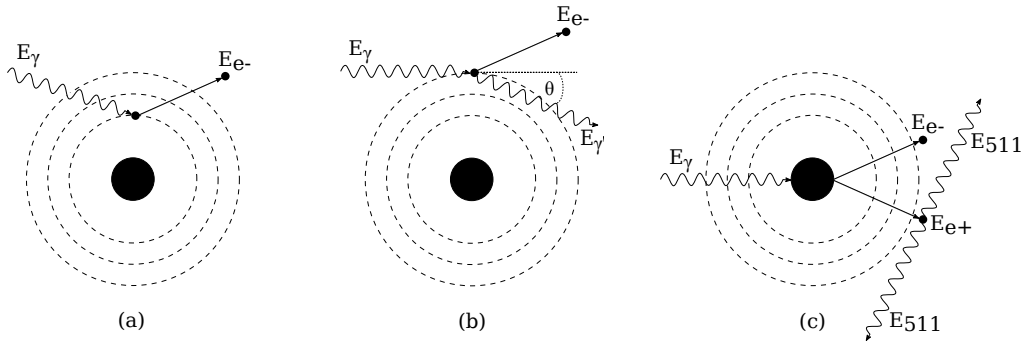


*Figure 2.1: Schematic illustration of (a) photoelectric absorption, (b) Compton scattering and (c) pair production.*

Each of these interaction processes affects the incident gamma rays by either absorption or scattering. The probability of each interaction occurring is fixed per unit path length in the absorber material. The linear attenuation coefficient, $\mu$, describes the sum of the probability of each of these interactions per unit path length and is given by

$$\mu = \mu_{pe} + \mu_{cs} + \mu_{pp}. \tag{2.1}$$

This can also be expressed as the mean free path, which is the reciprocal of the linear attenuation coefficient, representing the average distance a gamma ray travels in a material before it interacts. The intensity of a beam of transmitted photons, $I$, will decrease exponentially with the thickness of the absorber material, $t$, where the rate of exponential decrease is controlled by the linear attenuation coefficient as given by

$$I = I_0 e^{-\mu t}, \tag{2.2}$$

where $I_0$ is initial intensity.

### 2.1.1 Photoelectric Absorption

In photoelectric absorption the incident gamma-ray photon imparts its full energy to a bound atomic electron. The electron, known as a photoelectron, is ejected from its electron shell, as depicted in Figure 2.1 (a), with a kinetic energy, $E_{e-}$, equal to the incident photon energy, $E_\gamma$, minus the binding energy of the electron, $E_b$,

$$E_{e-} = E_\gamma - E_b \tag{2.3}$$

This equation assumes the atom has no recoil. Whilst the conservation of momentum requires the atom to have some recoil, it is usually small enough to be considered

negligible. For typical incidence energies, photoelectrons are most likely to be produced in the most tightly bound K shell. For germanium this results in a binding energy of 12 keV.

When the photoelectron is ejected, a vacancy is created in the electron shell, which is quickly filled by rearrangement of the outer shell electrons or the capture of a free electron, releasing binding energy in the form of a characteristic X-ray. These X-rays can be reabsorbed through photoelectric absorption with less tightly bound shells or may escape the detector volume, degrading measured energy. Photoelectric absorption is the dominant interaction mechanism at low energies, particularly in high atomic number, Z, absorber materials. The probability of photoelectric absorption per atom, $\tau$, can be approximated using,

$$\tau\alpha\frac{Z^n}{E_\gamma^{3.5}} \tag{2.4}$$

where n varies between 4 and 5 depending on incident gamma-ray energy, $E_\gamma$ [Kno10], [Eva55].

### 2.1.2 Compton Scattering

Compton scattering is the process whereby an incident gamma ray imparts a fraction of its energy to a weakly bound electron, causing scattering at an angle $\theta$ from its incident direction as illustrated in Figure 2.1 (b). Energy imparted to the recoil electron is dependent on the scattering angle, which can range from a minimum at $\theta = 0$ to a maximum at $\theta = \pi$. The conservation of energy and momentum dictates the energy of the scattered gamma ray, $E_{\gamma'}$, is fixed for any set angle and incident photon energy, given by

$$E_{\gamma'} = \frac{E_\gamma}{1 + \frac{E_\gamma}{m_0c^2}(1 - cos\theta)}, \tag{2.5}$$

where $m_0c^2$ is the rest mass energy of the recoil electron (511 keV). In practice scattering will occur at all angles, resulting in a Compton continuum in the produced gamma-ray energy spectrum as illustrated in Figure 2.2. The angular distribution of scattered gamma rays can be predicted using the differential cross section $\frac{d\sigma}{d\Omega}$, given by the Klein-Nishina formula

$$\frac{d\sigma}{d\Omega} = Zr_0^2\left(\frac{1}{1+\alpha(1-cos\theta)}\right)^2\left(\frac{1+cos^2\theta}{2}\right)\left(1+\frac{\alpha^2(1-cos\theta)^2}{(1+cos^2\theta)[1+\alpha(1-cos\theta)]}\right), \tag{2.6}$$

where $r_0$ is the electron radius, $\sigma$ is cross section, $d\Omega$ is solid angle subtended by the detector and $\alpha \equiv \frac{E_\gamma}{m_0 c^2}$. Figure 2.3 displays a polar plot for several incident photon energies, showing that as energy increases the distribution becomes forward focused. As mentioned previously the energy range of interest for SIGMA is 100 keV - 2MeV where, as can be seen from Figure 2.3, scattering will be mostly forward focused.

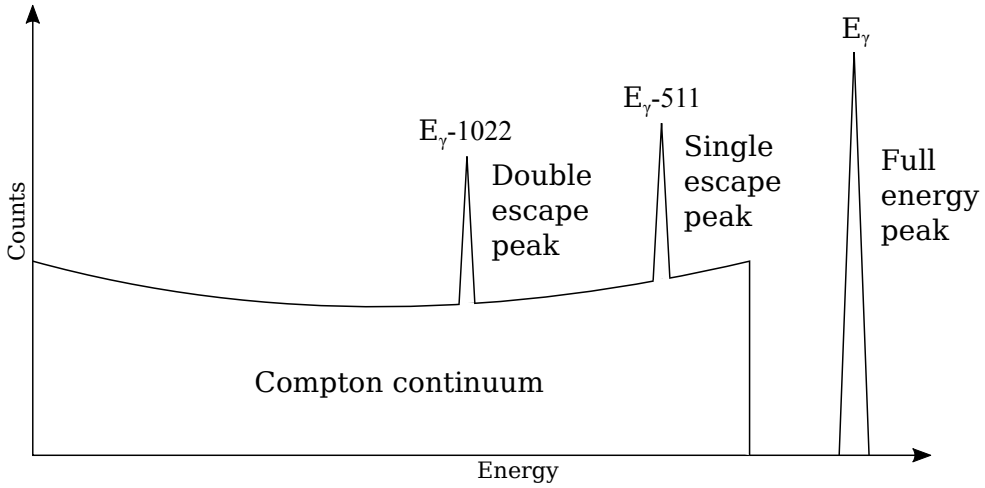


*Figure 2.2: Simplified figure showing the effects of Compton scattering and pair production on an energy spectrum.*

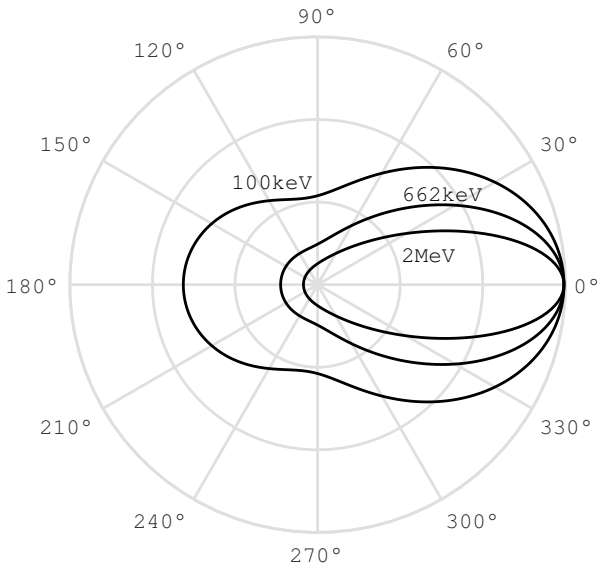


*Figure 2.3: Polar plot of the scattering angle of photons for given initial energies of 100keV, 662keV and 2MeV.*

### 2.1.3 Pair Production

For energies greater than 1022 keV, twice the electron rest mass energy, incident photons are capable of interacting by pair production. The probability of pair production only

becomes significant at energies of several MeV and it therefore is a minor contribution to spectroscopy in this thesis. In pair production, the photon disappears upon interaction with the Coulomb field of a nucleus, creating an electron-positron pair simultaneously. When the incident photon has energy greater than 1022 keV, any residual energy is shared as kinetic energy between the electron and positron. Positrons are quickly slowed down within material and undergo annihilation with free electrons, producing two annihilation photons of 511 keV each as shown in Figure 2.1 (c). Annihilation photons can escape the detector, resulting in single and double escape peaks in acquired gamma-ray energy spectra as illustrated in Figure 2.2.

## 2.2 The Germanium Detector SIGMA

Germanium is a widely used detector material in gamma-ray spectroscopy. Germanium detectors provide superior energy resolution compared to scintillation detectors, due to the significantly lower energy requirement for the creation of electron-hole pairs than photons, and their solid state offers far greater stopping power than gas detectors, making them more efficient per unit volume. The following sections describe how signals are generated from the germanium detector SIGMA as a result of gamma-ray interactions.

### 2.2.1 Band Structure

Solid crystalline materials have discrete atomic energy levels which form allowed energy bands for electrons within the material. The lower valence band represents bound outer-shell electrons, whilst the higher conduction band contains free electrons. Materials can be classified based on the size of the bandgap energy, the separation between valence and conduction bands, $E_g$, as either insulators, semiconductors or conductors, visualised in Figure 2.4.

Conductor materials have either overlapping bands or a valence band which is not completely filled, providing free electrons to carry charge. For insulators and semiconductors, energy bands are separated by forbidden energies, resulting in a fully occupied valence band and empty conduction band at 0K. The large band gap of insulator materials mean there is a very low probability of an electron gaining enough energy to enter the conduction band through thermal excitation. For low bandgap energy semiconductors, such as germanium where $E_g = 0.67$ eV, electron elevation across the bandgap by thermal excitation is possible at room temperature, causing leakage current. Cooling germanium detectors with liquid nitrogen is used to reduce this leakage current.

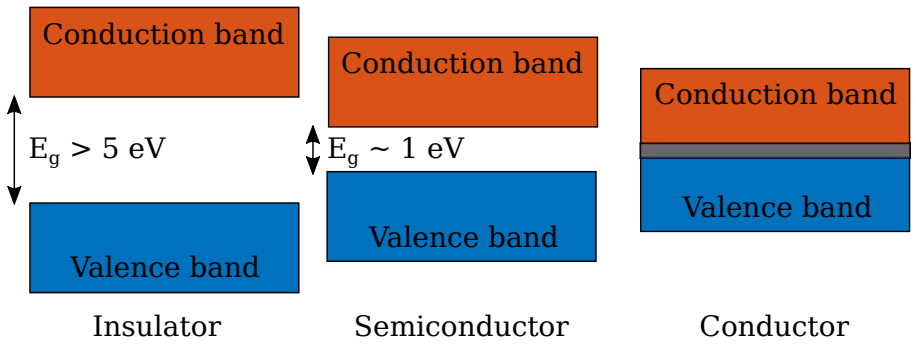


*Figure 2.4: Simplified band structure for insulators, semiconductors and conductors.*

### 2.2.2 Charge Carriers

The excitation of an electron across the bandgap leaves behind a vacancy in the valence band, known as a hole. Under an applied electric field, the excited electron and created hole will move in opposite directions, parallel to the field. When a gamma ray interacts with an atomic electron, the released electron will cause the creation of multiple electron-hole pairs as it loses energy via multiple ionisation events, resulting in a charge cloud; where the number of charge carriers created is proportional to the deposited energy. For germanium an average energy of around 3 eV is required to make one electron-hole pair. For gamma-ray detection, ideally all charge carriers would be collected, however in practice some are lost to trapping and recombination within the crystal volume before collection can occur. Trapping is caused by impurities in the crystal, which can hold a charge carrier for long enough to prevent it from contributing to the measured energy of that event. Recombination can happen anywhere in the crystal but is often caused by traps which can collect both electrons and holes, causing them to recombine. The probability of trapping and recombination increases as the time between charge creation and collection increases.

### 2.2.3 Doping

An intrinsic semiconductor is a pure material with the same number of electrons in the conduction band as there are holes in the valence band. In practice this is impossible to achieve and the electrical properties of the material are affected by small quantities of electrically active impurities that are present in the crystal despite purification processes. Doping involves the addition of trace impurities to modify the electrical properties of a semiconductor. There are two types of doped material, n and p type, which correspond to the addition of an impurity containing one extra, or one less valence electron than the semiconductor material as shown in Figure 2.5. Dopants will occupy sites within the crystal lattice and, in the case of a n-type material, have one electron which is not covalently bonded and may be released with little energy; this creates a conduction electron not paired with a hole. For a p-type material, the lattice

site will contain one covalent bond left open which acts as a hole, though with slightly less binding energy than a normal hole as there is only one bond available. As germanium is tetravalent, the addition of a pentavalent dopant will result in a n-type donor material with additional loosely bound electrons; the addition of a trivalent dopant would result in a p-type acceptor material with extra holes. In each case the charge carrier concentration is dominated by the dopant impurities, leading to majority and minority charge carriers. SIGMA is a p-type crystal so the majority charge carriers are holes which are collected by the point contact. The minority charge carrier electrons are collected by the outer segments.

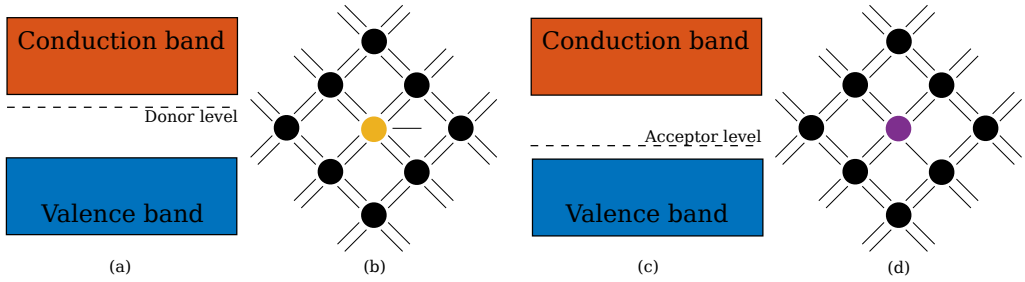


*Figure 2.5: Donor (a) and acceptor (c) levels and representations of a donor (b) and acceptor (d) impurity occupying a site in the crystal lattice.*

### 2.2.4 P-N Junction

Germanium detectors are operated as p-n junctions, which are formed when p-type and n-type materials are brought together in good thermodynamic contact. When first brought into contact, charge carriers diffuse across the junction from areas of high concentration to areas of low concentration. As electrons migrate from the n-type material to the p-type material they recombine with holes; this diffusion builds up a net negative space charge on the p-type side of the junction and a net positive space charge on the n-type side. The space charge creates an electric field preventing further diffusion across the junction and creates a steady state charge distribution with the charge imbalanced region extending into both sides of the junction termed the depletion region as illustrated in Figure 2.6. Build-up of net charge in the depletion region results in an electric field over the region, drawing electron-holes pairs created within the depletion region to the n-type and p-type material respectively. The electric field is not sufficient to prevent trapping and recombination and any signal measured would have a poor signal to noise ratio.

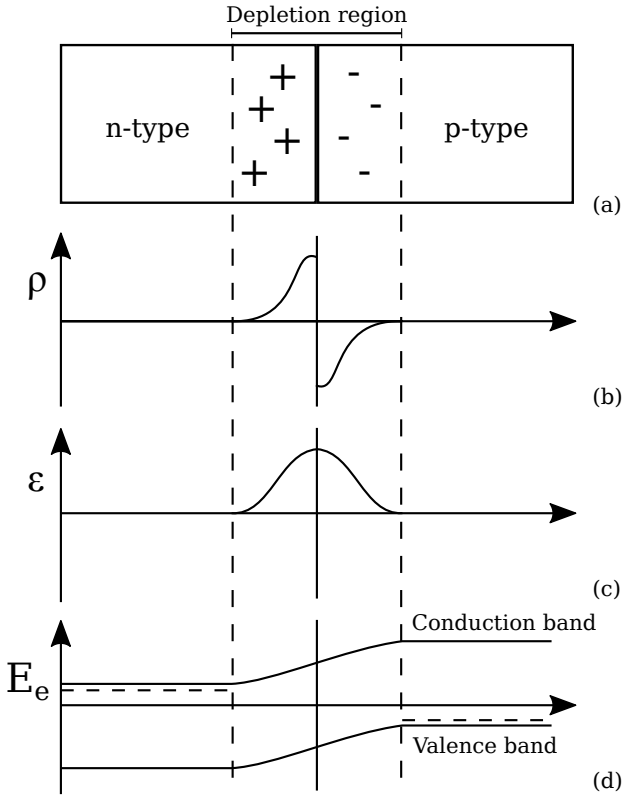


*Figure 2.6: A representation of the build up of space charge in an ideal p-n junction (a). The space charge density (b) and electric field (c) across the depletion region. The electron energy with position (d) showing the allowed energy states [Leo94].*

To increase the detector performance of a simple p-n junction, an external voltage is applied. A forward bias, a positive voltage applied to the p-type side and a negative voltage to the n-type side, would attract the majority charge carriers across the junction, increasing conductivity and closing the depletion region. A reverse bias, a negative voltage applied to the p-type side and a positive voltage applied to the n-type side, attracts the minority carriers across the junction, resulting in a small current. The applied voltage appears across the depleted region due to its higher resistivity compared to the surrounding p-type and n-type material. This causes the space charge to increase and consequently the depletion region increases. Increasing the reverse bias voltage enough will result in a fully depleted detector, with further increases amplifying the electric field. As the depletion region acts as the active detector volume, full depletion is desirable, however large reverse biases may lead to breakdown.

## 2.3 Signal Generation in SIGMA

When a gamma-ray interacts in a germanium detector it creates multiple electron-hole pairs, which are free to move under the influence of an electric field. As soon as the charge starts to move towards an electrode, a signal is generated on that electrode

and continues until all the charge has been collected. There is no time delay between the creation of this free charge and the start of the generated signal. The time taken to fully collect the charge and the shape of the signal are therefore a reflection of the location of the interaction within the detector. As a segmented detector, SIGMA outputs multiple signals for each gamma-ray event and understanding how the position of the interaction affects these signals will allow for position information beyond that offered by segmentation alone.

### 2.3.1 Weighting Potential

The Shockley-Ramo theorem [He01] states that the current induced on an electrode is

$$i = qv.E_0(x), \tag{2.7}$$

where $q$ is the charge of the carrier at position $x$, $v$ is the velocity and $E_0(x)$ is the weighting field. This principle can also be expressed in terms of the total induced charge on the electrode, $Q$, by

$$Q = -q.\phi_0(x), \tag{2.8}$$

where $\phi_0(x)$ is the weighting potential. The weighting potential can be found by solving the Laplace equation for the geometry of the detector, assuming the charge collecting electrode has a unit potential, all other electrodes are set to zero and there is no other charge including trapped charge. By determining the difference in the weighting potential at the start and end of the charge carrier path, the weighting potential offers a simplified method of calculating the induced charge on an electrode. The induced charge as a function of time can be used to determine the output pulse shape.

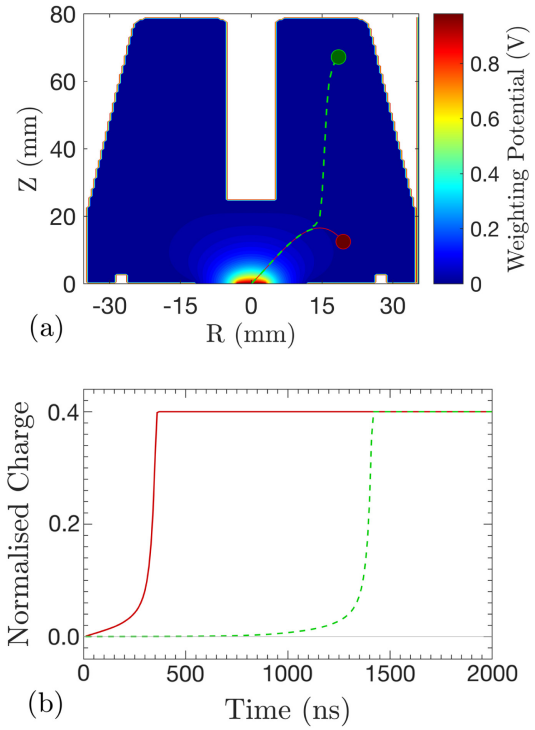


*Figure 2.7: The simulated weighting potential from the point contact of SIGMA (a) showing two example interaction positions in different areas of the crystal. The circles show the positions of interaction and the lines the hole drift paths. The example pulses (b) created by the interaction positions shown in (a). This figure is reproduced from [WHBB+18].*

SIGMA has a small point contact, which collects the primary charge carriers, and larger outer segment contacts which collect the secondary charge carriers. The size of the contact affects the weighting potential, with larger contacts having a larger area of high weighting potential. A simulated weighting potential and charge transport model for SIGMA are described and evaluated in [WHBB+18], produced using FieldGen and SigGen [R+21]. Due to the small size of the point contact, the weighting potential is virtually zero throughout most of the detector volume and rises rapidly close to the contact as seen in Figure 2.7 (a). This results in pulse shapes where the pulse amplitude rises sharply when charge is in close proximity to the point contact. Figure 2.7 (b) shows the simulated pulse shapes for two gamma-ray interactions in different areas of the crystal. They both display the sharp rise and a clear temporal difference with the interaction closest to the front of the crystal taking significantly longer to be collected. It is this clear distinction in pulse shapes produced by interactions in different areas of the crystal which will allow for the excellent position resolution predicted for SIGMA. An experimental pulse for the point contact is shown in Figure 2.8 showing similar pulse shape characteristics as the simulated pulses.

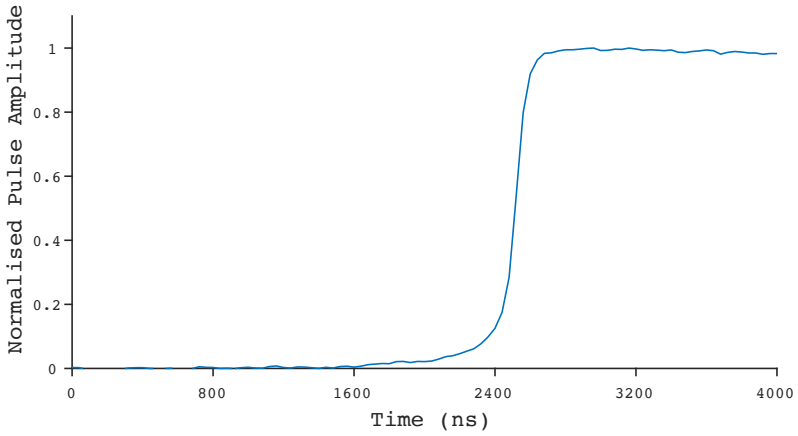


*Figure 2.8: An example preamplifier pulse recorded for the point contact of SIGMA.*

Weighting potentials calculated previously for the outer segments are shown in Figure 2.9. It should be noted that these simulations were produced for the original SIGMA design and so show Segment 18 which has been combined with Segment 19 in the prototype. Comparing Figure 2.7 and Figure 2.9 it can be observed that the weighting potential of the point contact has a much sharper increase close to the contact than the outer segments. This means that the pulse shapes for the outer contacts will not have the same fast rise in amplitude as the point contact.

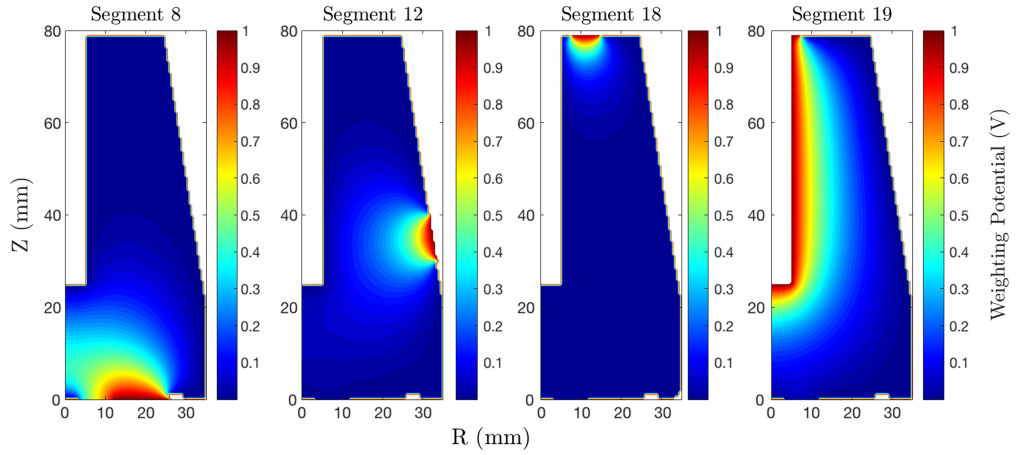


*Figure 2.9: Figure taken from [WHBB+18] showing the simulated weighting potential for segments 8, 12, 18 and 19 for the original SIGMA design.*

### 2.3.2 Image Charges

When charge is liberated following a gamma-ray interaction, the path it travels to its collecting electrode is dictated by the electric field lines in the detector. For a segmented detector, as charge travels through the detector volume, it may pass through the weighting field of other contacts. The variation in the weighting potential due to charge causes an induced charge, known as an image charge. As the charge is not

collected by the contact, the weighting potential is zero at the start and end of the charge carrier path meaning there is no net charge, resulting in a pulse shape similar to that seen in Figure 2.10. The size of the image charge produced is dependent on the energy of the interaction as well as its position and how close the charges pass by the contact.

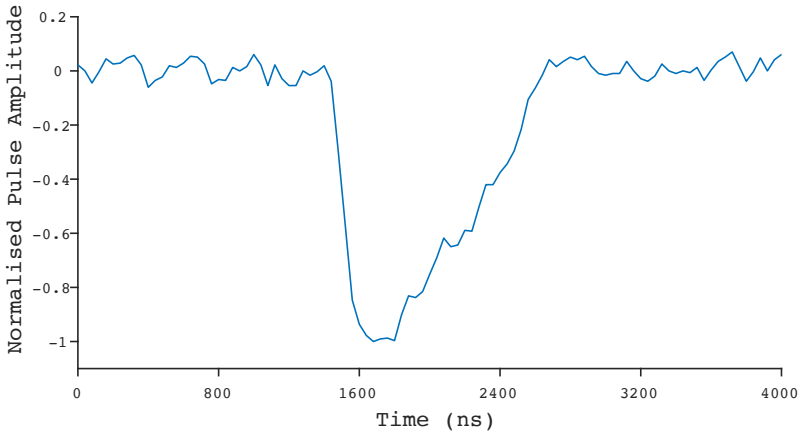


*Figure 2.10: An example image charge recorded for Segment 11 of SIGMA.*

SIGMA has 18 outer segment contacts giving the opportunity for multiple image charges to be created from a single gamma-ray interaction. The relative size and position of the image charges therefore provide comprehensive information on the charge collection path and the interaction position. The pulses recorded in every segment for an event can be displayed in the form of a superpulse, where each pulse is recorded in the same time period and plotted beside each other for complete observation. The superpulse is a simple way to view the charge response of each segment for a single event. A simulated superpulse is shown in Figure 2.11 for the original SIGMA design. Image charges are seen in every segment that does not collect charge.

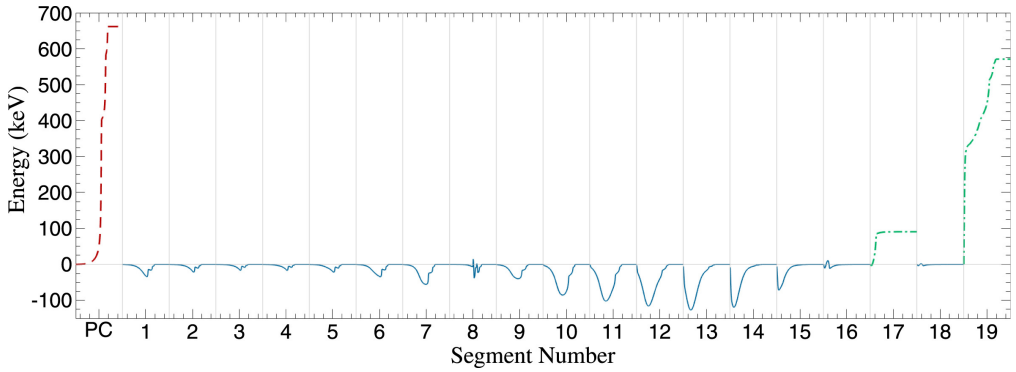


*Figure 2.11: Simulated superpulse showing the pulses seen in the point contact and every segment for a single event. Figure reproduced from [WHBB+18].*

## 2.4 Spectroscopic Performance of SIGMA

The detector was installed into a custom frame, allowing the detector to be mounted upright in the *front position* or at $90^o$ in the *side position*, as shown in Figure 2.12 (a) and (b) respectively. SIGMA was initially mounted in the *front position* with the liquid nitrogen dewar located above the detector, for ease of filling, and the front face of the detector closest to the floor.

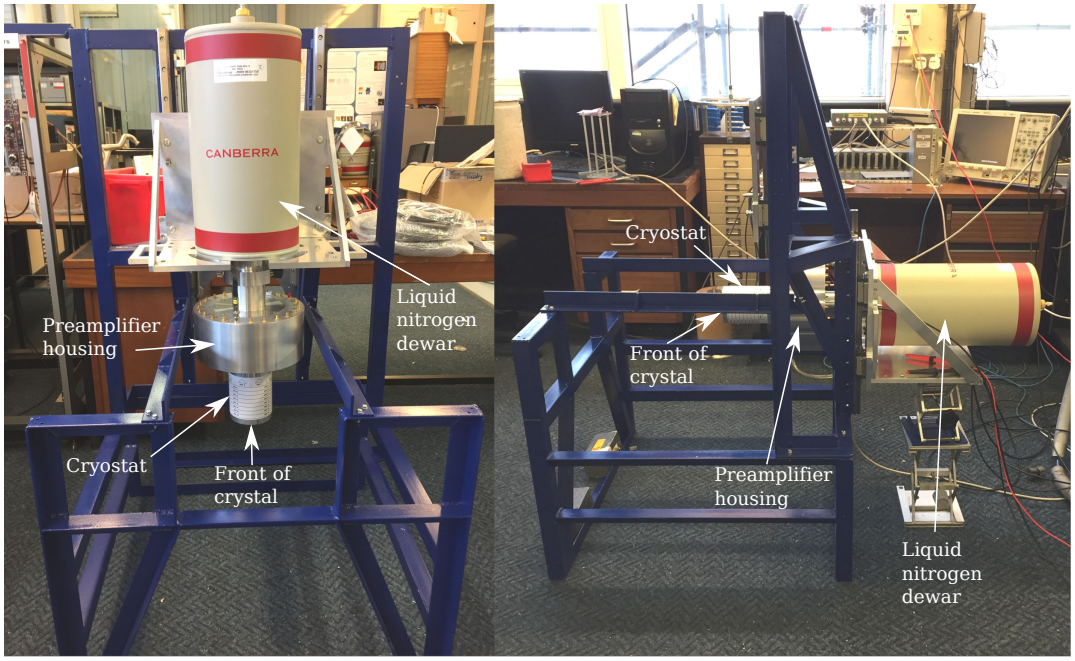


*Figure 2.12: Photographs showing SIGMA mounted in the frame in: (a) the front position and (b) the side position.*

On arrival from the manufacturer (Mirion technologies (Canberra) [Mir20]) in April 2018, the detector was cooled by filling the Dewar with liquid nitrogen over several hours [MIR18]. The cooling was monitored using a Platinum Thermistor (PT100). Figure 2.13 shows the temperature of the detector recorded over time until an operating temperature of -181$^o$C (92 K) is reached. Having reached operating temperature, the detector was left overnight to stabilise before any voltage was applied.

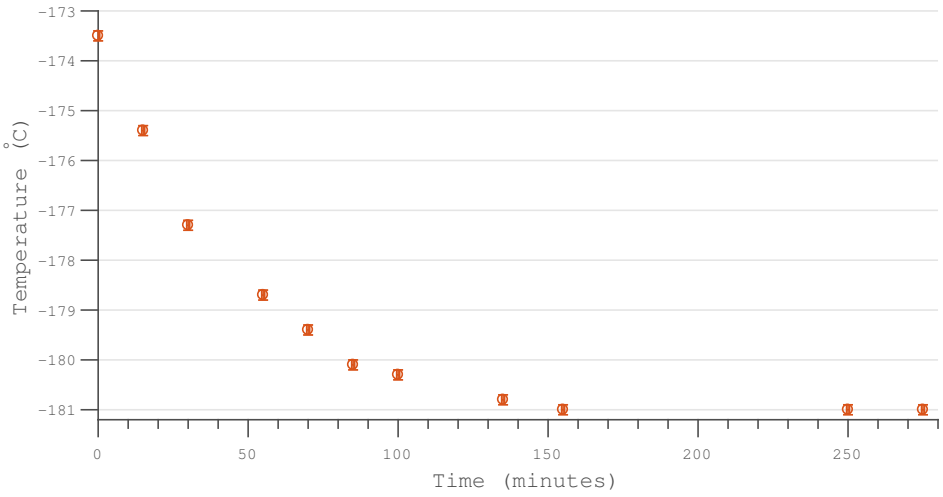


*Figure 2.13: Temperature measured by the PT100 as the detector was cooled.*

Once stabilised, a voltage could be applied across the detector using a bias supply, with a bias shut-down to protect the detector in the event of a cooling failure. Initially a signal response was seen in all 19 channels, using a digital oscilloscope, at a bias voltage of 0 V. The voltage was slowly increased to the recommended operating voltage of -2500 V in 100 V steps monitoring the noise in the point contact. Figure 2.14 shows that the crystal reaches full depletion at $\sim$ -1000 V, the additional voltage applied above this at the operating voltage serves to increase the electric field strength within the detector. The peak-to-peak noise at full bias was observed to be 4-10 mV across all channels, with the point contact being 4 mV.

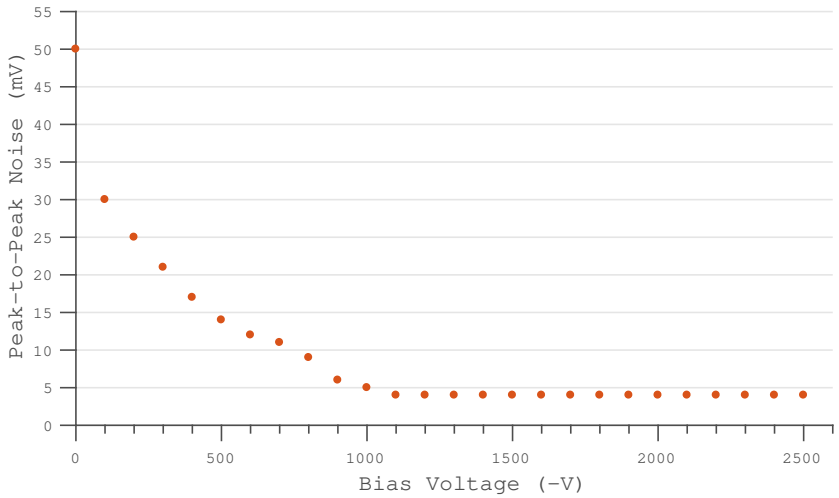


*Figure 2.14: The peak-to-peak noise of the point contact as a function of bias voltage.*

## 2.5 Energy Resolution

Each preamplifier output from SIGMA was connected to a Canberra 2026 spectroscopy amplifier. This in turn was connected to an Ortec 927 Multi Channel Analyser (MCA) for acquisition of energy spectra using Maestro [AME20]. The energy resolution of each channel was measured individually, with no other channels connected to obtain the best possible results and the resulting spectra analysed using GF3 [Rad18].

Data were acquired using $^{57}$Co and $^{60}$Co gamma-ray sources, of activity 0.033 MBq and 0.279 MBq respectively, to measure energy resolution for each output. The sources were placed so as to keep the count rate $\leq 1$ kHz, minimising the dead time contribution. To reduce acquisition time the sources were moved to be in line with the segment being measured, for example, the sources were placed at the front of the detector to measure segments 17 and 19 and at the rear of the detector for segments 1-8. To assess the energy resolution, a measure of the full width at half the maximum height (FWHM) was used for the Gaussian fitting to the peaks provided by GF3 for the 122 keV peak of $^{57}$Co and the 1332 keV peak of $^{60}$Co. An example energy spectrum for the point contact is shown in Figure 2.15. Each segment must pass the following SIGMA design criteria:

Individual performance:

- $<$ 2.5 keV FWHM at 122 keV
- $<$ 3.5 keV FWHM at 1332 keV

Average performance:

- $<$ 2 keV FWHM at 122 keV
- $<$ 3 keV FWHM at 1332 keV

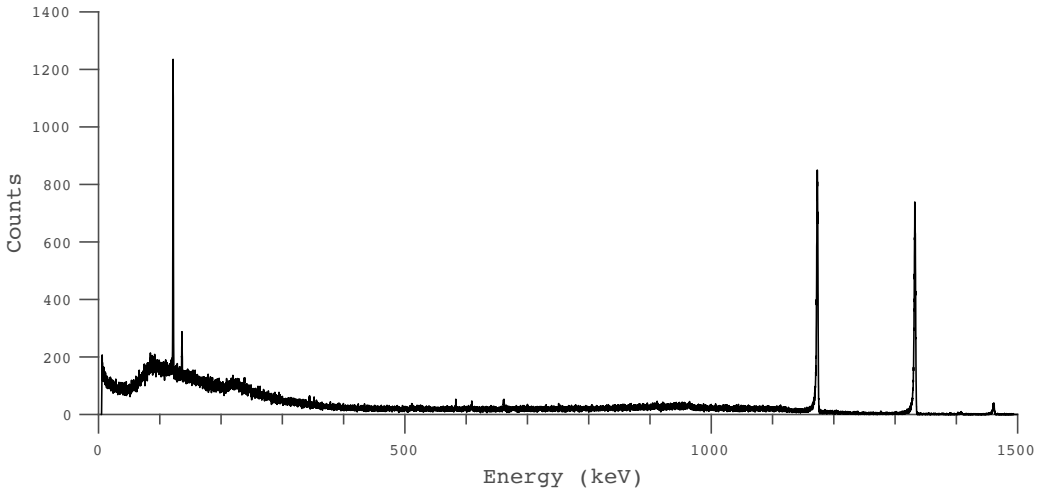


*Figure 2.15: Example energy spectrum recorded from the point contact of SIGMA for $^{57}Co$ and $^{60}Co$ sources.*

To optimise the energy resolution, the measurements were repeated over a range of shaping times from 1-12 $\mu$s. While 6 $\mu$s is a standard shaping time used for many germanium detectors, the long drift times associated with SIGMA mean longer shaping times may be required. Optimising the shaping time is a pay off between count rate and energy resolution. The count rate was kept below 1000 cps for these measurements to minimise the effects of pile up and baseline shift. As shaping time increases the FWHM is expected to improve as the ballistic deficit decreases and the series noise is reduced up to a point where the FWHM begins to increase again. This is due to the increased influence of parallel noise as shaping time increases. The point contact achieves an optimum energy resolution of 0.89 keV at 122 keV and 2.21 keV at 1332 keV by applying shaping times of 6 $\mu$s and 12 $\mu$s respectively. This is slightly higher than the 2.0 keV at 1332 keV energy resolution requirement for the third phase of DEGAS [DEG14], though as the first prototype detector of its kind, small improvements can be expected in future models which could bring this within specification. The outer segments achieve an average energy resolution of 1.42 keV at 122 keV and 2.62 keV at 1332 keV with the results for individual segments shown in Table 2.1. This is within the average performance acceptance criteria. Due to a faulty connection, while a signal was initially seen from Segment 5, the signal was lost and Segment 5 is considered a dead segment to undergo future repair.

| Segment number | 122keV | | 1332keV | |
|---|---|---|---|---|
| | FWHM (keV) | Shaping time ($\mu$s) | FWHM (keV) | Shaping time ($\mu$s) |
| PC | 0.89 | 6 | 2.21 | 12 |
| 1 | 1.48 | 6 | 3.27 | 6 |
| 2 | 0.97 | 6 | 2.36 | 6 |
| 3 | 0.82 | 6 | 2.44 | 6 |
| 4 | 1.03 | 6 | 2.70 | 6 |
| 6 | 1.67 | 6 | 2.74 | 6 |
| 7 | 1.06 | 6 | 2.40 | 6 |
| 8 | 1.38 | 6 | 2.26 | 6 |
| 9 | 2.83 | 10 | 3.40 | 10 |
| 10 | 1.67 | 12 | 2.80 | 12 |
| 11 | 1.27 | 10 | 2.05 | 10 |
| 12 | 1.32 | 10 | 2.22 | 10 |
| 13 | 1.11 | 12 | 2.04 | 12 |
| 14 | 1.21 | 10 | 2.06 | 12 |
| 15 | 1.31 | 12 | 2.13 | 12 |
| 16 | 2.48 | 12 | 2.99 | 12 |
| 17 | 1.14 | 6 | 1.82 | 6 |
| 19 | 1.42 | 12 | | |

*Table 2.1: Energy resolution values for all segments and the shaping time at which they were measured.*

Segments 1-8 all achieve their optimum resolution at 6 $\mu$s for both energies measured. Whilst there is a slight variation in the energy resolution measured for each azimuthal segment, the consistent shaping time suggests the charge collection in these segments is similar as would be expected for segments of the same shape and around the axis of symmetry. The shaping times for the longitudinal segments vary slightly but are all longer than the azimuthal segments. This suggests charge in the longitudinal segments takes longer to be collected resulting in a longer required shaping time. Segment 17 has a shorter shaping time of 6 $\mu$s suggesting that it, like the azimuthal segments, has faster charge collection than the longitudinal segments. This correlates with the size of the segments with the azimuthal segments and Segment 17 being the smallest segments. Segment 9 is the only segment to fail to meet the acceptance criteria. Segment 9 is known to be surrounded by the crystal holding structure, which may be a source of additional noise, potentially explaining its poorer performance at low energy. Segment 13 appears to perform well in terms of energy resolution, though other performance issues were seen in the energy spectra produced. Segment 13 consistently produces additional low energy peaks when exposed to a $^{60}$Co source. An example energy spectrum showing the additional peaks seen in Segment 13 is shown in Figure 2.16. This effect is not observed with the lower energy $^{57}$Co source used in these measurements. Such behaviour is indicative of crosstalk between the channels,

where a signal seen in one segment is shared with another causing an additional signal in the affected channel. The sharing of the signal between multiple channels results in degradation of the energy resolution, although corrections can be made to the output data to reduce the effects of crosstalk [BNL+17].

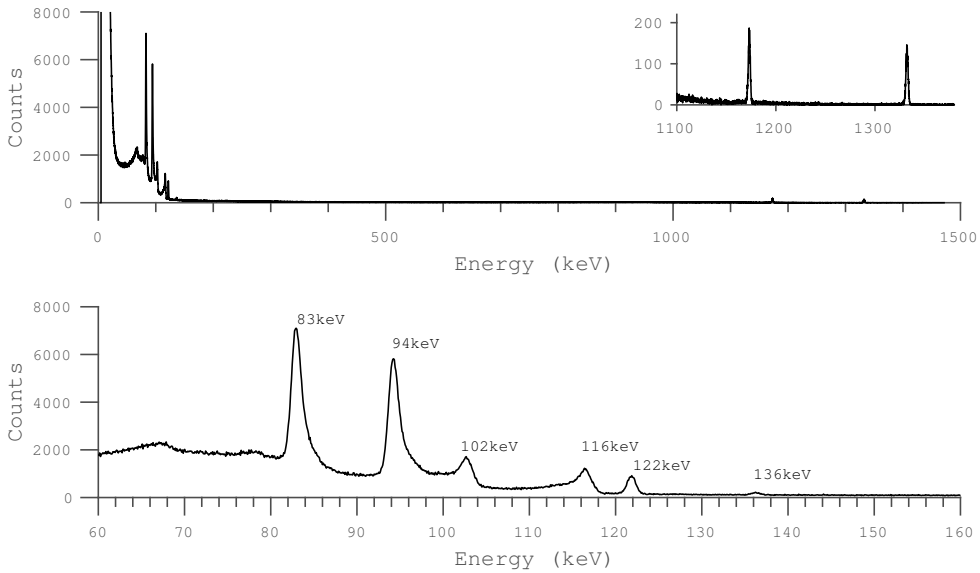


*Figure 2.16: Example energy spectra from Segment 13 for $^{57}Co$ and $^{60}Co$ sources showing additional low energy peaks. The upper image shows the full spectra with a zoomed view of the 1173 and 1332 keV peaks. The lower image includes labelled energies for the low energy peaks.*

A measurement for the 1332 keV resolution of Segment 19, the well contact, is omitted from this data. The manufacturer recommended shaping time of 24 $\mu$s was greater than was possible to replicate using the analogue system and the peaks produced at lower shaping times were difficult to give a meaningful fit. The peak produced by Segment 19 are broad, particularly at high energy, as shown in Figure 2.17. It was observed that increasing the shaping time reduced this effect at low energies but a shaping time large enough to improve the high-energy peak could not be reached. The peak shape seems to suggest two distinct pulse shapes which register at slightly different energies in the analogue system resulting in a merged double peak. As the shaping time increases the system registers the two pulse shapes as closer in energy until, at a sufficiently high shaping time, they form a single peak. This may be an issue created by the merging of segments 18 and 19 due to the change in crystal geometry or dependent on the position of the interaction in the segment.

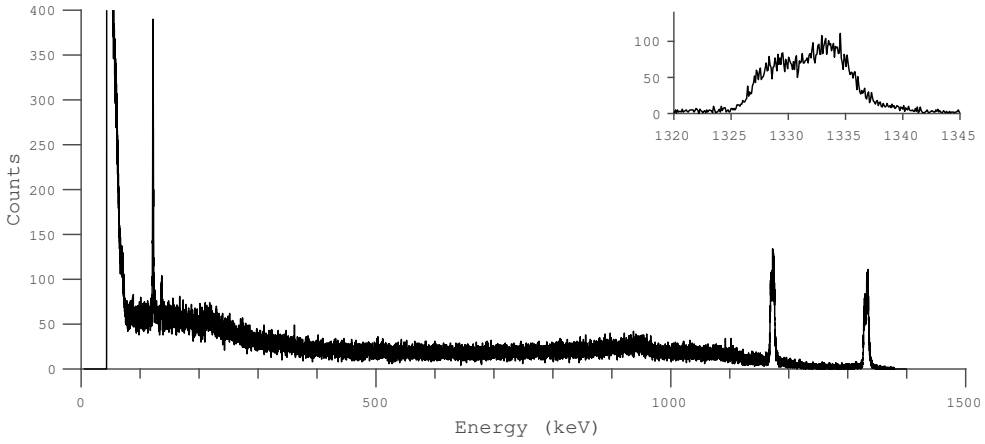


*Figure 2.17: Example energy spectra from Segment 19 for $^{57}Co$ and $^{60}Co$ sources. Zoomed section showing the shape of the 1332 keV peak.*

The energy resolution of a n-type detector with a similar geometry to SIGMA, the Inverted Coaxial Point-Contact (ICPC) detector, has been measured by [SCC+17]. Poor intrinsic energy resolution was observed in the ICPC detector due to charge trapping and recombination, which lead to the development of an algorithm to correct for these effects. The energy resolution observed for SIGMA is better than the algorithm corrected value of 3.44 at 1332 keV for the ICPC, which suggests that trapping and recombination do not have a large contribution in SIGMA.

## 2.6 Efficiency

The absolute photo peak efficiency for a detector describes the fraction of gamma rays that deposit their full energy in the detector and is given by,

$$E_{abs} = \frac{Count\ rate\ in\ photopeak}{Source\ activity\ \times\ Gamma\ fraction} \tag{2.9}$$

The absolute photo peak efficiency was investigated as a function of gamma-ray energy using a 0.179 MBq $^{241}$Am source and a 0.053 MBq $^{152}$Eu source, by inputting the point contact preamp into the same analogue system with a shaping time of 6 $\mu$s. The sources were aligned with the centre of the detector, at a distance of 25 cm from the front face of the crystal, for 1 hour each. The absolute photopeak efficiency of SIGMA measured as a function of energy is shown in Figure 2.18. Above 122 keV the efficiency is seen to decrease with energy as the gamma rays become more likely to scatter out of the detector without depositing their full energy or pass through the crystal without interacting. The probability of an interaction per unit path length is given by the mean free path, $\mu_m$, as discussed in Section 2.1. As energy increases $\mu_m$ gets smaller and, as

shown by Equation 2.2, the proportion of the gamma rays attenuated by the crystal reduces. This gives rise to the near exponential decrease in efficiency with energy. The drop in efficiency at 60 keV is due to the 1 mm aluminium cap at the front of the detector and the germanium dead layer created by the contacts attenuating the gamma rays before they can enter the active crystal volume.

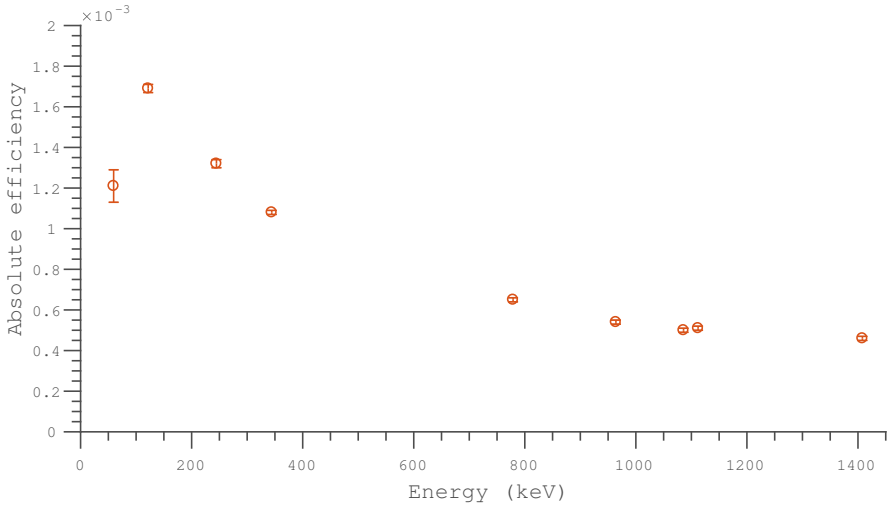


*Figure 2.18: Absolute efficiency calculated using data acquired with $^{241}Am$ and $^{152}Eu$ sources placed 25cm from the crystal.*

Relative efficiency is defined as the absolute efficiency relative to a standard 3×3 inch NaI crystal with an absolute efficiency of $1.2\times10^{-3}$ for the 1332 keV peak of $^{60}$Co [Kno10], [IEE96]. It is often used as the industry standard to compare the efficiency of different gamma-ray detectors. The relative efficiency was measured by placing a 0.2809 MBq $^{60}$Co source 25 cm from the front of the crystal face for 2500 s. The 1332 keV peak was used to calculate a relative efficiency of 40.9 ± 0.1% which is in agreement with the manufacturer specified 41% relative efficiency giving a preliminary confirmation of the detector geometry.

# 3 Singles Scanning

The University of Liverpool scanning system allows a collimated gamma-ray source to be precisely positioned in steps across the full area of the SIGMA crystal. Probing the crystal with beams of gamma rays emitted from $^{241}$Am and $^{137}$Cs sources gives information on the crystal dimensions, the active area of the segments and their location relative to other structures such as the cryostat. Front and side $^{241}$Am scans are used to reveal the true dimensions of the crystal. Multiple processing attempts in the manufacturing of SIGMA resulted in a volume reduction from the original dimensions. The $^{137}$Cs front scan is used to probe the full crystal volume, verifying features seen in the $^{241}$Am scans and allowing the visualisation of the active area of the rear segments. The $^{137}$Cs front scan is also used to position the crystal for coincidence measurements that are discussed in Chapter 4. The active area of the segments is compared to the original detector design. A comparison of two methods to calculate the number of hit segments, referred to as fold, is also made to determine the most appropriate method for future use.

## 3.1 Scanning System

The Liverpool scanning system consists of a collimated gamma-ray source mounted on a Parker scanning table. Two independent motors allow the scanning table to position the source in the x and y axes with 100 $\mu$m precision. The movement of the table can be programmed from the data acquisition system (DAQ). SIGMA was mounted above the scanning table with the 1 mm collimated source beam directed perpendicular to the front face of the detector as shown in Figure 3.1 (a). The frame supporting SIGMA allowed the detector to be lowered to minimise the distance between the collimator and the cryostat to limit divergence of the gamma-ray beam. The system allowed for either an $^{241}$Am or $^{137}$Cs source to be mounted on the scanning table, both of which have been used to investigate the geometry of SIGMA.

SIGMA was positioned on the scanning table in the *side position* and subsequently the *front position* above a collimated 1.6 GBq $^{241}$Am source. The source was encased in a 80 mm lead cube with a 40 mm long, 1 mm collimator as shown in Figure 3.1 (b). The collimation creates a 1 mm pencil beam close to the collimator opening. Divergence of the beam after it has left the collimator resulted in a 1.1 mm diameter beam spot at

the front face of the crystal. Due to the curvature of the crystal, the beam spot size on the surface of the crystal for the side measurements varies from 1.1 mm in the centre to 2.1 mm at the outer edges. In the *front position*, the crystal was also scanned with a 0.7 GBq $^{137}$Cs source encased in lead with a 80 mm long 1 mm collimator and a 100 mm long 5 mm collimator as shown in Figure 3.1 (c). This results in a beam spot size of 1.1 mm at front of the crystal and 1.5 mm at the rear.

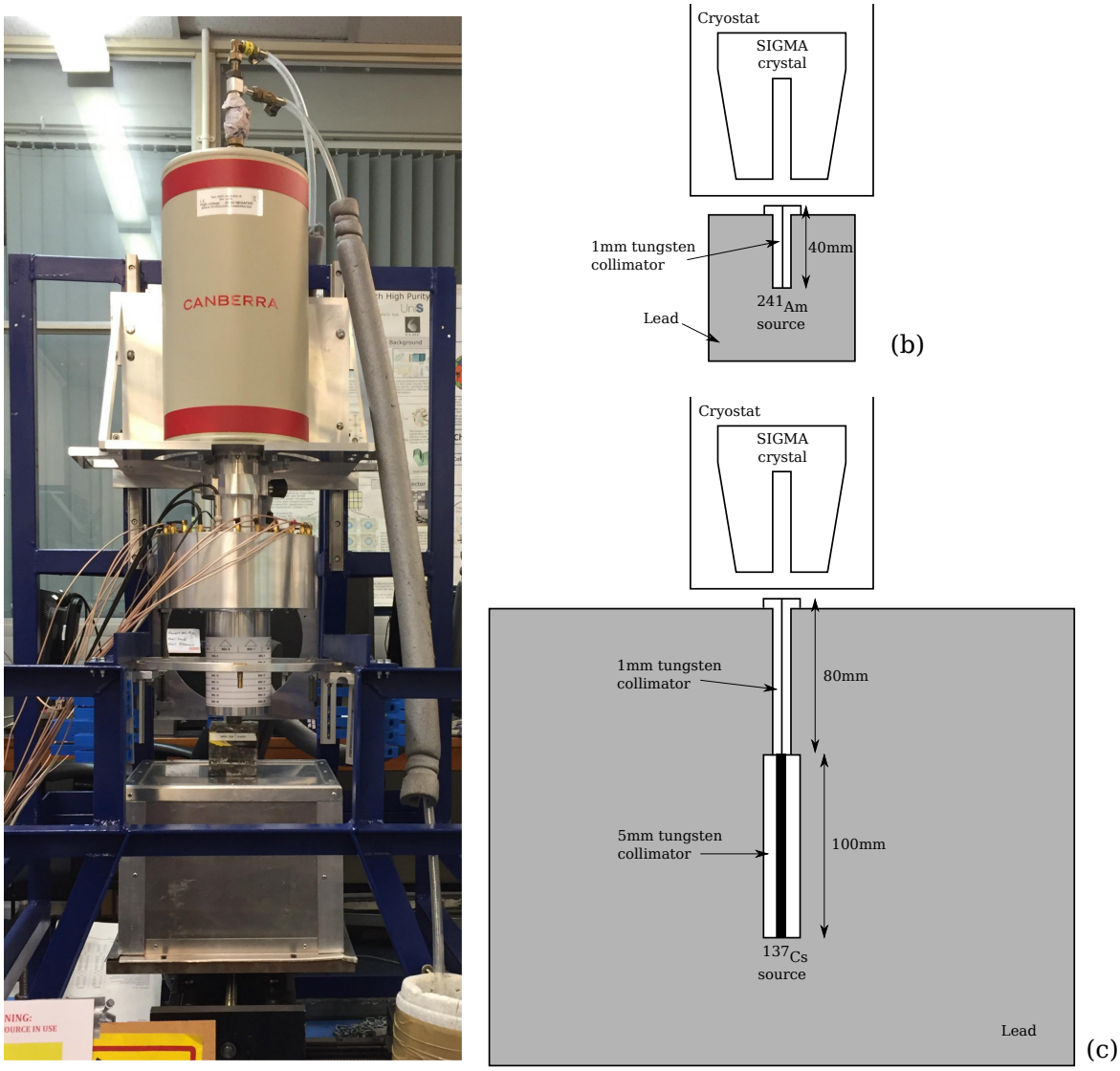


*Figure 3.1: (a) Photograph of SIGMA in the front position above the $^{241}$Am source. Illustrations showing the collimation of the $^{241}$Am source (b) and the $^{137}$Cs source (c).*

Using the DAQ system MIDAS [Nuc19], the scanning table was programmed to position the source in a 1 mm by 1 mm x-y grid across the full area of the crystal. For the $^{241}$Am side scan the table paused at each location for 20 seconds to collect

data. Once it had been established there were sufficient counts, the counting time was reduced to 10 seconds per step for the $^{241}$Am and $^{137}$Cs front scans to reduce the scanning time.

## 3.2 Data Acquisition System

Data were acquired using the digital electronics system shown in Figure 3.2, which allows both online processing and the recording of data to disk for offline processing. The preamplifier signals for all 19 channels first pass through a Gain and Offset (GO) box designed to amplify the signal so that the full dynamic range of the digitisers is used. A gain factor of 2 was used for the point contact and a gain factor of 5 used for all of the other channels. The GO box also allows the baseline offset to be adjusted individually for each channel. The signals are then passed to CAEN V1724 digitisers which have a sampling rate of 100 MHz, equating to 1 sample every 10 ns. Each digitiser has 8 channels meaning 3 were required to fully instrument SIGMA's 19 channels. To align the timing of the 3 digitisers, a V1495 general purpose VME board was used to synchronise the time stamps. The system was operated in singles mode so that if the point contact is triggered all channels are written out to the DAQ via the V2718 VME to PCI optical link bridge where it is stored to disk for future processing using mtsort [Jud19]. During the set up of the digital electronics system, segments 15 and 16 displayed high levels of noise which the digitisers struggled to cope with and had to be disconnected from the system. This meant data for these segments could not be collected and they are missing from the singles and coincidence scanning measurements.

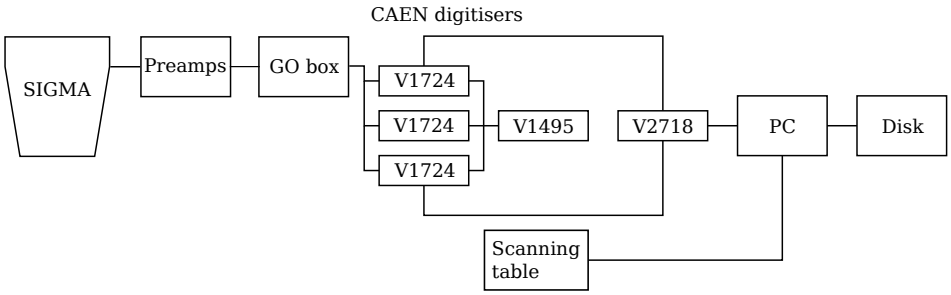


*Figure 3.2: Schematic of the electronic components used for singles scanning data acquisition.*

To convert the preamplifier pulse to a digital signal, the pulse was sampled over a 28 $\mu$s window. A decimation of 4 was employed resulting in a sampling rate of 1 sample every 40 ns. The energy of each pulse was calculated in two ways using either the baseline difference or a Moving Window Deconvolution (MWD) algorithm [GGL94]. The baseline difference is calculated by sampling an area of the baseline at the start of the pulse and the peak of the pulse and determining the difference between the two. Due to the shape of the preamplifier pulse, the peak area of the pulse sampled will

not be flat but contain part of the exponential decay of the pulse, or if placed poorly, the rising edge. To gain a better estimate of the pulse height, MWD uses a trapzoidal filter to create a flat top area for sampling. The digital signal produced by sampling the preamplifier pulse has a long exponential decay which is removed by the MWD by first turning it into a step function, maintaining the pulse height. The signal is then differentiated to create a square pulse. A moving average window is applied to the square pulse to smooth the pulse and remove noise resulting in the final trapezoidal pulse shape. The energies used in this section are calculated using MWD.

## 3.3 $^{241}$Am Singles Scanning

When the collimated beam is scanned across the surface of the crystal, an intensity matrix is created displaying the number of counts recorded at each x-y location. The counts at this stage include any signals recorded by the detector including background and scattered photons, meaning counts can appear when the beam was positioned outside of the crystal volume. To limit the effects of this and gain a clearer image of the crystal geometry, selection criteria can be set to limit the data included. By applying an energy gate around the full energy peak of the source only gamma rays which deposit their full energy in the crystal volume are included. $^{241}$Am produces a 60 keV gamma ray and was chosen for surface scanning due to the low penetration, only probing the first few mm of the crystal with Equation 2.2 showing 88 % of gamma rays are stopped in the first 2 mm. This allows the surface structure of the crystal to be investigated. An energy gate of 60 $\pm$ 2 keV was used to produce side and front face surface scans of the crystal in the orientations shown in Figure 3.3. The position of the energy gate is shown relative to the peak produced by the point contact in Figure 3.4.

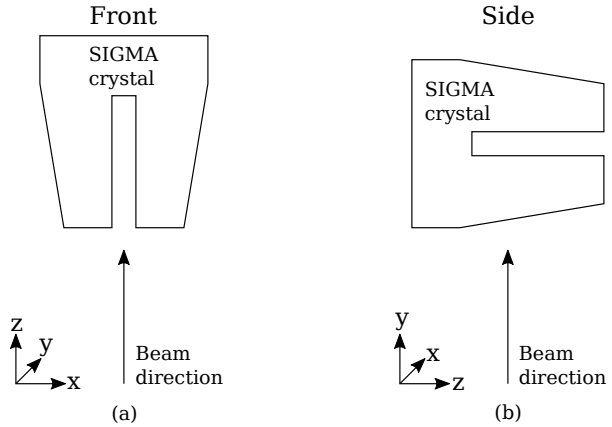


*Figure 3.3: Orientation of the crystal relative to the beam direction for the front (a) and side (b) scanning positions.*

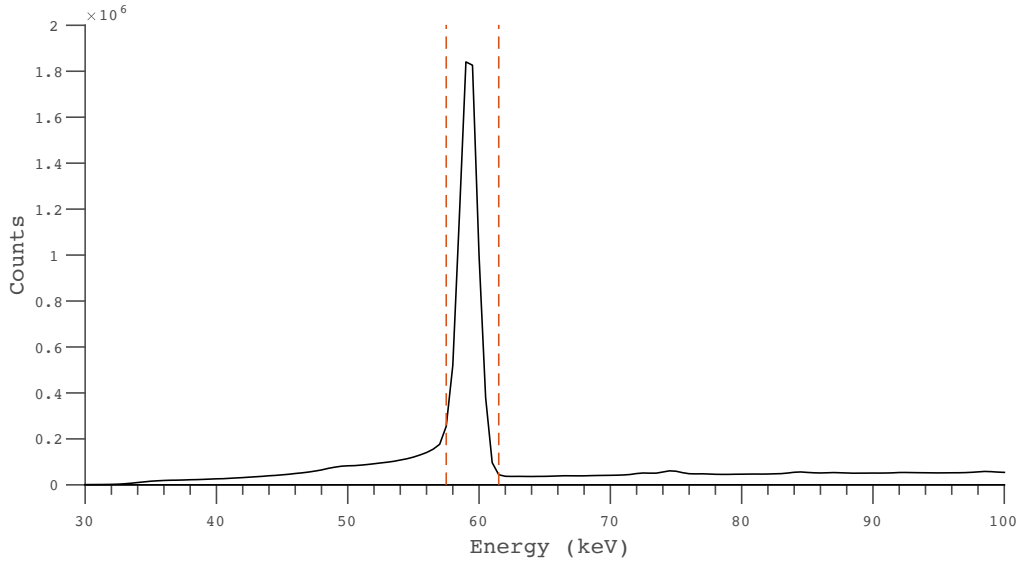


*Figure 3.4: Energy spectrum from the point contact of SIGMA recorded during the $^{241}$Am scan. The position of the ± 2 keV energy gate is represented by the red dashed lines.*

### 3.3.1 Side Scan

The energy gated intensity matrix produced by scanning the side of the crystal is show in Figure 3.5 (a). The majority of background counts have been removed by setting a threshold of 175 counts. Any positions with fewer counts than the threshold are displayed as white. The segmentation scheme of the crystal is clearly seen when compared to Figure 3.5 (b) with increased counts of around $\sim$ 3800 at the segment boundaries compared to $\sim$ 3300 in the centre of the segment volume. This suggests the electrodes are thinner at the segment boundaries. There are two areas of reduced intensity where the counts drop to $\sim$ 1200, seen in segments 14 and 15 at xy= (42,73) mm and (71,83) mm respectively, which relate to the placement of the electrodes on the crystal. Segment 9, at the rear of the crystal, is much fainter than the other segments with around $\sim$ 1000 counts. This is due to the attenuation of the low energy $^{241}$Am source by the holding structure which surrounds Segment 9. The intensity decreases towards the edges of the crystal due to the cylindrical shape of the crystal and the cryostat meaning gamma rays at the edges pass through more aluminium and a thicker contact dead layer.

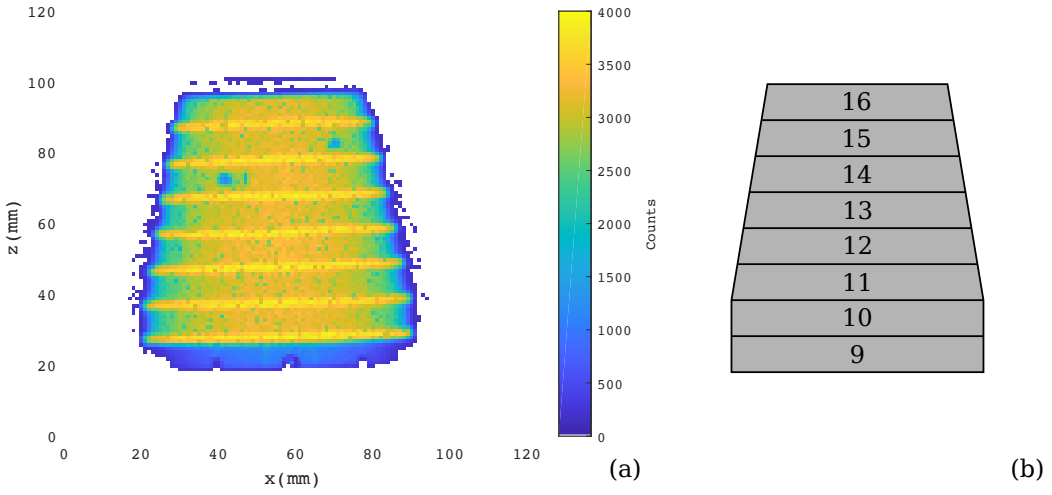


*Figure 3.5: (a) Energy gated intensity matrix showing the number of counts per x-z position recorded by the point contact. (b) Illustration of the longitudinal segmentation of SIGMA with segment numbers.*

To visualise the number of counts in the different regions of the crystal, a slice through x = 56 along z is shown in Figure 3.6. The segment boundaries are clearly visible as regularly spaced peaks. By comparing the counts measured in the segment volume and at the segment boundaries, the difference in contact thickness can be estimated using Equation 2.2. The attenuation coefficient for a 60 keV gamma ray in germanium is 2.03 cm$^2$/g [Cha67]. The average difference in thickness between the segments and boundaries is therefore calculated to be $\sim$ 180 $\mu$m of germanium.

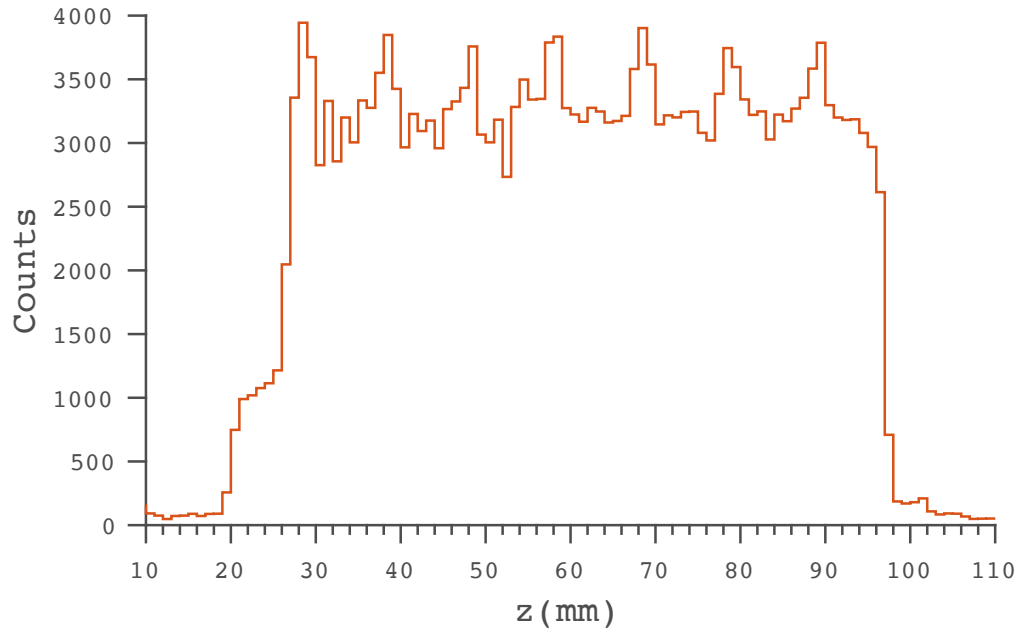


*Figure 3.6: The number of counts per z depth for a slice through the centre of the crystal.*

Whereas Figure 3.5 was created by applying an energy gate to the point contact, equivalent intensity matrices can be produced for each segment by gating on the energy measured by individual segments. This depicts the x,z region represented by the collecting electrode, which is illustrative of the weighting potentials discussed in Section 2.3.1. The number of counts in the segment gated matrices will vary from those seen in the same area of the point contact gated matrices as the point contact is the full volume contact. This means the point contact matrices include any number of interactions in the entire crystal where the energy gate is met, whereas the segments include any number of interactions within that segment which meet the energy gate.

Figure 3.7 shows the energy gated matrices for segments 9-14. A threshold has been used again to remove background events, set to 100 counts for all but Segment 9 which is set at 55 due to the lower count rate seen in Segment 9. The low penetration distance of the $^{241}$Am gamma rays means only segments directly facing the source can be visualised. Looking at the signals from individual segments allows the active area of those segments to be measured. Segments 10-14 are all 10.0 $\pm$ 0.7 mm in the z axis as specified in the initial design supplied to the manufacturer. Due to the loss of counts around Segment 9 it is hard to measure the true size of the segment. Assuming it is the same as the other longitudinal segments measured gives the crystal a full height of 79.0 $\pm$ 0.9 mm, close to the 80 mm specified.

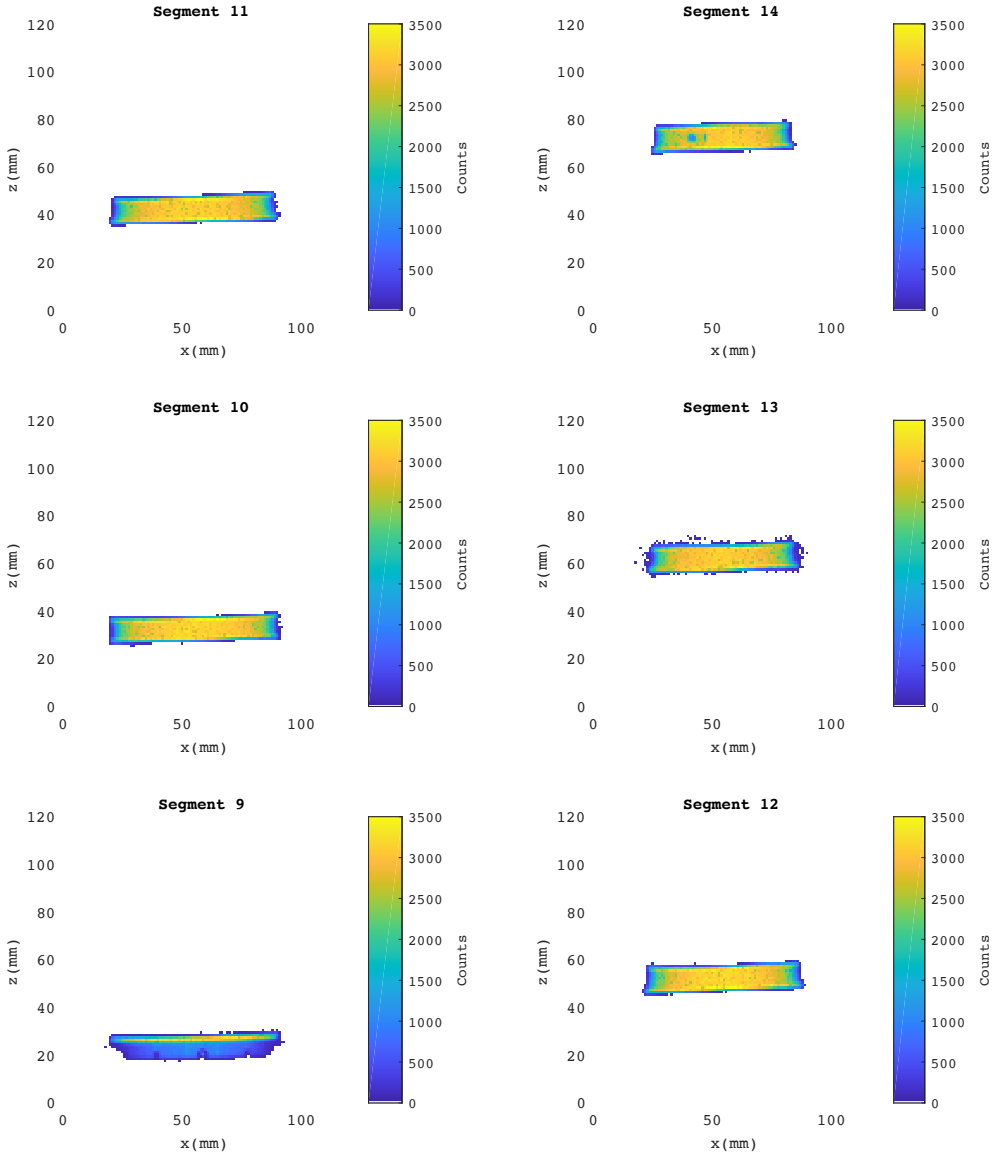


*Figure 3.7: Energy gated intensity matrices showing the number of counts per x-z position seen by segments 9-14.*

The size and position of the active areas of the outer segments seen in Figure 3.7 are compared to the contact areas for the original detector design. Due to the low penetration distance of the 60 keV gamma ray of $^{241}$Am only the first few mm of the crystal are investigated. For segments 11-14 the segment boundaries show good correlation with the original design. The boundary between segments 9 and 10 is the only boundary which shows significant deviation from the original specification, with Segment 10 extending further down and reducing the width of Segment 9.

### 3.3.2 Front Scan

The same scanning technique and energy gates were also used to produce an $^{241}$Am surface scan of the front face of the crystal. Figure 3.8 shows the energy gated intensity matrix for the point contact with a background threshold of 50 counts. The crystal appears as an area of higher intensity surrounded by 2 low intensity rings. The outer 100 mm diameter ring (ring 1) is produced by the cryostat and the inner 85 mm diameter ring (ring 2) by the holding structure of the crystal causing gamma rays to scatter into the crystal. These could be removed by using a smaller energy window for the gating but offer valuable information on the location of the crystal within the cryostat and potential causes of attenuation, such as the holding structure, which should be considered in future measurements.

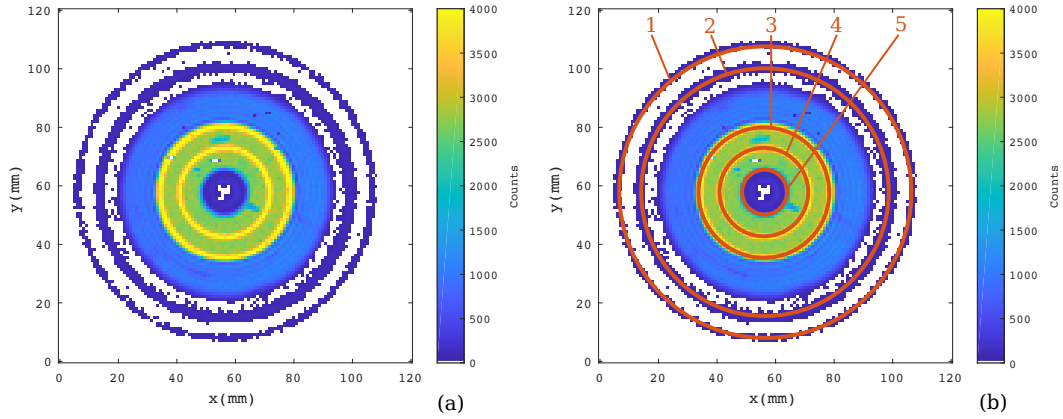


*Figure 3.8: Energy gated intensity matrix showing the number of counts per x-y position recorded by the point contact (a) with ring structures labelled (b).*

The boundaries between the front segments are seen as higher intensity rings of 30 and 47 mm diameter (rings 3 and 4) with $\sim$ 4000 counts compared to $\sim$ 3000 counts in the centre of the contact area. This increase is due to the reduced contact thickness at the segment boundaries. At the outer edge of the well, a ring of lower intensity (ring 5) connected to a protrusion extending into Segment 19 is observed which has $\sim$ 1500 counts and resembles the similar area of lower intensity seen in Segment 17. These areas are caused by attenuation of the gamma-ray beam by the outer contacts and electrodes. The counts per position change rapidly within the well, this can also be visualised in Figure 3.9 which shows the counts per position for a slice through the centre of the crystal at y = 57 mm. The intensity initially drops to $\sim$ 100 counts due to the well contact which runs the full depth of the well producing the equivalent to a 55 mm deep dead layer for gamma rays at the well edges, visualised in Figure 3.10, which absorb the $^{241}$Am 60 keV gamma rays. The counts then increase slightly to $\sim$ 200 to form a 10 mm ring relating to the central well. Moving further into the well, the counts drop again to $\sim$ 50 for the 6.0 mm diameter central region in line with the

point contact. A few reduced intensity sections seen in the crystal area are caused be the scanning table temporarily losing connection to the DAQ and losing data. As these areas are easily identifiable by their shape, 1 pixel wide in the y axis and neighbouring x axis pixels, due to the pattern of scanning, it is assumed they do not relate to any real features in the crystal.

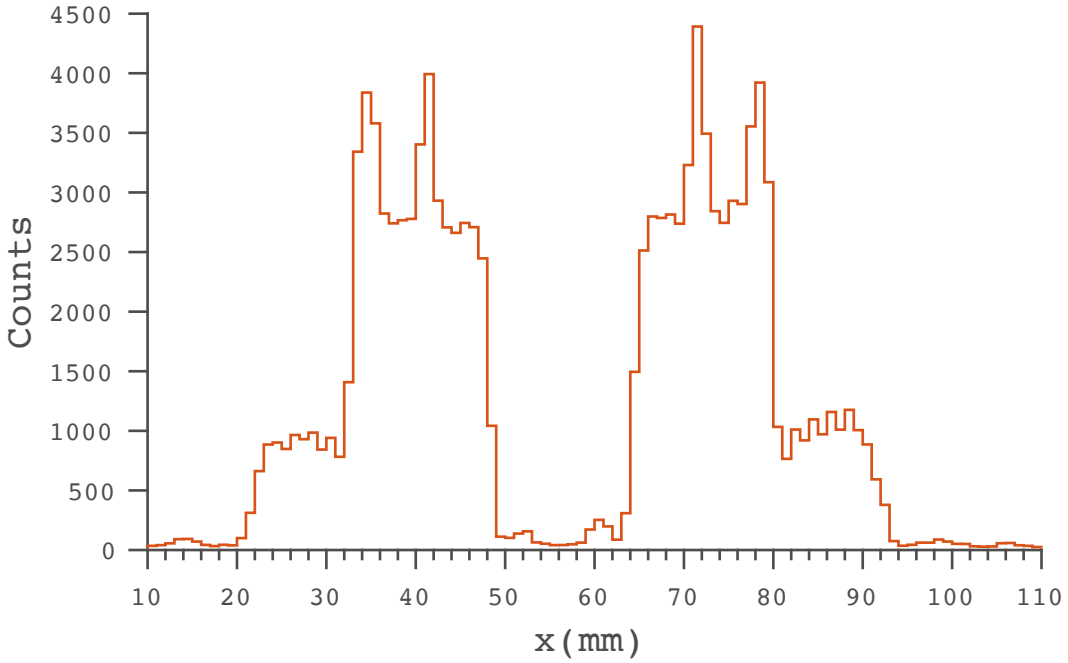


*Figure 3.9: The number of counts per x position for a slice through the centre of the crystal.*

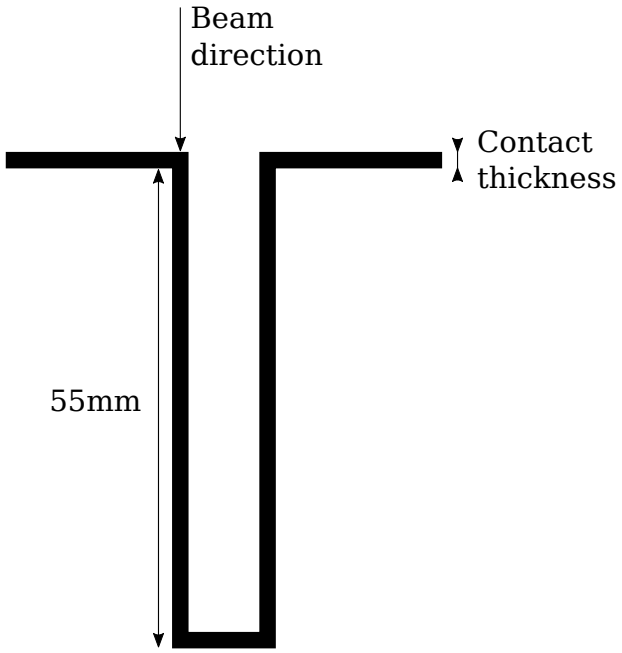


*Figure 3.10: Sketch showing the thickness of the well contact relative to beam direction.*

Intensity matrices were also produced for each segment individually as seen in Figure 3.11 (a) with a background threshold of 60 counts for segments 13 and 17 and 40 counts for all other segments. These images are equivalent to those shown for the side scan in Figure 3.7 and display the number of counts per position which pass the energy gate recorded in a single segment. Due to the low penetration of $^{241}$Am, a response is seen in the front face segments, 17 and 19, and the tapered segments, 11-14. A response is also seen in Segment 10 as some gamma rays are able to penetrate the thin, outer tapered edge of Segment 11. No response is seen in the rear segments 1-9 as they cannot be directly entered by the beam without passing through more than a few mm of the crystal as shown in Figure 3.11 (b) and (c). For segments 11-14, the width of the ring is measured to be 2.0 $\pm$ 0.7 mm, this corresponds to the projection of the tapered area visible from the front face of 1.8 mm based on the original $10^o$ tapered design. The number of counts in segments 11-14 is also seen to increase the closer the segment is to the front of the crystal due to the reduced source distance and beam divergence.

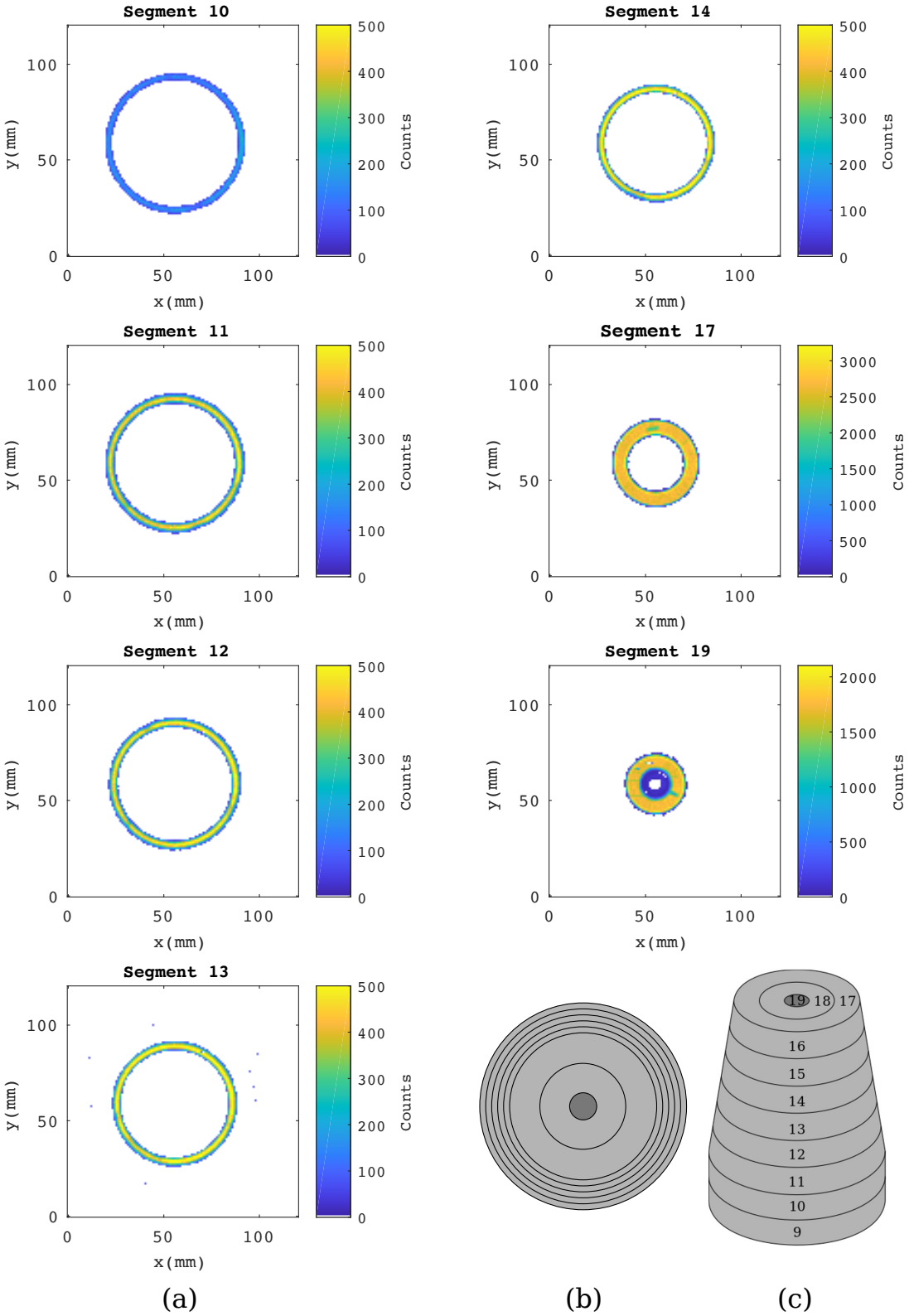


*Figure 3.11: (a) Energy gated intensity matrices showing the number of counts per x-y position recorded by segments 10-19. Illustrations of the SIGMA crystal as seen from the scanning position (b) and from the side with numbered segments (c).*

Combined with the side scan, these measurements give the outer dimensions of the crystal. Most of the measurements appear to be within error of the initial design such as the width of the rear of the crystal which is measured at 70.0 ± 0.7 mm. The only dimension identified as notably different is the diameter of the front face which is 47.0 ± 0.7 mm rather than the 49 mm stated in the design. This suggests that much of the loss in mass due to reprocessing can be attributed to the front face rather than a uniform loss from all sides and further explains the need for the merged segments in this area.

### 3.3.3 Risetimes

Due to the low penetration of $^{241}$Am it can be assumed that all interactions happen in the first few mm of the crystal, as such all the pulses produced for a single x-y location will have similar properties including the risetime of the pulses. Risetime is a standard method used to examine charge collection in HPGe detectors. Risetime refers to a time taken for a pulse to rise from one fraction of the full amplitude to another. Given the difficulty in measuring the exact moment of charge creation and the full amplitude of a pulse due to noise in the signal, the fractions of the full amplitude used can differ. The appropriate fraction is determined by the magnitude of the signal to noise and the area of interest within the rising edge. To gain the fullest possible picture of charge collection in the SIGMA crystal from this data the widest possible risetime gating will be used. $^{241}$Am has a relatively low energy of 60 keV resulting in poor signal to noise as displayed in Figure 3.12 (a). Measuring the risetime of individual $^{241}$Am pulses and forming an average for the x-y location in this way would limit the risetime to t10 - t90, defined as the time at which the pulse reached 10% and 90% of the final amplitude. To reduce the noise and widen the risetime limits, an average pulse for each x-y location was created as shown in Figure 3.12 (b). The pulses where aligned by the point at which they reach 50% of their maximum height, referred to as t50, and summed to form an average pulse response for the location. A single risetime measurement was made of the average pulse at each x-y location from t01 - t99, defined as the time at which the pulse reaches 1% and 99% of the full amplitude.

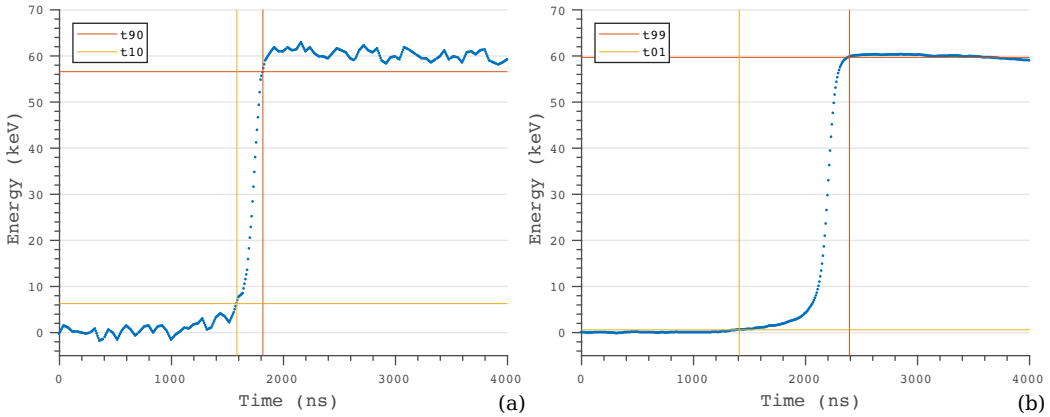


*Figure 3.12: A single $^{241}$Am pulse recorded in the point contact (a). The noise level in the pulse means risetime limits are limited at t10 and t90 as shown by the yellow and red lines respectively. An average of all the $^{241}$Am pulses at a single x-y location (b) Due to the reduced noise the risetime limits can be increased to t01 and t99 shown by the yellow and red lines respectively.*

Figure 3.13 (a) shows the risetime t01 - t99 for each x-y position with greater than 50 counts in the crystal volume across the front face of the crystal. Some of the crystal features identified in the energy gated intensity matrix (Figure 3.8) are also visible here, including the well and the front face of the crystal boundary as highlighted in Figure 3.13 (b). The risetimes recorded inside of the well are much shorter than those in other areas of the crystal at $\sim$ 600 ns. This is due to the interactions occuring deeper in the crystal and closer to the point contact, resulting in a much shorter drift time. A slight increase in risetime is seen around the outer edge of the well and the outer edge of the front face of the crystal though the risetime shows little change across the crystal varying between $\sim$ 900 ns to $\sim$ 1200 ns. This suggests that though the full drift time from charge creation to charge collection changes with location in the crystal, the risetime from t01 - t99 remains relatively constant.

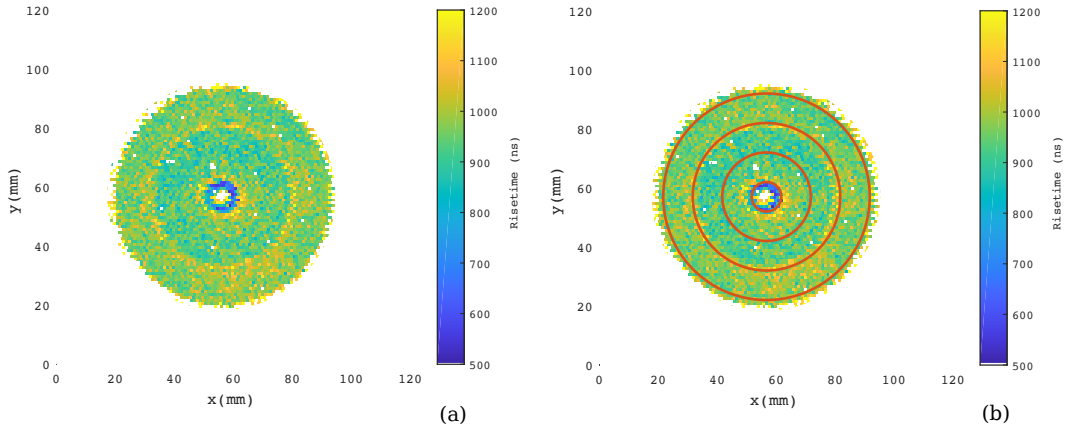


*Figure 3.13: Matrix showing the average risetime per x-y position for the front face of the crystal (a) with lines superimposed representing crystal boundaries (b).*

## 3.4 $^{137}$Cs Singles Scanning

The scanning table also allows the use of a $^{137}$Cs source to scan the front face of the detector. The greater penetration of gamma rays with energy 662 keV emitted from $^{137}$Cs compared to 60 keV from $^{241}$Am means additional information could be gathered on the crystal characteristics as well as creating a coordinate system for the crystal relative to the $^{137}$Cs source for future coincidence measurements. Whereas with the $^{241}$Am scan it could be assumed that all interactions occurred in the first few mm of the crystal, there is no depth constraint for the $^{137}$Cs with Equation 2.2 showing $\sim$ 12 cm of germanium is required to stop 99 % of gamma rays, greater than the height of the crystal. At 662 keV the dominant interaction mechanism in germanium is Compton scattering. For these interactions the x-y location of the scanning beam is therefore for the first interaction only and subsequent interactions can occur at any position within the crystal. An energy gate of 662 $\pm$ 5 keV, as shown in Figure 3.14, was used to produce a front face scan of the crystal. Figure 3.15 shows the energy gated intensity matrix for the point contact with a background threshold of 10 counts.

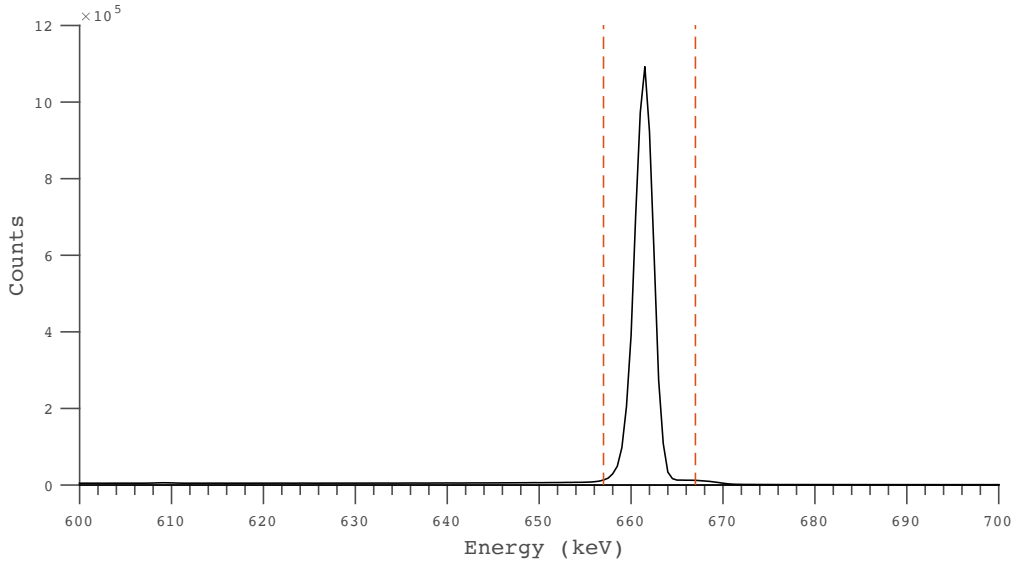


*Figure 3.14: Energy spectrum from the point contact of SIGMA recorded during the $^{137}$Cs scan. The position of the $\pm$ 5 keV energy gate is represented by the red dashed lines.*

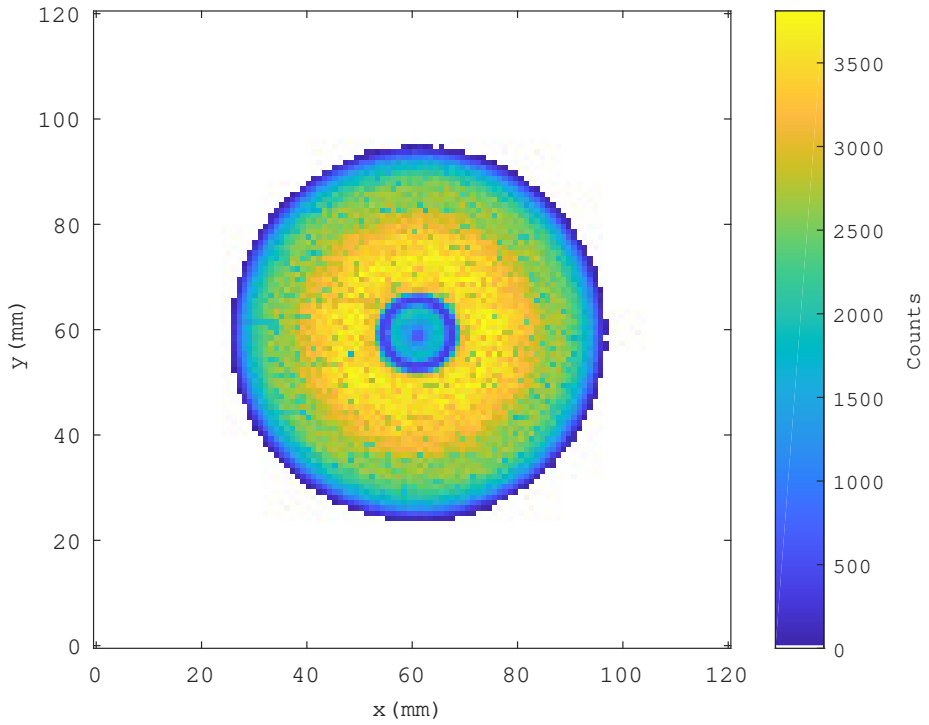


*Figure 3.15: Energy gated intensity matrix showing the number of counts per x-y position as recorded by the point contact.*

For the gamma rays emitted from the $^{137}$Cs source, interactions are happening at a range of depths within the crystal, hence, the boundary between the front and tapered edge is not seen as sharply as with the $^{241}$Am shown in Figure 3.8, though a rough outline of the front face is visible as an area of $\sim$ 3500 counts. The inner edge of the front ring and the start of the well can again be seen as an area of reduced intensity down to $\sim$ 400 counts due to the well contact. The counts in the well increase to $\sim$ 2000 at the outer edges, reducing to $\sim$ 600 counts over the point contact. This overall reduction compared to the counts seen in the front face of the crystal is partly due to the reduced thickness of germanium at the base of the well attenuating less of the beam. The same effect is seen in the gradual decrease in counts towards the outer edges of the crystal as the taper results in less germanium for the beam to pass through and a greater likelihood of the gamma ray scattering out of the crystal.

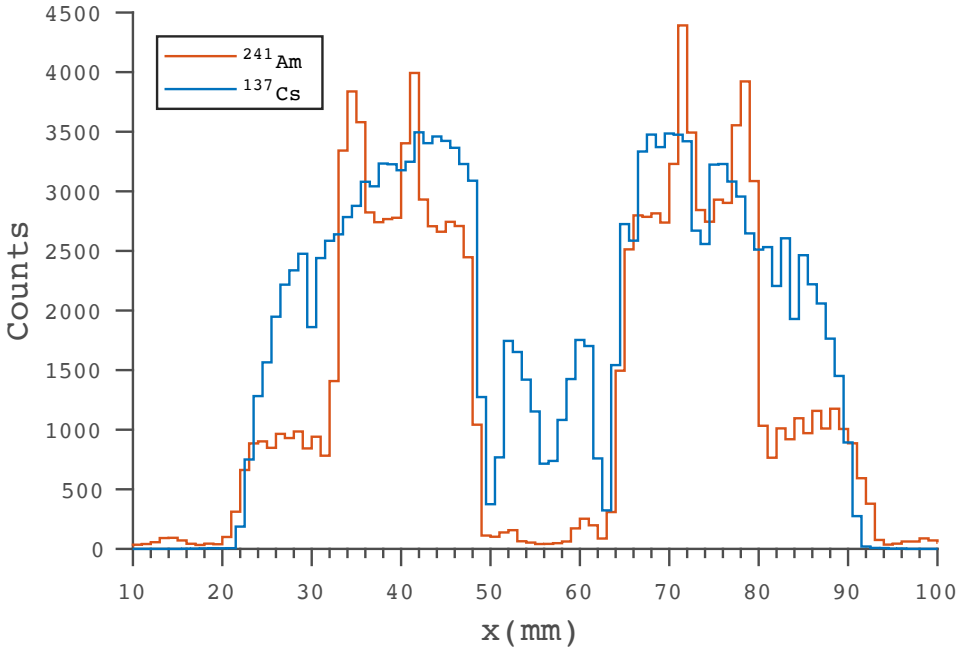


*Figure 3.16: Energy gated counts recorded in each x position across the centre of the crystal for a set y value for the $^{241}$Am and $^{137}$Cs font face scans.*

Direct comparison of the counts recorded per position for the $^{241}$Am and $^{137}$Cs front face scans can offer additional information on the crystal structure. This is done by taking a slice through the intensity matrix for a set y value. Figure 3.16 shows the counts recorded at each x location for a slice through the centre of the detector. The 4 peaks seen in the $^{241}$Am spectrum at x = 34 mm, 41 mm, 71 mm and 78 mm correspond to the increased counts at the segment boundaries observed in Figure 3.8. These are not in the $^{137}$Cs due to the higher penetration of the 662 keV gamma ray being relatively unaffected by the change in contact thickness. Using Equation 2.2 the average difference between the segments and segment boundaries seen in the $^{241}$Am spectrum relates to $\sim$ 350 $\mu$m of germanium. The taper of the crystal also has less of an effect on the counts recorded for the $^{137}$Cs, which is seen to gradually decrease with distance rather than the steep cut off seen in the $^{241}$Am at x = 32 and 80. Both spectra show a sharp decrease in counts at the outer edge of the well at x = 49 and 63 due to the length of the well contact, though the $^{137}$Cs is still above background suggesting a small number of photons manage to penetrate this layer and reach the active detector volume beneath. The dip in the centre of the well for both sources relates to the location of the point contact and possibly the location of the electrode for reading out the well segment. Slices were also taken for a set x value through the central point of the detector for both the $^{241}$Am and $^{137}$Cs scans as shown in Figure 3.17. This gives a preliminary confirmation of the symmetry of the detector with the slices matching closely. The only significant difference in the counts recorded is in the $^{241}$Am slices at

75 mm where the constant x value is lower than the constant y. This is due to the contact placement seen in Figure 3.8. The contact for Segment 17 is in line with the central constant x slice used causing the drop in counts.

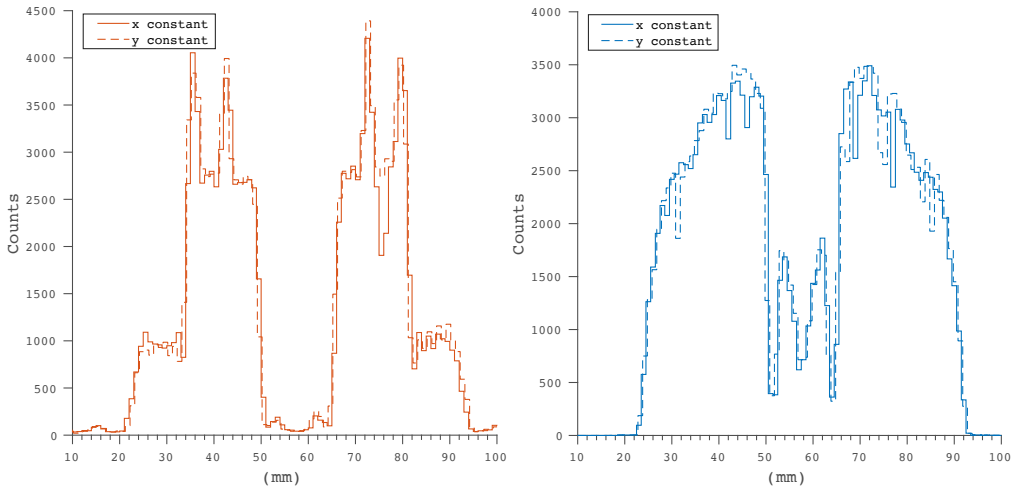


*Figure 3.17: Energy gated counts recorded for slices through the centre of the detector in the x and y axis for an $^{241}$Am source (on the left) and a $^{137}$Cs source (on the right).*

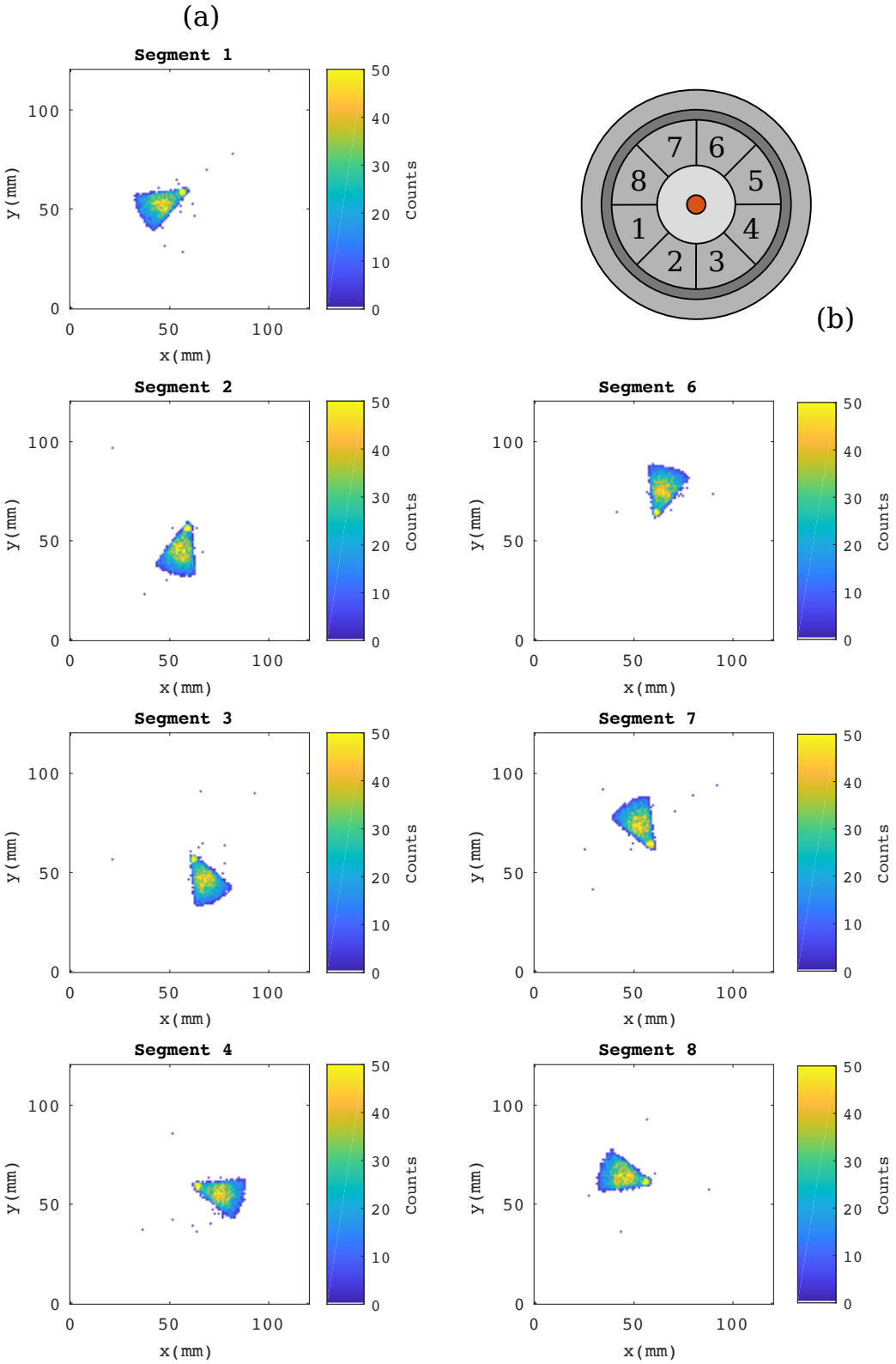


*Figure 3.18: (a) Energy gated intensity matrices showing the number of counts per x-y position seen by segments 1-8. (b) Illustration of the rear segmentation scheme of the SIGMA crystal*

As with the results shown in Figure 3.11 for the $^{241}$Am front scan, intensity matrices can be produced for the individual segments of the crystal. Due to the higher penetration of the $^{137}$Cs gamma rays all active segments can now be observed, including the azimuthal segments at the rear of the crystal, which are shown in Figure 3.18 (a) with a background threshold of 2 counts. While a background threshold has been applied there are still a small number of points outside of the segments. These are background counts due to gamma rays scattering into the segment which, due to the low count rate at the back of the crystal, cannot be removed without also removing counts in the segment area. These images allow the dimensions of the segments to be confirmed as those given in the initial specification for the crystal design. For each segment, the areas of highest intensity is located in the central area of the segment and at the tip, close to the point contact as visualised in Figure 3.18 (b). The increase in the central region of each segment to $\sim$ 40 counts compared to $\sim$ 15 at the edges, is due to the energy gating excluding events which scatter into neighbouring segments, which is more likely to occur close to segment boundaries. The increase seen at the tip to $\sim$ 80 counts correlates with the position of the central well of the detector and can be observed in Figure 3.19 where the diameter of the ring of increased counts relates to the well diameter. The beam is much higher intensity in the region underneath the well as the gamma rays do not pass through the main bulk of the crystal resulting in the increased counts. Figure 3.19 also clearly shows the dip in counts at the segment boundaries and the reduction in counts above the point contact where the well contact is predicted to collect the secondary charge carriers.

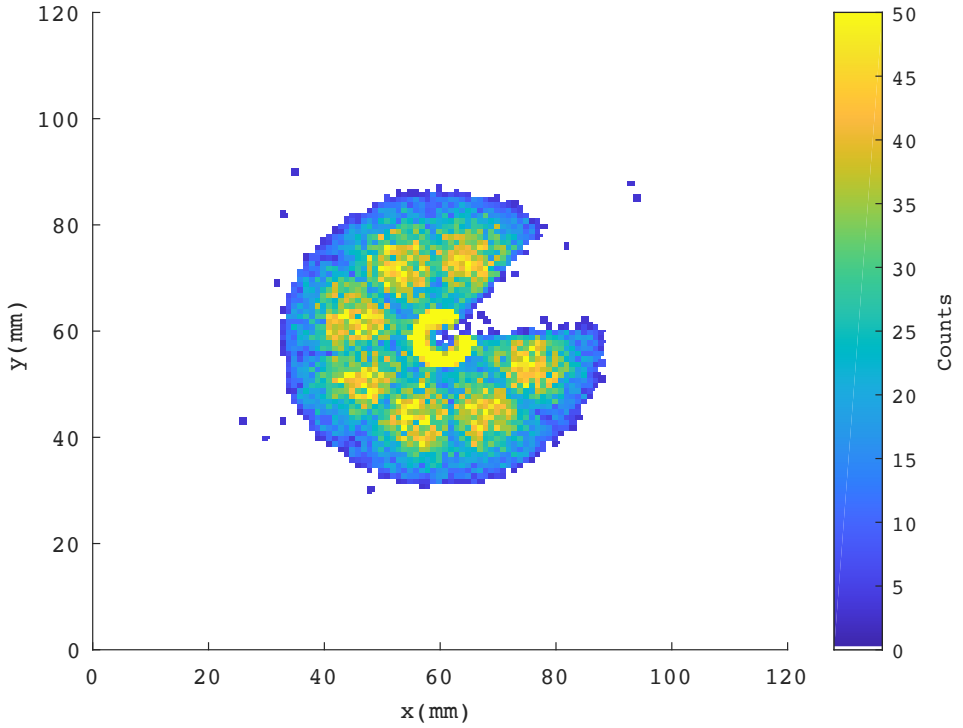


*Figure 3.19: Combined energy gated intensity matrix showing the number of counts per x-y position seen by segments 1-8.*

Intensity matrices were also produced for segments 9-19, shown in Figure 3.20 with a background threshold of 8 counts for Segment 19 and 3 counts for all other segments. For segments 10-14 the most counts are seen at the outer edge with the counts reducing toward the centre of the crystal. This corresponds to the thickness of germanium the photons will have passed through to reach each area of the segment with the least being at the outer edge. For Segment 17 the opposite is true with the most counts being at the edge of the inner radius. This is due to the shape of the surrounding segments meaning the active area for Segment 17 is thickest at the inner edge and thinnest at the outer edge.

The inner diameter of Segment 9 shows a square shaped variation in the counts. This may be an indication of the position of the crystallographic axes in the detector. Germanium has a face-centred cubic (FCC) diamond lattice structure. The properties of the crystal, including the mobility of charge carriers, are dependent on the orientation of the lattice [DBB$^+$10]. As the drift velocity depends on the mobility of charge carriers, drift velocity is also effected by the lattice orientation. At a given radius drift time will vary with the lattice orientation with the shortest drift time along $\langle 100 \rangle$ where drift velocity is highest and the longest drift time along $\langle 110 \rangle$ where drift velocity is slowest [MGL$^+$00]. The crystallographic axes are visible in the energy gated intensity matrix of Segment 9 due to the low count rate at the inner edge. The probability of trapping and recombination increases the slower the drift velocity, meaning events in the longer drift

time areas of the crystal are more likely to suffer from charge loss [Kno10]. This charge loss affects the number of events which meet the energy gate, reducing the accepted counts in longer drift time areas. The original design for SIGMA asked for $\langle 110 \rangle$ to be along the segment 1/8, 2/3, 4/5 and 6/7 boundaries and $\langle 100 \rangle$ to be along the segment 1/2, 3/4, 5/6 and 7/8 boundaries. This agrees with the orientation seen in Segment 9 with the low count area extending furthest along the $\langle 110 \rangle$ axes as expected.

Segments 11-17 show a well defined inner edge displaying the boundary between secondary collecting electrodes. By measuring the inner and outer diameter of segments 11-14 the active area of these contacts and the well contact can be estimated. In [WHBB$^+$18] the charge collection area of each segment was simulated, shown in Figure 3.21. Lines have been added to Figure 3.21 to show the measured internal and external diameter of some of the longitudinal segments. The depths of the lines is based on the segment positions from the $^{241}$Am side scan as there is no depth information extracted directly from this scan. The front scan data gives a single diameter value for each segment and cannot be used to identify the finer structure, however the measured values follow the same general trends as the simulation with the well contact being widest in line with segments 12 and 13. The inner diameter becomes less well defined for segments 9 and 10 as the active area for these segments reduces towards the centre of the crystal due to the charge collection area of the azimuthal segments.

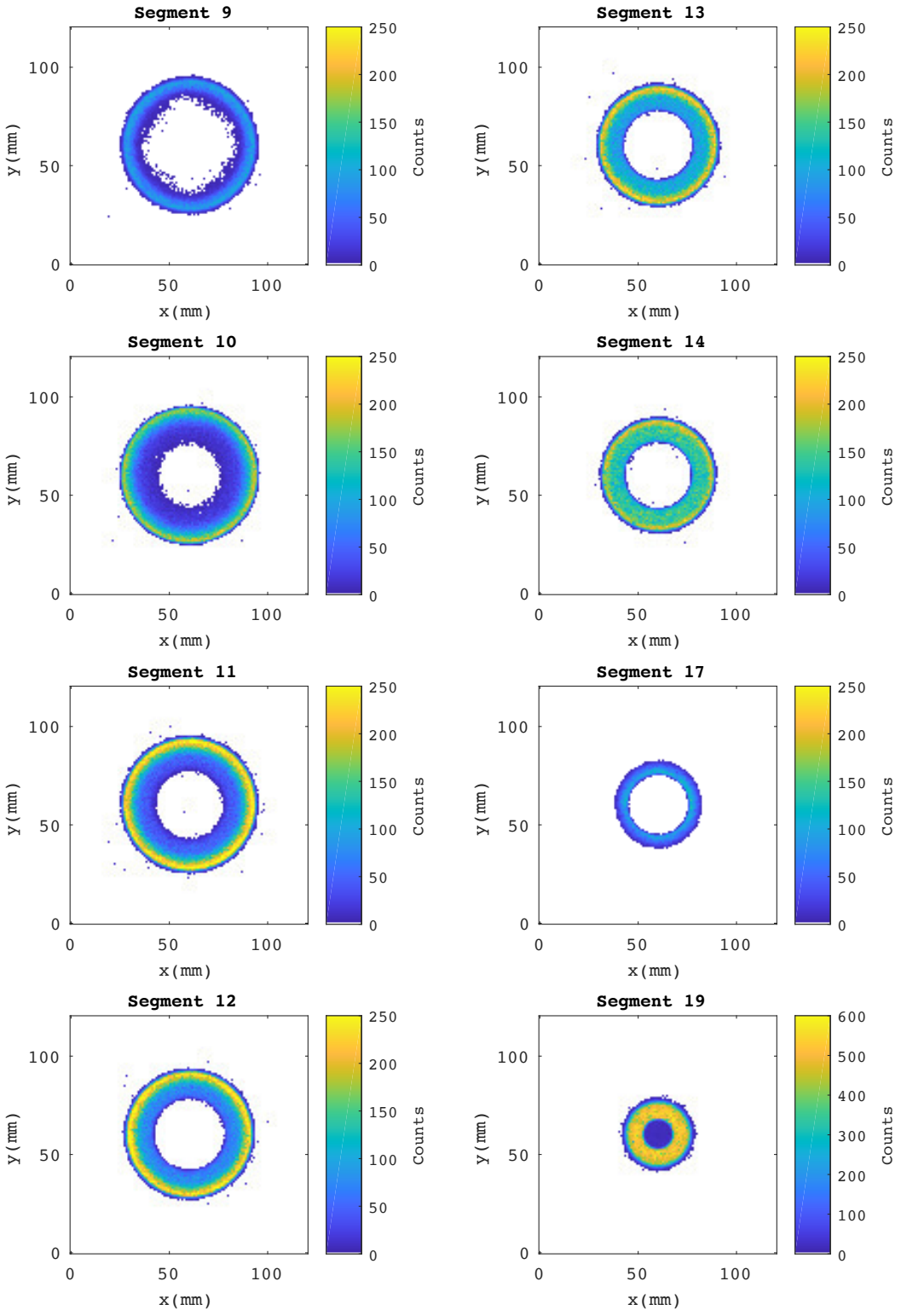


*Figure 3.20: Energy gated intensity matrix showing the number of counts per x-y position seen by segments 9-19.*

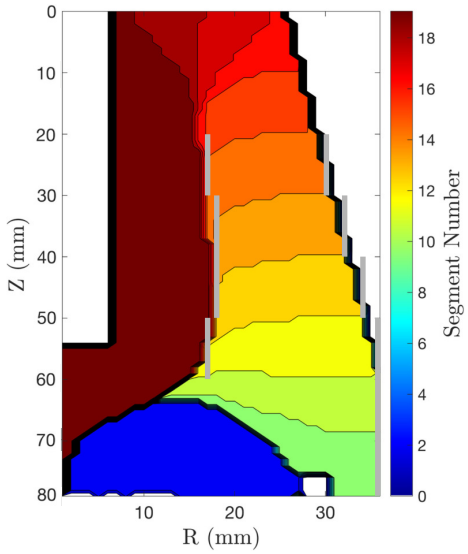


*Figure 3.21: The simulated secondary charge collecting electrode as a function of interaction position taken from [WHBB+18]. The grey lines have been added to represent the measured inner diameter of segments 11-14 and the measured outer diameter of segments 9-14.*

## 3.5 $^{137}$Cs Fold 1 Gated Singles Scanning

Fold refers to the number of segments in which interactions occur for a single gamma-ray event. Fold can therefore be used to select events that only interact in a single segment of the crystal using a "fold 1" gate. Two different methods of fold calculation are considered here to determine which method is best suited for use in future analyses.

### 3.5.1 Fold Calculation Methods

The first of the two methods used to calculate fold relies on analysing the pulses from the segments. This method, referred to here as the *segment fold*, examines all of the signals from the secondary charge collecting segments and uses a threshold, positioned above the baseline noise at $\sim$ 20 keV, to identify real signals against noise and image charges. The number of pulses which pass the threshold are counted and given as the fold value. This method is open to misidentifying single interactions close to segment boundaries in which the charge cloud is split between segments. It is also effected by crosstalk, whereby a signal is induced in a segment due to coupling with another segment in which a real signal did occur. This results is an artificially higher fold as two segments record a pulse for one interaction. Segment 13 is known to suffer from crosstalk for all events and as such has been removed for this analysis.

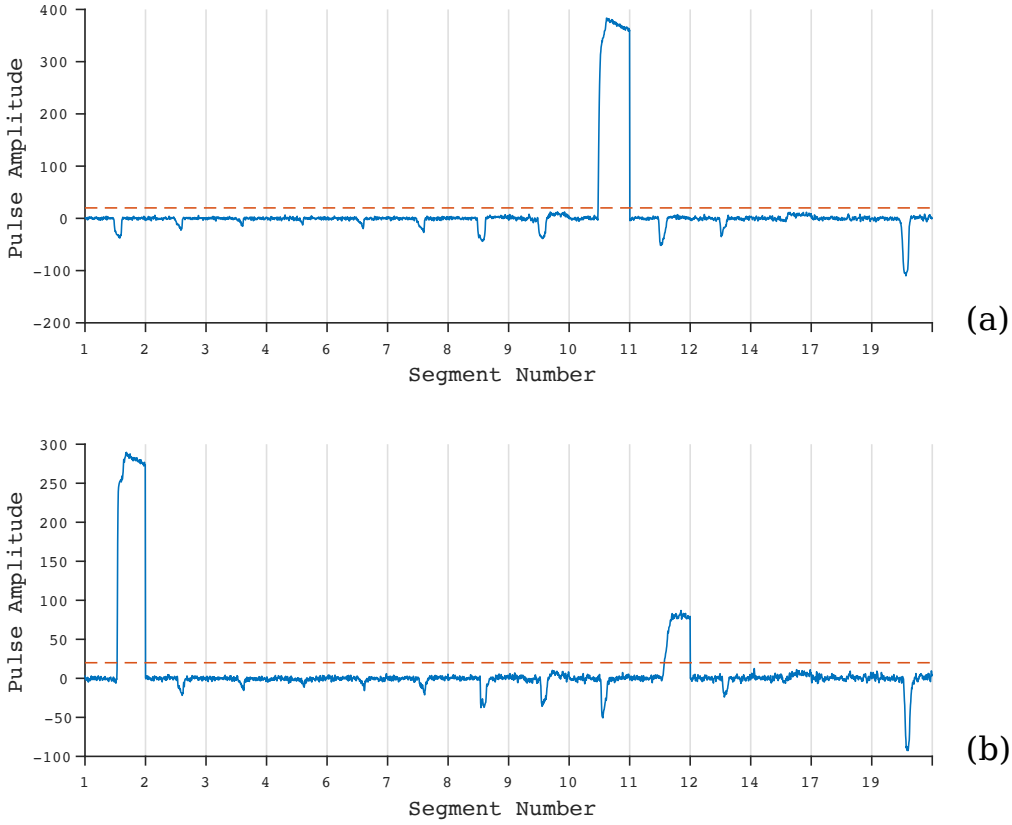


*Figure 3.22: Pulses from the segments with the 20 keV threshold shown in red for a fold 1 (a) and fold 2 (b) event.*

The second fold calculation method, referred to as the *pulse fold*, relies on the shape rising edge produced by the point contact of SIGMA, which allows multiple interactions to be identified from the point contact pulse, as described in [WHBB$^+$18]. The *pulse fold* is found by differentiating the point contact pulse, highlighting discontinuities in the rising edge which appear as peaks in the differentiated pulse, as shown in Figure 3.23. To identify the number of peaks in the differentiated pulse, and hence the fold value, a threshold of 25 % of the maximum amplitude of the differentiated pulse is applied. The peaks are then counted as the number of non-sequential elements which pass the threshold.

While this method can identify multiple events which occur in a single segment, unlike the *segment fold*, small secondary peaks can be missed due to thresholding and it is vulnerable to misidentifying the fold for events where the discontinuities occurs during the fastest part of the rising edge. In these instances, the secondary peak is embedded in the side of the larger peak and the small temporal space between the peaks does not pass below the threshold. Crosstalk has no effect on the point contact pulse shape, therefore crosstalk does not effect the *pulse fold* of an event.

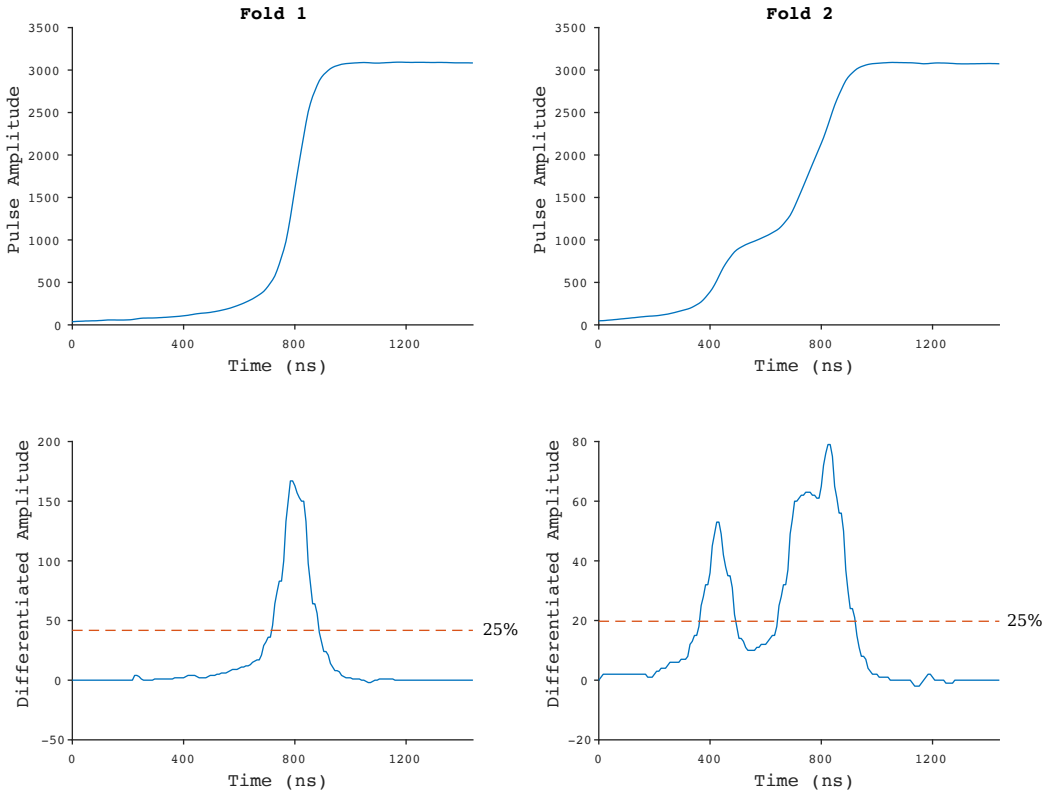


*Figure 3.23: The point contact pulse and its differential for events identified as fold 1 or fold 2 by the pulse fold method.*

#### 3.5.1.1 Segment Fold

Figure 3.24 shows the intensity matrix for the number of *segment fold* 1 events in Segment 6 as an example of the behaviour of the azimuthal segments. As with the energy gated matrices, there is an increase in counts to $\sim$ 700 relating to the area of the well compared to $\sim$ 200 in the main bulk of the segment. The slight increase in counts in the centre of the segment relates to the area at which the segment has the largest collection thickness. The counts drop at the rear edge of the segments due to the wrap around of Segment 9 and then increase outside of the crystal volume due to photons scattering into the segments from the holding structure around Segment 9. The background is removed by setting a limit of 40 counts, below which the pixels are displayed as white. The background removal gives well defined edges for most of the segments; the boundaries which segments 4 and 6 share with Segment 5 being the exception. This can be observed in Figure 3.24 on the right side of Segment 6 where additional counts are seen outside of the segments active volume due to Segment 5 not being instrumented. As *segment fold* counts the number of signals, any interactions in Segment 5 which scatter into another segment cannot be identified as a higher fold; this indicates that interactions in Segment 5 are most likely to scatter into the neighbouring segment, close to the segment boundary. For interactions which occur

at the segment boundaries, the charge cloud produced can be split and collected by both segments registering as *segment fold* 2 even though only a single interaction has occurred; resulting in a drop in counts at the segment boundaries.

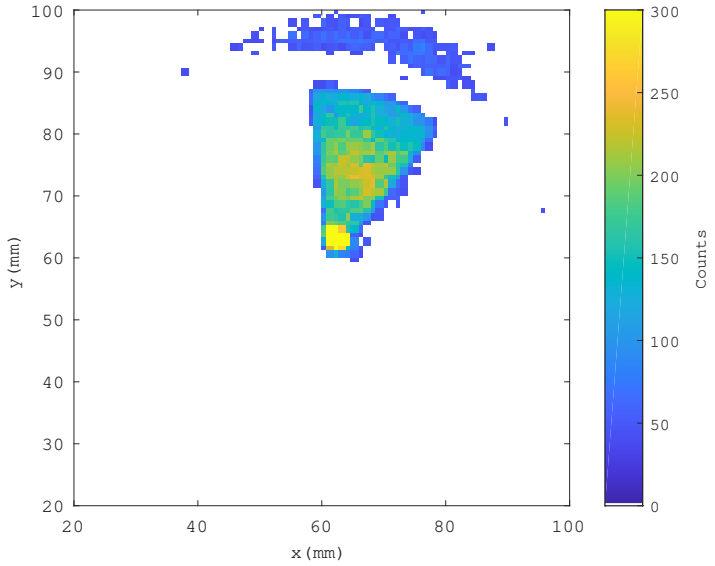


*Figure 3.24: Segment Fold 1 events in Segment 6.*

Using the *segment fold* 1 gate, segment 9-19 show the same shape as displayed in the energy gated matrices in Figure 3.20. They however have significantly higher background, removing the ability to clearly define the inner radius seen in segments 9-12. An example of this is shown in Figure 3.25 for segment 10. Segment 14 has significantly higher counts than the other longitudinal segments due to the removal of segments 13, 15 and 16, which neighbour Segment 14. Any interactions which occur in these segments and subsequently scatter into Segment 14 cannot be detected in this method of fold calculation and are included as fold 1.

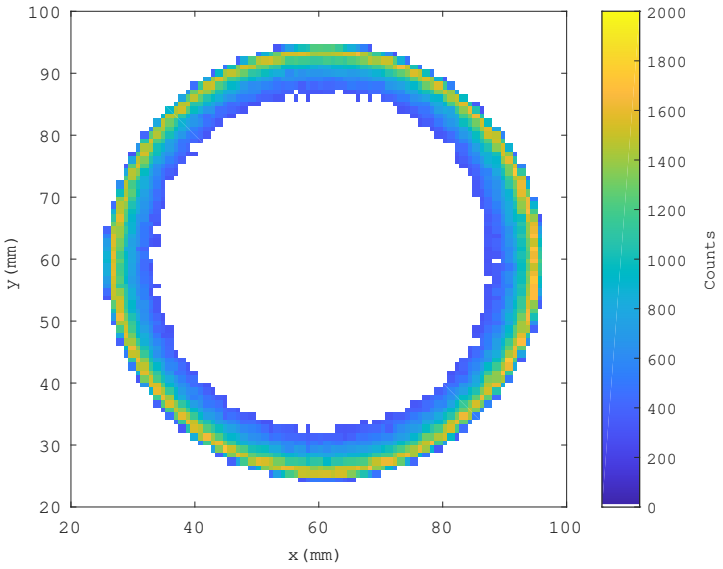


*Figure 3.25: Segment Fold 1 events in Segment 10.*

#### 3.5.1.2 Pulse Fold

The same intensity matrices have been produced for a *pulse fold* of 1. Figure 3.26 shows the number of counts per position for segment 6 with a background threshold of 120 counts. As with the *segment fold*, the sides of the segments are well defined and there are increased counts in the well. The main difference occurs in the handling of interactions at the outer edge of the crystal, in the wrap around area of Segment 9. Whereas the *segment fold* showed a sharp reduction in counts to background, the *pulse fold* shows a smaller reduction, going from $\sim$ 300 counts in the segment volume to $\sim$ 200 in the wrap around area. This suggests either the second peak produced by the differentiated pulse is too small to meet the threshold and is being missed by the fold calculation, or there is some element of charge sharing between Segment 9 and the azimuthal segments, which is registered as multi fold by the *segment fold* but does not result in a change in the pulse shape.

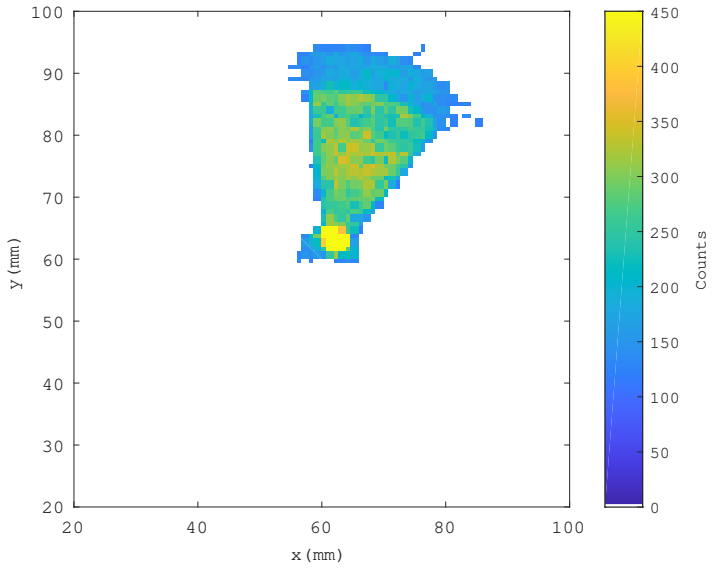


*Figure 3.26: Pulse Fold 1 events in Segment 6.*

Figure 3.27 shows the intensity matrices for segments 9 and 12 with a background threshold of 300 counts. Segment 9 shows a ring of reduced counts in the central area. This may relate to the contact boundary with the well contact though the inclusion of counts in the inner area suggests crosstalk between segments 9 and 19, resulting in counts registering in Segment 9 in an area of the crystal they should not. Segment 14 also seems to suffer from the same crosstalk issue with Segment 19. The outer diameter of the well is just visible in Segment 12 due to the thickness of the well contact, resulting in an area of inactive crystal. As with the external structures, interactions in this area cannot be detected and so scattering in this area cannot be removed.

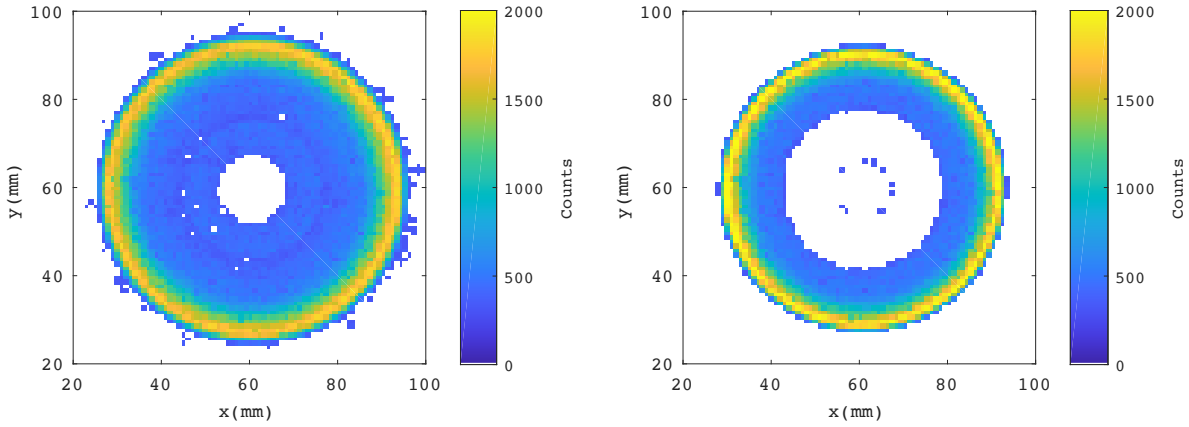


*Figure 3.27: Pulse Fold 1 events in segments 9 (left) and 12 (right).*

## 3.6 Fold evaluation

Having used two different methods to calculate fold and applied fold based gates to the data, differences in the performance of the *segment fold* and *pulse fold* have been displayed. The dimensions of the segments can be seen in both fold 1 gated methods, though the *segment fold* offers a sharper distinction between segment and background for the azimuthal segments. *Segment fold* was however effected by the non-instrumented segments, such as Segment 5, the effects of which are not seen in *pulse fold*. One of the benefits of trialling both of these methods has been the identification of crosstalk, as seen in segments 9 and 14. The biggest issue facing both methods is the handling of crosstalk between channels. The *segment fold* removes true fold 1 events which experience crosstalk and adds them to higher fold data, resulting in artificially lowered counts in fold 1. The *pulse fold* does not identify crosstalk and so can attribute a fold 1 event to two segments, including false interactions in the data. While no crosstalk corrections have been made to this data it is possible to, at least partially, correct for crosstalk and improve the performance of both of these fold calculation techniques. Without this correction, the choice in fold calculation method is based on the ability to identify interactions within the correct segment. As such *segment fold* will be used for future fold gating for the coincidence measurements as, though is results in a greater loss of events, the events which pass the fold 1 gate are always attributed to a single segment.

# 4 Coincidence Measurements

In order for pulse shape analysis to be effective in improving the position resolution of SIGMA, a library of preamplifier pulse shapes produced at known gamma-ray interaction positions must be generated. Preamplifier pulses measured in any future experimental work can then be compared against the library to determine the position of interaction. For detectors such as SIGMA, where a sub-mm position resolution has been predicted [WHBB$^+$18], [CRHL11], it would be impractical to gather experimental data for all possible locations in the detector. As such, a simulation will be used to generate the pulse shape database and experimental measurements used to validate the simulated database. The measurements also allow for a better understanding of the charge collection response through analysis of the preamplifier signal shape at various gamma-ray interaction positions in SIGMA. This chapter will focus of the creation of an experimental pulse library to be used for future simulation validation, using coincidence measurements.

## 4.1 Scanning system

The same scanning system as discussed in Section 3.1 was used to position a 0.7 GBq $^{137}$Cs source, encased in lead with a 80 mm long 1 mm diameter collimator and a 100 mm long 5 mm diameter collimator, perpendicular to the front face of the SIGMA crystal as shown in Figure 3.1 (c). A secondary set of lead collimators were positioned around the SIGMA cryostat, leaving 3 mm gaps at 4 set heights in the crystal. 32 bismuth germinate (BGO) detectors with a crystal diameter of 12.7 mm and height of 72 mm were placed in line with each gap, with 8 BGO detectors forming a ring at each selected height, as shown in Figure 4.1 (a) and schematically in (b). The collimated system is designed so that only gamma rays which scatter at close to 90$^o$, at one of the selected heights, are seen in coincidence in both SIGMA and a BGO detector as illustrated by the example in Figure 4.1 (b). The energy deposited in each detector for an interaction of this kind can be calculated using the Compton scattering formula, Equation 2.5, and for exactly a 90 degree scatter results in 374 keV being deposited in SIGMA and 288 keV in the BGO. To locate the front of the crystal within the cryostat, a collimated source was positioned in a plane parallel to the front of the crystal, and the detector slowly lowered until a response was seen.

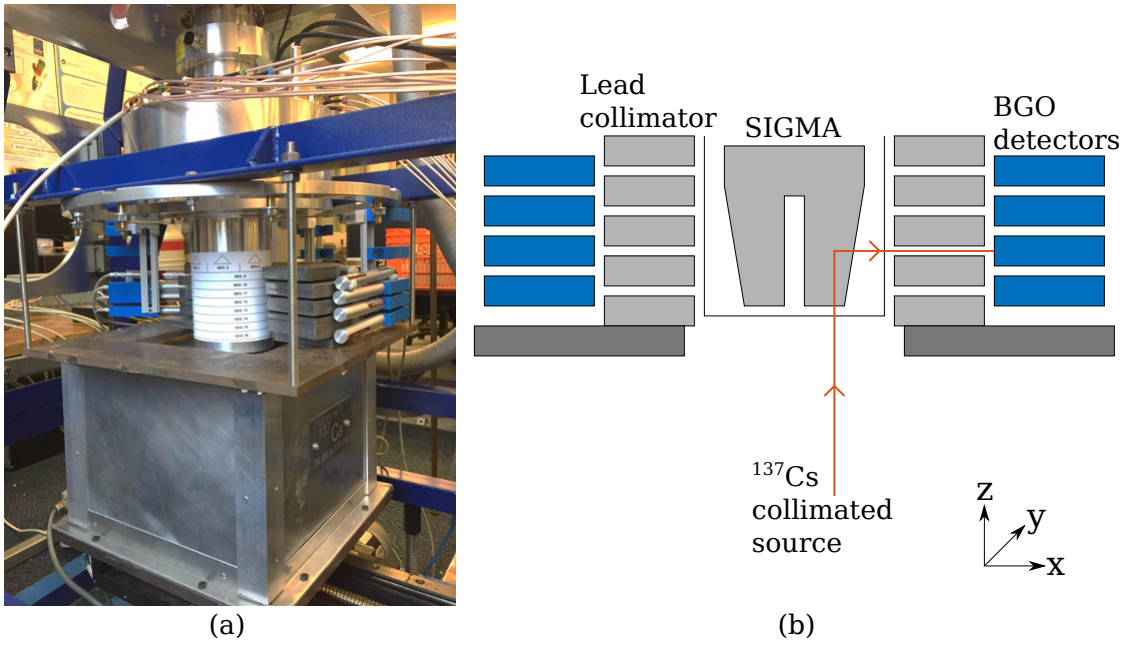


*Figure 4.1: Photograph showing coincidence scanning system for half of the detector (a) and a schematic of the same system (b).*

A total of 8 different depths in the crystal were achieved by moving SIGMA down 5 mm in the z-axis and repeating the data collection for the same x-y locations. Table Table 4.1 shows the depth, z, of each ring measured from the front face of the crystal and the spot size of the collimated gamma-ray beam at that depth, calculated based on a perfect collimator with no gamma-ray penetration. The BGO rings were aligned with the secondary collimator gaps to only allow scattered gamma rays from a single depth to enter. This means that the BGO number can be used to determine the depth of the interaction. There is a minimum distance required between depths, related to the physical width of the BGO detectors, so no two rings overlap.

| Depth (mm) | Width (mm) | Spot Size (mm) |
|---|---|---|
| 5.5 | 3 | 1.1 |
| 10.5 | 3 | 1.1 |
| 30.5 | 3 | 1.2 |
| 35.5 | 3 | 1.2 |
| 48.5 | 3 | 1.3 |
| 53.5 | 3 | 1.3 |
| 65.5 | 3 | 1.4 |
| 70.5 | 3 | 1.4 |

*Table 4.1: The depth and width of each collimated gap alongside the spot size of the collimated $^{137}$Cs beam at that depth.*

The collimated $^{137}$Cs beam was held at each x-y position for 6 hours with data acquired for 4 BGO depths simultaneously. After data were acquired for all of the

x-y positions of interest, the detector was lowered and data acquired at the same x-y positions for the remaining 4 depths. Data were collected at a total of 85 x-y positions with 8 depths, resulting in a total of 680 positions. Data were collected in linear and radial patterns as shown in Figure 4.2 (a)(b). The linear points were selected to examine the pulse shapes in the centre of the segments and at segment boundaries. The selected points are reflected in the x and y axis to confirm the symmetry of the crystal. The radial points were selected to examine the change in pulse shape with radial position and increasing radius, including an area of increased granularity to identify fine changes.

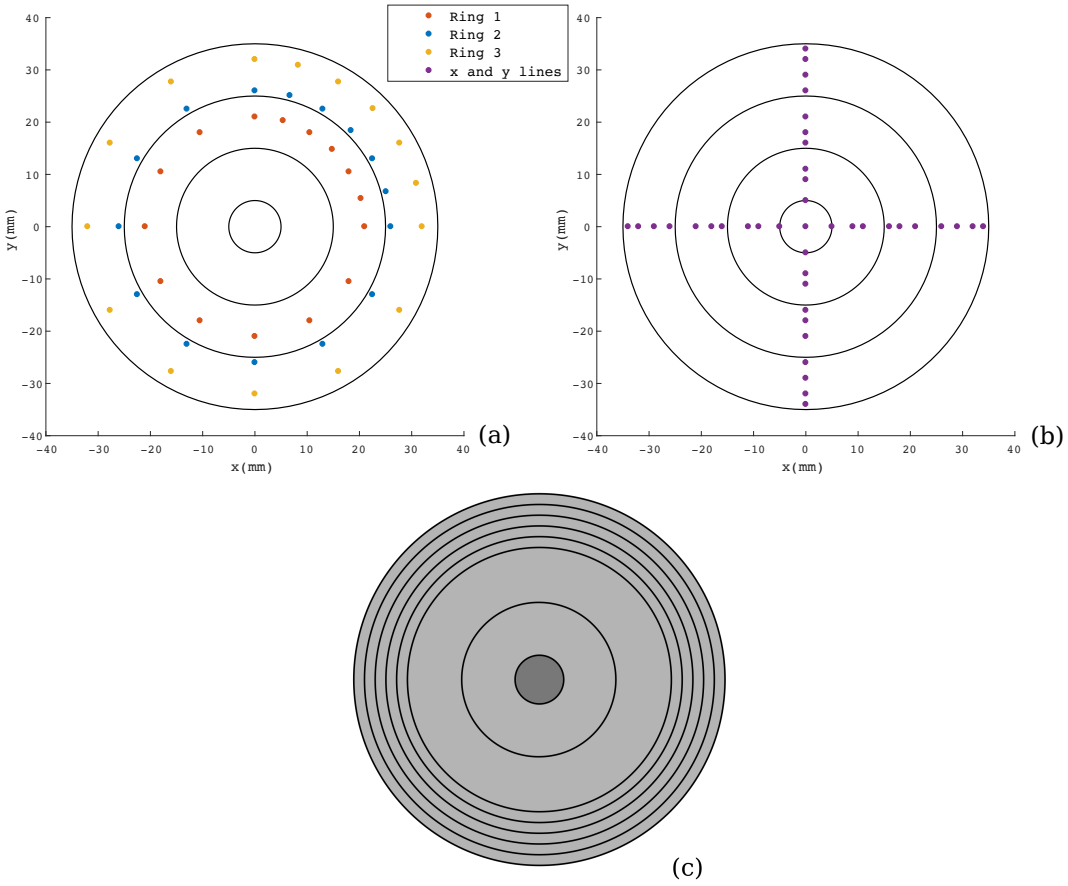


*Figure 4.2: x-y positions of the coincidence data showing the radial (a) and linear (b) patterns of the data. The black lines illustrate the outline of the crystal, front face, radial segment boundary and bore hole as shown in the schematic of the front face of the crystal (c).*

## 4.2 Data Acquisition system

Data were acquired using the same digital electronics system as the one used for the singles measurements, described in Section 3.2, with the addition of 32 BGO detectors as illustrated in Figure 4.3. The BGO detectors were individually connected to a preamplifier box which amplifies the signal and allows the gain of each detector signal

to be adjusted. The BGO preamplifier pulses were converted to a digital signal by the CAEN V1724 digitisers over a 20 $\mu$s window. As with SIGMA, a decimation of 4 was used, resulting in one sample each 40 ns. Each digitiser had 8 channels, meaning 3 were required for SIGMA and 4 were used for the BGO detectors. The system was operated in coincidence mode so that the system only triggered when the signal passes a threshold set just above the noise level in the point contact of SIGMA and a BGO detector within the 325 ns window. When the trigger requirements are met, all channels were written out to the DAQ via the V2718 VME to PCI optical link bridge and stored to disk. Data was processed post collection using mtsort [Jud19].

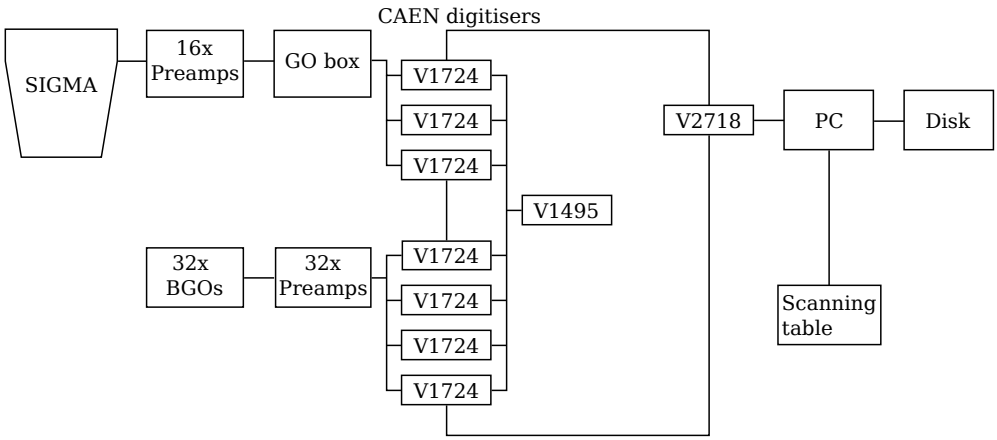


*Figure 4.3: Schematic of the electrical components used for the coincidence data acquisition.*

## 4.3 Data Analysis

The scanning system and the acquisition electronics were designed to maximise the number of single site events of interest. The collimation is designed to only accept near $90^o$ scatters and the coincidence triggering system only accepts events which occur in both SIGMA and a BGO detector within a small time window, reducing the chances of random coincidence events. Unfortunately even with these factors, not all of the data acquired met the event requirements of being a single $90^o$ scattered event. In order to produce an accurate average preamplifier signal response for each gamma-ray interaction location the unwanted data had to be removed. This was achieved by filtering the data and, once an average was formed, comparing each pulse to the average to identify significantly different pulse shapes. This process is described beneath.

### 4.3.1 Filters

The SIGMA and BGO pulses were acquired and stored to disk for off-line processing. It was at this stage that multiple filters were applied to remove events which were not the single site, with close to $90^o$ degree scatter, event-type required. To be accepted,

an event must have passed each of these gates:

**Multiplicity:** To ensure that all channels of SIGMA and the BGOs are written out for an event it must have a multiplicity of equal to the total combined number of channels of 48 (16 SIGMA channels plus 32 BGO channels). Figure 4.4 shows the multiplicity for a selection of events collected at multiple locations during the coincidence data collection. For the majority of events the data acquisition system works well, writing out all 48 channels when the system is triggered. There are also a small number of events where one or more channels are missing from the event and are registered as a separate event. This is due to timing issues in the digitisers causing some channels to appear to be outside of the timing window for an event and so registered as a separate event.

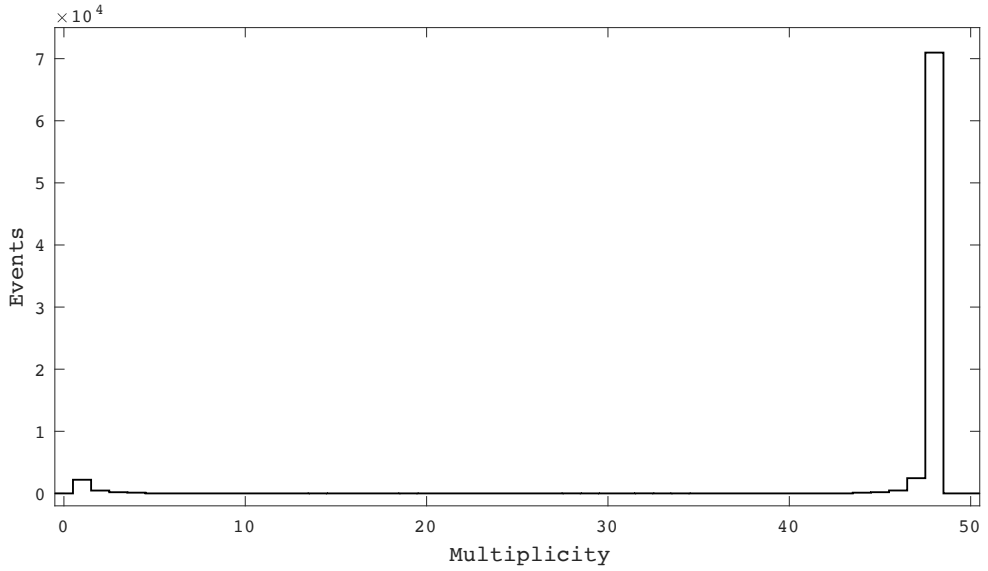


*Figure 4.4: The multiplicity of events recorded in the coincidence data collection.*

**Energy:** For a 662 keV gamma ray to scatter at $90^o$ it will deposit 374 keV in SIGMA and 288 keV if fully absorbed in the BGO detector. Figure 4.5 shows an example of the energy recorded in the point contact of SIGMA and the energy in the charge collecting BGO detector integrated over multiple positions. The SIGMA energy spectrum shows two peaks, one at 374 keV relating to $90^o$ scattered events and one at 662 keV relating to full energy absorption events. The BGO spectrum shows a peak at 288 keV relating to the full absorption of the $90^o$ scattered events. The 2D energy matrix shows that the majority of events which deposit the energies of interest for this scattering process do so in both detectors at the expected energies, confirming the interaction mechanism. The 662 keV events in SIGMA are also highlighted in the 2D matrix due to the high number of events resulting in a high number where a background event is also detected in a BGO detector within the timing window for the event. A wide coincidence timing window was required due to SIGMA's slow signals relative to the BGOs. An energy

gate of 374 keV ± 20 keV was used for SIGMA and, due to the poorer intrinsic energy resolution of the BGO detectors, a wider energy gate of 288 keV ± 80 keV was required for the BGOs. This led to the acceptance of only events which meet both of these gates as represented by the red box in Figure 4.5.

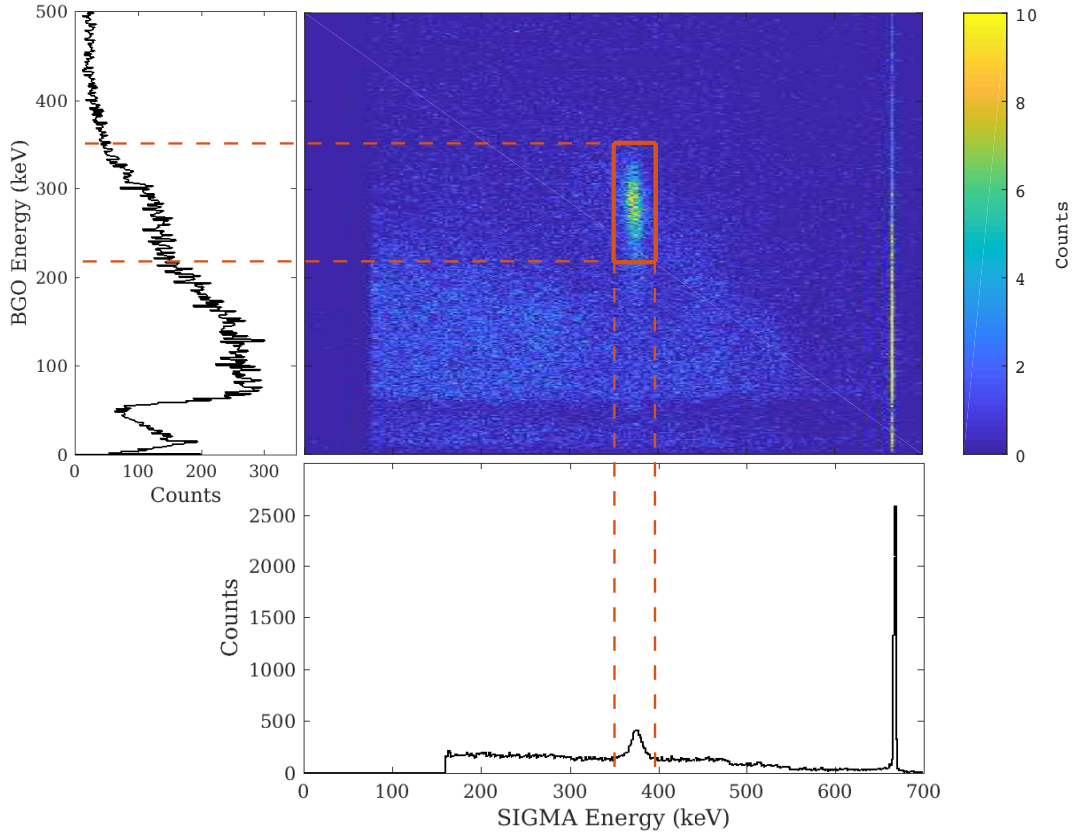


*Figure 4.5: The energies measured in the point contact of the SIGMA detector and the BGO detectors. The energies are displayed in both spectra form and as a 2D matrix of events. The red dotted lines represent the energy gates applied to each detector system, forming the red box which illustrates the accepted events.*

**Fold:** Fold gates were applied to SIGMA and the BGO detectors separately using the *segment fold* as described in Section 3.5. Only single site events were wanted in SIGMA, which should deposit their energy in a single segment, as such a gate of fold 1 is applied. When a gamma ray scatters in SIGMA into a BGO it should only be seen in one BGO, so a fold 1 gate was applied to the BGO detectors. Figure 4.6 (a) and (b) shows the spread in BGO and SIGMA fold respectively for a selection of coincidence events. The majority of events are fold 1 with sharply declining number of events at higher fold. There are also some fold zero events where an interaction has enough energy to trigger the data acquisition system but the energy is not high enough above the noise level to be considered significant in the data analysis. The number of fold zero events is higher in SIGMA where the low noise point contact is used as the data

acquisition trigger, but the outer segments are used to calculate fold. This means the noisier outer segment signals have not passed any threshold leading to a large number of events being removed at this stage.

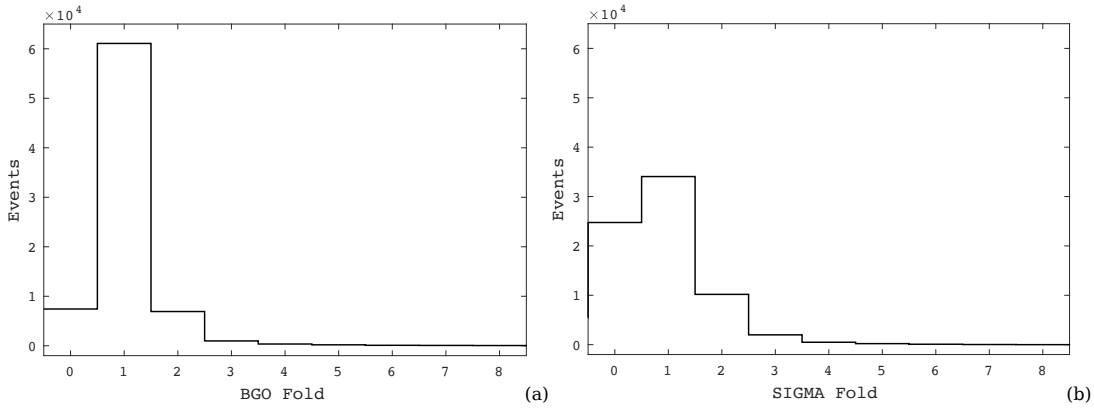


*Figure 4.6: Histogram of the event fold in the BGO detectors (a) and the SIGMA detector (b).*

**BGO ID:** While this was not used to reject any events, it was used to differentiate events by depth, z, at which they occurred. As each ring of 8 BGO detectors were aligned with one collimator gap, each BGO ID is associated with a specific depth.

Applying these gates significantly reduces the number of events to around 4 % of those which initially triggered the data acquisition system. Some unwanted events which do not interact in the required mechanism however still remain. These unwanted events were removed in the next stage of processing by creating an average pulse and comparing each event to it to highlight any remaining unwanted events.

### 4.3.2 Average Pulse Formation

Of the events which remain after filtering, the pulses rise start at different points within the digitised sample window due to baseline noise, which causes jitter, and walk [TL15]. Before an average can be created, the pulses must be time aligned. This is done by assigning a start time to each event and shifting all of the start times to a fixed temporal point. The start time for the event is calculated from the secondary charge collecting segment as charge is collected faster in these segments than the point contact. The point at which the pulse reaches 5% of the maximum amplitude for the event is used as the estimated start time as 5% is the lowest level of the pulse which can be consistently identified above the noise level.

Once the pulses are time aligned, so the point at which the pulse from the secondary charge collecting segment reaches 5% of its final amplitude relates to the same sample number in each pulse, all of the pulse arrays are added together summing the pulse

height for each sample. An initial average pulse is created by dividing this total height array by the total number of pulses. Each individual pulse is then compared to the initial average by subtracting the pulses from one another and calculating the average difference per sample. As the total recorded pulse length is long compared to the risetime of the pulses, sample comparison was made over a smaller selected region rather than the full pulse, to cover the rising edge of each pulse or the full image charge. This prevents any small fluctuations in the baseline noise from swamping the average difference per sample and masking differences in the rising edge. Figure 4.7 (a) shows the average difference per sample when the full 28 $\mu$s pulse is compared to the initial average. There is only one distinct peak present and gating on that peak to only include pulses with an average difference per sample of less than 20 results in the final average pulse shown in yellow in (b). This final average clearly is not a good representation of the pulse behaviour at this location and the pulses being accepted and rejected, shown in green and red respectively, show little correlation. Figure 4.7 (c) shows the average difference per sample when the pulse is compared to the initial average over a 4 $\mu$s window centred on the rising edge. Two peaks are now visible with good separation and, with a threshold of below 50, the accepted and rejected pulses shown in (d) show good correlation with all of the accepted pulses being similar in shape and all other pulse shapes rejected.

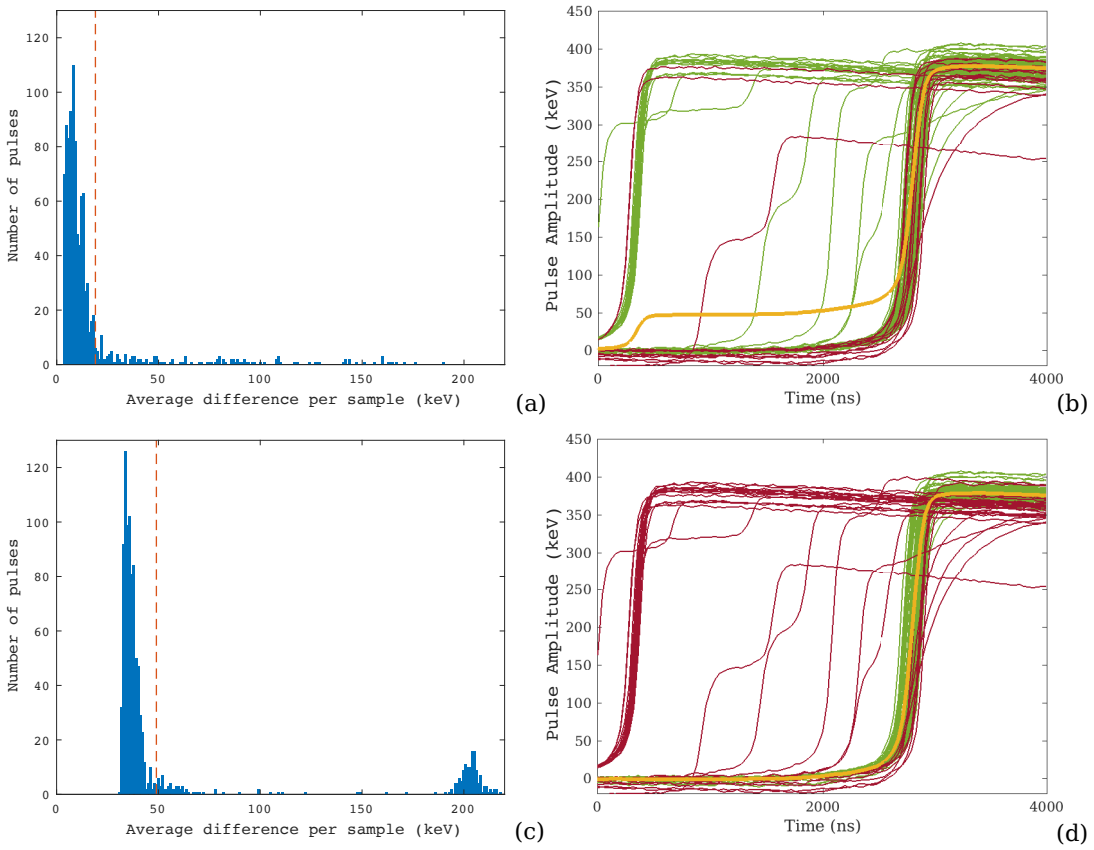


*Figure 4.7: The average difference per sample when comparing the full pulse (a) and a 4 μs window centred on the rising edge (b) to the initial average for the point contact. The accepted (green), rejected (red) and final average (yellow) pulses when setting limits based on the full pulse (b) and a 4 μs window centred on the rising edge (d).*

The last step used to remove unwanted events was to set limits on the maximum accepted average difference per sample. The limits were set to only accept pulses which showed the smallest difference from the initial average and refined until accepted pulses looked suitably similar visually. For the point contact and secondary charge collecting segment, a limit of below 50 was used. A lower limit of below 30 was used for the image charges as they are significantly smaller pulses. These limits were chosen by examining the spread in pulse difference for multiple positions. While these limits were used in most instances, each pulse was checked and, if required, the limits were adjusted to compensate for differences in the shape, size and position of accepted pulses compared to the unwanted pulses. The pulses which passed this final filter were used to create the final average pulse, which will be used as the average response of the detector at that position.

The average difference per sample is plotted in Figure 4.8 (a,b,c) for the 3 types of pulse examined, the point contact (a), an image charge (b) and a secondary charge collecting segment (c). Viewing the difference between individual pulses and the initial average in this way indicates that most of the pulses are similar in shape, forming the

large peak seen below the accepted pulse limit illustrated by the red dotted line for all three pulse types. A second smaller peak is also seen well above the limit, most notably in the point contact (a) and secondary charge collecting segment (c). Few pulses were collected in between the two peaks, suggesting that the rejected events may be similar in shape. This is investigated by viewing the accepted and rejected pulses.

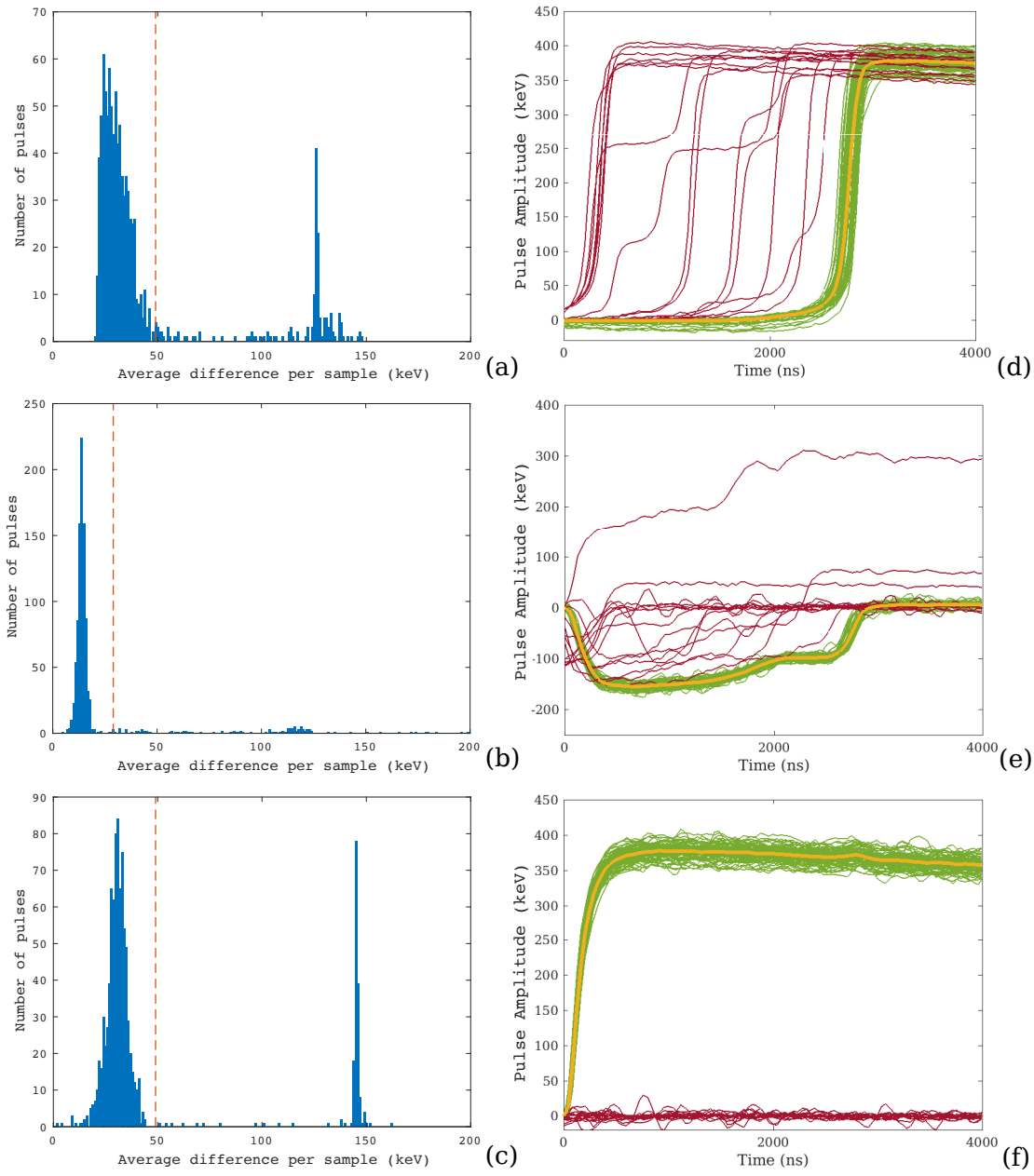


*Figure 4.8: The limits used to determine which pulses are accepted and rejected based on the level of difference from the initial average for the point contact (a), an image charge (b) and a secondary charge collected in the secondary charge collecting segment (c). A sample of 100 of the pulses either accepted (green) or rejected (red) and the final average pulse (yellow) for the point contact (d), an image charge (e) and a secondary charge collected in the first hit segment (f).*

The yellow plot in Figure 4.8 (d,e,f) show the final average preamplifier pulse alongside a sample of 100 accepted (green) and rejected (red) pulses. The secondary charge collecting segment is used to align the pulses so the rejected pulses in (f) are all from

events where the secondary charge is collected in a different segment. The similarity in shape of the rejected pulses compared to the accepted pulses causes the peak in rejected pulses shown in (c). For the point contact and the image charge, many of the rejected pulses are the same shape as the accepted pulses but misaligned. The misaligned pulses for the point contact all occur before the aligned pulses, were the average is close to zero. This results in the rejected pulses having a similar average difference per sample as seen in the rejected peak in (a). The stepped pulses in (d) show that many of the rejected pulses from the point contact resulted from multiple interaction events which the fold gating parameters failed to remove. Multiple interaction events can be easily identified by a flattening in the rising edge followed by a further rise. The flattening is caused by the charge from the first interaction being collected, the pulse then begins to rise again as the second interaction charge approaches the point contact.

By using an average pulse, the baseline noise seen in a single pulse can be suppressed. The degree of noise reduction is dependent on the number of pulses averaged, as shown in Figure 4.9. With increasing number of events, the size of the peak to peak noise declines rapidly to begin with, before slowing and appearing to level off after 600 pulses. In the first 100 pulses the noise is more variable pulse to pulse due to the greater statistical influence of noise in a single pulse. All of the average pulses created in this analysis contain 500 - 1000 pulses, putting them into the low noise area. A maximum upper limit of 1000 pulses were used due to limited disk space and timing considerations for data processing.

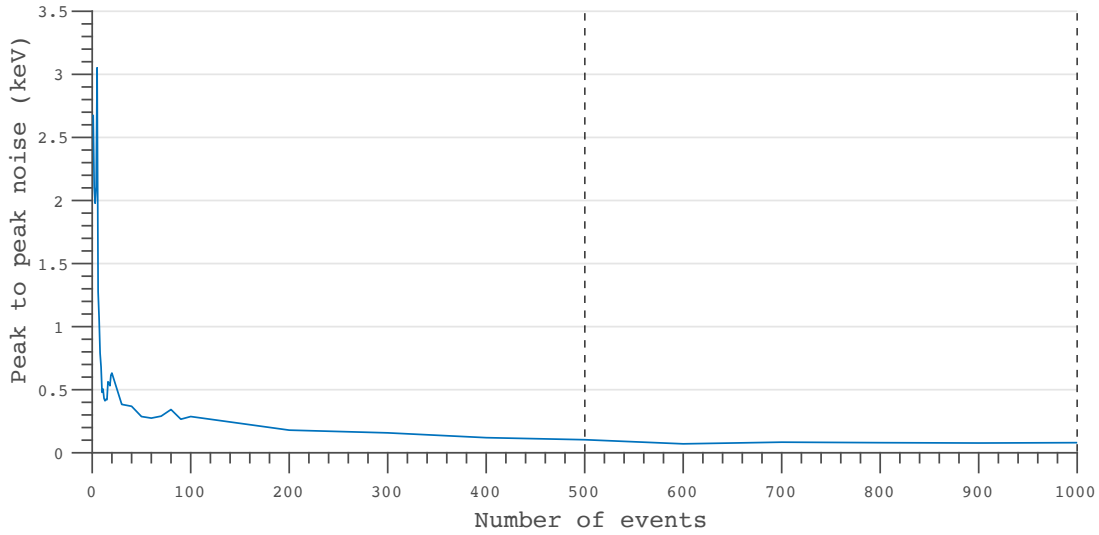


*Figure 4.9: The peak to peak noise in the average pulse as a function of the number of pulses used to create the average.*

The number of pulses that pass the filters and are therefore used to form the average, changes with gamma-ray interaction position in the crystal. There is also a reduction in

counts with increasing depth from the front face of the crystal as the 662 keV photon beam is attenuated (Section 2.1). Due to the taper of the crystal, the reduction in counts is non-uniform. The radius also affects the attenuation of the scattered 288 keV photons, as interactions at lower radii travel longer paths within the crystal than those scattered at high radii and therefore undergo greater attenuation. This attenuation has a greater effect than the taper of the crystal due to the lower energy of the scattered photons.

When forming the average pulse, locations close to the segment boundaries result in a lower number of pulses, as the beam divergence means events are split between multiple segments. The number of pulses used to form the average also declines with depth due to the reduction in the effectiveness of the pulse alignment process, shown in Figure 4.10. As the depth increases, both the number of multiple interaction pulses and the number of pulses which are similar in shape, but not aligned, increases for the point contact. The segment pulses show that, with depth, the number of full energy events collected by the secondary charge collecting segments reduces due to the increased probability of scattering with depth. As there is no energy gate on the secondary charge collecting segments, these events, where the charge has either been split between multiple segments or collected in a different segment, are not removed and result in an inaccurate start time.

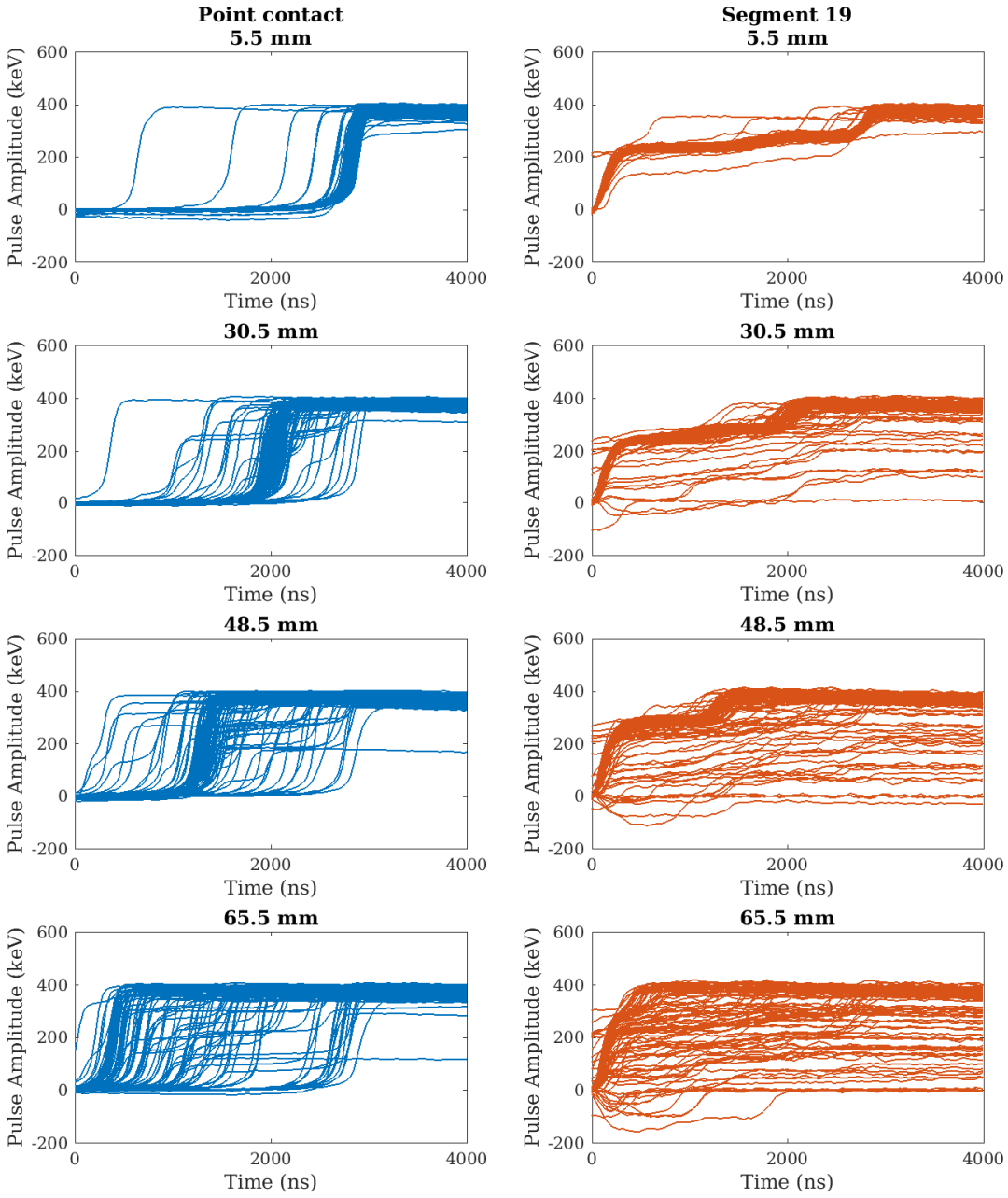


*Figure 4.10: Illustration of the effectiveness of the time alignment of point contact pulses (blue) and the first hit segment, Segment 19, used for the time alignment (red) with depth.*

## 4.4 Average Super Pulses

Coincidence measurements were taken at 680 x-y-z positions within the crystal volume, in linear and radial patterns, as shown in Figure 4.2. Average super pulses were created to show the average response in each segment simultaneously for a location. This section will focus on examining the key features identified in the average super pulses.

### 4.4.1 Linear Data

The linear scans consist of 2 lines through the centre of the detector at (x,y = 0,0). Each line consists of 21 (x,y) points with a shared central point at (0,0), as shown in Figure 4.2 (a). The points are spaced symmetrically around the centre line of the detector with the spacing designed to investigate areas of particular interest such as the segment boundaries.

Moving in a single dimension, a change in superpulse shape is seen with scanning table position. The greatest change in superpulse shape is observed in events in which the secondary charge carriers are collected in different segments. For events which occur in the same segment, a measurable difference is still seen, with events with a greater physical difference in location showing a greater difference in pulse shape. An example of this is shown in Figure 4.11 where (a) displays 3 superpulses generated for the (x,y) locations shown in (c). The superpulse is displayed as 1000 ns of each pulse from all working segments. All 3 locations are positioned on the y = 0 line and at the same z depth (z=5.5 mm) in the crystal (i.e. the same BGO ring). On this scale it is difficult to see any obvious visual differences in the pulse shapes. To make the differences clearer, the super pulses for (-18,0) and (-16,0) are subtracted from (-21,0) and the differences plotted in Figure 4.11 (b) along side the highest noise level recorded for a single interaction in any of the segments. The difference in most of the segments is below the noise level with only the point contact, Segment 17 and Segment 19 being notably above the noise level for both locations. This is as would be expected for the azimuthal segments (1-8) as there has been no angular change in position. The change in signal shape for the longitudinal segments (9-16), though small, increases the closer the interaction is to the longitudinal segment. Examining the point contact and Segment 19, where the largest change is seen, it is clear that the difference in pulse shape is similar in shape for both locations with the larger separation of the events resulting in a larger difference. This means that while the point contact shows the greatest change, other segments including the secondary charge collecting segment and the well contact (Segment 19) can be used to identify the (x,y) position of gamma-ray interaction events. The difference in pulse shape is significantly above the noise threshold for these events meaning differentiation of events with even smaller spatial difference may be possible.

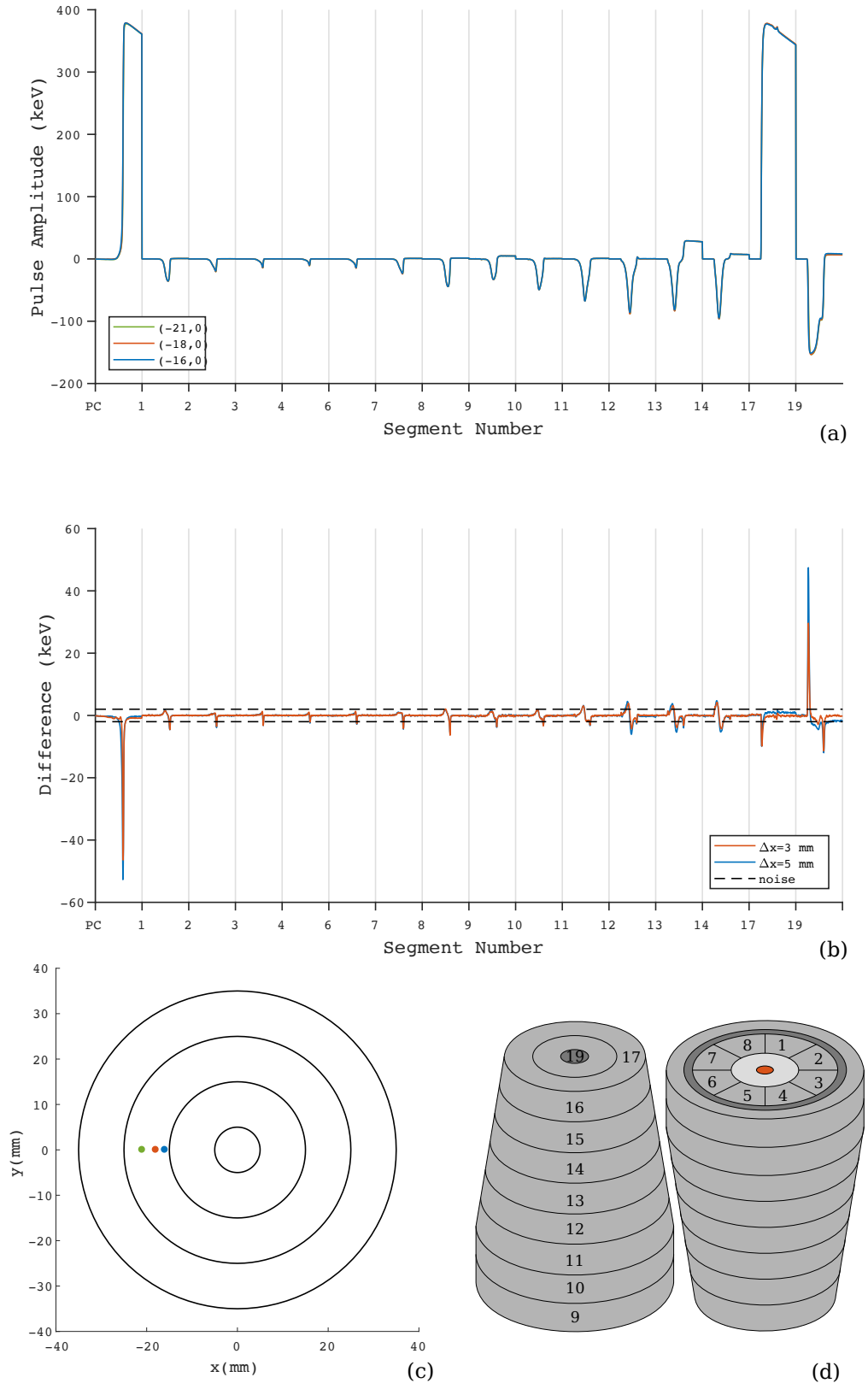


*Figure 4.11: Three average superpulses with the same y-z locations (a), the difference between these pulses (b). The locations of the three superpulses relative to the front of the crystal (c) and a schematic of the segmentation scheme of the crystal (d).*

Across all of the data points the closest event positions are a distance of 2 mm away in one dimension. For the superpulses at this location, a measurable difference is seen in the pulse shapes of at least 2 segments. An example of this is shown in Figure 4.12 where (a) displays 2 sets of pulses, each 2 mm apart, which are collected in different segments, the positions of which are shown in (c). As there is visually little difference between the pulses, they have been subtracted from one another and the difference plotted in (b). As this example only includes a change in the x position there is no angular or depth change so as expected the pulses produced in the azimuthal and longitudinal segments show very little change with segments 1-14 all below the noise threshold for both sets of positions. For the positions for which signals are collected by Segment 17 only the difference in the point contact and Segment 19 pulses is above the noise level. This means for fine position resolution the image charge created in a neighbouring segment, Segment 19 in this case, may offer more position information than the pulse from the secondary charge collecting segment. For the positions for which signals are collected by Segment 19, change above the noise level is seen in the point contact, Segment 17 and Segment 19. The difference observed in Segment 19 for the positions for which signals are collected in Segment 19 is smaller than the difference seen in Segment 19 for the positions for which signals are collected in Segment 17 showing a greater rate of change in the pulse shape produced in Segment 19 for events collected in a neighbouring segment. This effect is also identified in Segment 17 where the change is greater for the positions for which signals are collected in Segment 19 showing that the image charges produces in neighbouring segments may have greater position dependence than the secondary charge collecting pulses. Overall a difference is seen well above the noise level in at least 2 segments for both positions at 2 mm separation. This is a promising indicator that a difference could be identified between pulses of even smaller separation and that SIGMA may achieve sub mm position resolution. The magnitude of the differences for both sets of positions being different and the ability to differentiate a third segment above the noise level for the positions collected in Segment 19 also indicates that the position resolution is likely to vary across the crystal with different levels of pulse variation with position.

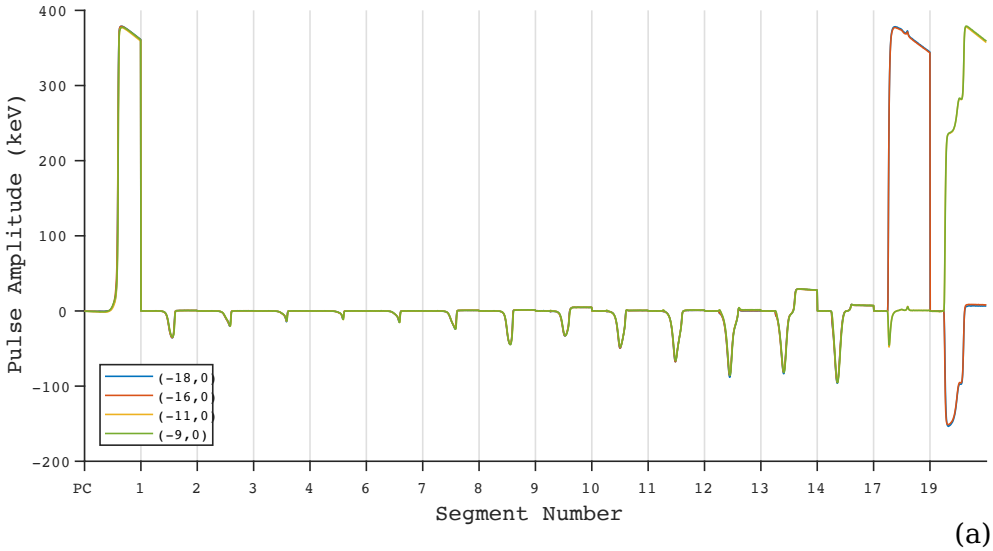


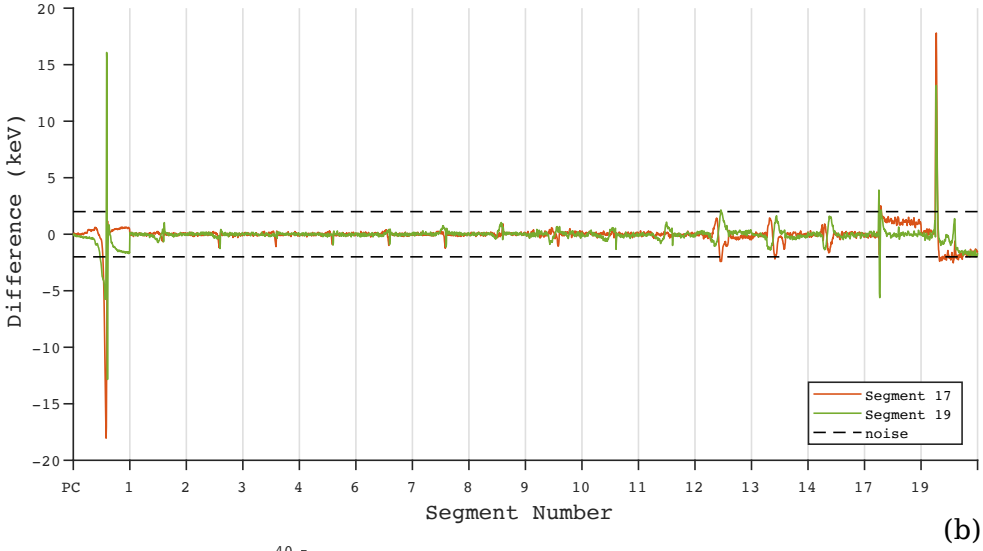


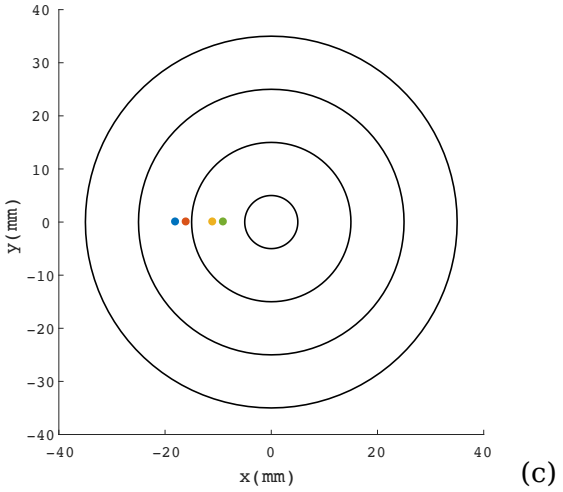


*Figure 4.12: Four average superpulses at a set y-z location (a). The difference between superpulses with a 2 mm separation in x for events collected in Segment 17 and 19 (b). Locations of the four superpulses relative to the to the crystal (c).*

Further examination of the image charges produced in the azimuthal segments for the linear positions reveals that the maximum amplitude of the image charges remain almost constant when there is no change in radial position and show a high degree of symmetry about the centre of the detector. An example of this is shown in Figure 4.13 (a) where the image charge amplitude is displayed for 4 of the azimuthal segments for interaction positions in a line through y=0 mm for a constant depth, z=5.5 mm. At either side of the centre point of the crystal (x=0) the size of the image charges remains constant for each segment with a change about the centre due to the change in radial position. When the interaction position moves from one side of the centre point to the other, the maximum amplitude of the image charge in one azimuthal segment switches to the azimuthal segment directly opposite. This is seen in Figure 4.13 (a) for segments 2 and 6 and segments 4 and 8 which are directly opposite each other as shown in Figure 4.13 (b). This reflection confirms the symmetry of the detector and that the azimuthal segments all operate in the same way.

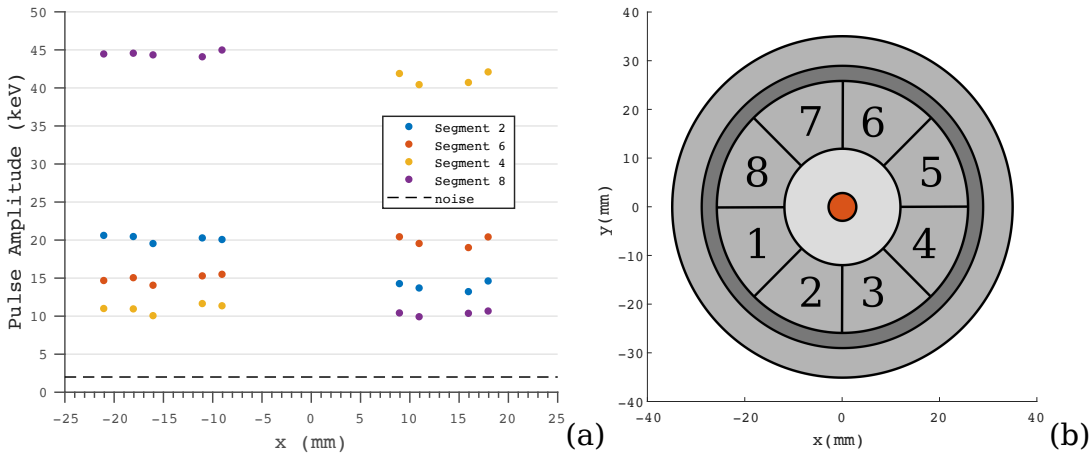


*Figure 4.13: The maximum amplitude of the image charges induced in 4 of the azimuthal segments for a line of data points at y=0 mm at a single depth, z=5.5 mm (a). The x-y position of the azimuthal segments when the crystal is view from the front (b).*

The linear positions were collected over multiple z depths in SIGMA to examine the change in pulse shape with depth in the crystal. For events that occur deeper in the crystal and further from the front face, the distance that the charge must travel to the point contact is reduced. This results in reduced drift times for the point contact. Example superpulses for events which occur at two different radii, r=-11 mm and r=-21 mm are shown in Figure 4.14 (a) and (b) with the locations of the events within the crystal shown in (c). As with the variation in x and y position, the events in which the secondary charge is collected in different segments show the greatest change with location. At small radii however, the active volume of Segment 19 extends most of

the length of the crystal meaning all 3 depths shown here are collected by a single contact. This is as expected from the simulation produced in [WHBB$^+$18] which gave the expected secondary charge collecting electrode is shown in Figure 4.14 (d). For both sets of depths, the image charges show a similar response. The azimuthal image charges maintain the same relative size to one another with depth as no azimuthal change in position has occurred. They also start earlier and reduce in size and width with depth. The earlier start time with depth is due to the increased proximity to the back of the crystal, and so the azimuthal segments, meaning the charge is seen by the azimuthal segments earlier. The reduction in signal size and width with depth is due to the reduction in time the holes spend drifting through the weighting potential of the azimuthal segments. For events closer to the front face of the crystal the holes spend more time drifting through the weighting potential of the azimuthal segments and start in an area of lower weighting potential resulting in a slower leading edge due to the weighting potential changing more slowly in this area. With increasing depth there is also a reduction in the number of image charges seen in the longitudinal segments as image charges are only created in segments which the primary charge carriers drift past on their way to be collected by the point contact. For events which are not collected by the well contact, for example those shown in Figure 4.14 (a), the image charges produced in Segment 19 have very similar start times and shape with a reduction in the size and width of the image charge with depth. The similarity in start time is due to the size of the well contact meaning all 3 event locations are a similar distance from the well contact. The similar shapes indicates a shared path which the holes take past the well contact to the point contact. All image charges show a shape increase as the holes begin to move through the weighting potential of the well contact. This is larger for events nearer the front face as they spend longer travelling through this area. The size of the image charge then reduces as the holes drift around the back of the well and away from the well contact. As they move towards the centre of the detector the weighting potential remains constant resulting in the plateau seen before the image charge falls rapidly as the holes drift towards the point contact.

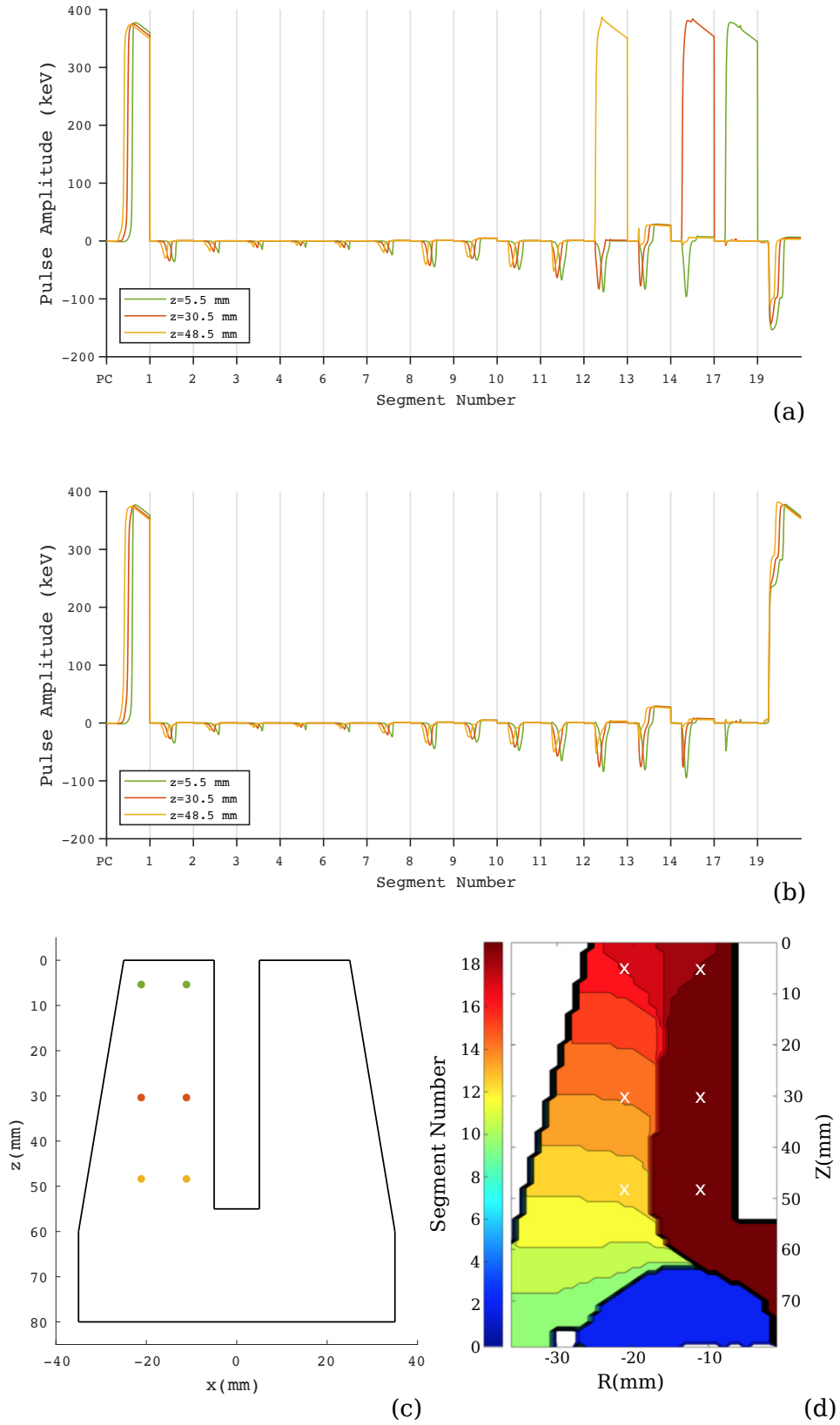


*Figure 4.14: Three average superpulses with the same x-y locations at a larger radius, r=-21 mm (a) and within the active volume of Segment 19 at r=-11 mm (b). The location of these points (c) and the expected collecting electrode from [WHBB+18].*

For events which occur at different depths in the active volume of Segment 19 the differences in the secondary charge collecting segment are more subtle. To view the change with depth more clearly, the point contact and Segment 19 pulses from Figure 4.14 (b) are shown in Figure 4.15. For the point contact pulses, a very clear separation is visible due to the significant difference in drift time with depth. The Segment 19 pulses, as the secondary charge collecting segment, have been used to identify the start time of the events. As such the start of these pulses are time aligned. The pulses continue to show good alignment until they reach around half of the final pulse amplitude. At this point significant differences appear based on the position of the event. Events closer to the front face of the crystal take longer to reach their full amplitude. This is due to the presence of the primary charge carriers, holes, moving towards the point contact. As the holes pass through the weighting potential of Segment 19 they induce a transient negative charge on Segment 19. All pulses show a fast initial increase in amplitude as the secondary charge carriers move towards and are collected by the well contact. The initial plateau seen in the pulse is the sum of the positive charge collected by Segment 19 and the negative image charge produced by the holes as they drift through the weighting potential of the well contact to the point contact. This takes longer for events closer to the front face of the crystal. The pulse amplitude them increases again as the holes move away from the well contact, towards the point contact. The pulses in Segment 19 only reach their full amplitude once the holes have been collected by the point contact.

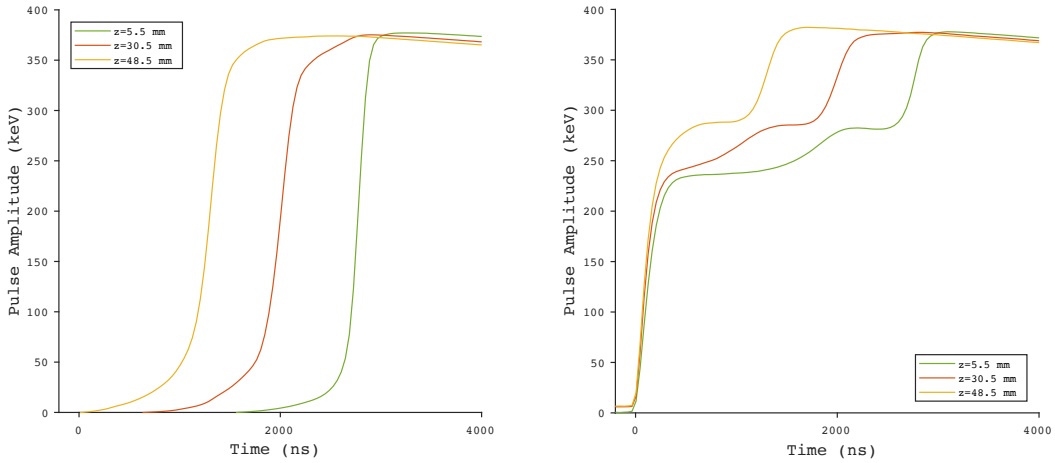


*Figure 4.15: A zoomed in view of the point contact pulses (left) and the Segment 19 pulses (right) from the superpulse shown in Figure 4.14 (b).*

### 4.4.2 Radial Data

The linear data has shown that by individually changing either the x, y or z location of an event, a measurable difference in the average superpulse can be observed. This section will look at the difference observed between positions with the same radial

distance from the centre of the detector. The radial data set relates to 3 rings of data at set radii centred at (0,0). Each ring consists of 15 points equally spaced at 30 degree intervals with a $90^o$ area of increased granularity. The positions of the rings relative to the crystal are displayed in Figure 4.2.

For most locations in the detector, events that happen at the same radius and depth will be collected by a single secondary charge collecting segment. An example of this is shown in Figure 4.16 where two superpulses for events $90^o$ apart are plotted (a) along with the difference between the two pulses (b) and their locations relative to the crystal (c). For azimuthal change, the biggest difference in the average pulse is seen in the point contact and the azimuthal segments as expected. In this example the first point is located at the boundary of segments 1 and 8 and the second point at the boundary of segments 2 and 3 as defined in Figure 4.16 (d). This results in the largest change in the azimuthal image charges being in segments 8 and 3 followed by 1 and 2. The longitudinal and radial segments show little difference compared to the noise level, including Segment 17 in which the secondary charge was collected. Due to the azimuthal change, the number of segments in which the difference is greater than the noise is significantly higher than the 3 seen in the linear change though the magnitude of the difference is smaller in this case. This means that for similar magnitudes of difference the radial positioning may offer greater accuracy as there are more pulses available to confirm the position.

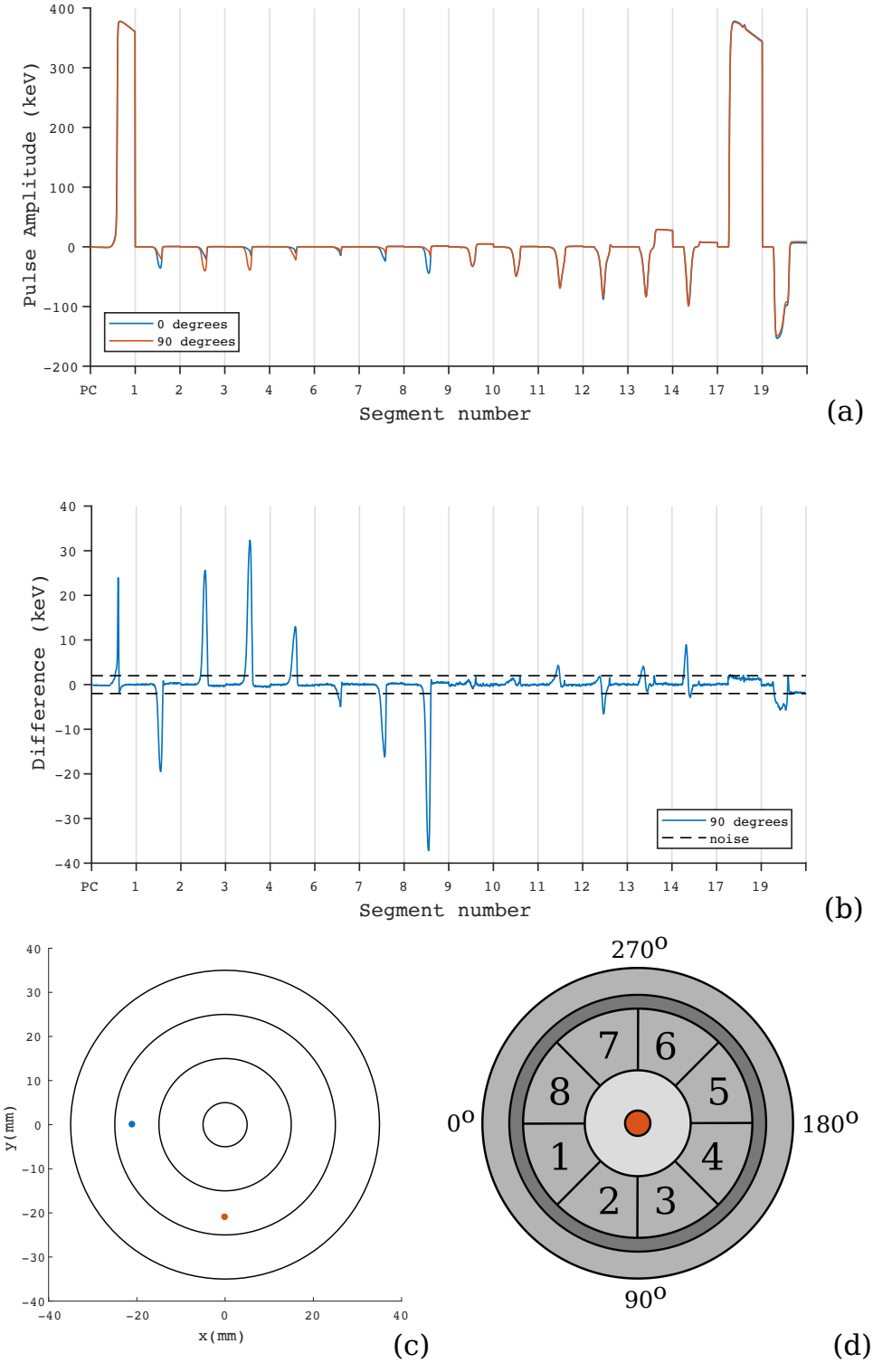


*Figure 4.16: Superpulses generated at two locations 90º apart at the same radial distance from the centre of the detector and depth (z=5.5 mm) (a). The difference between the two superpulses plotted in comparison to the maximum noise level recorded in any segment of the detector (b). The locations of the two points relative to the front face of the crystal (c) and the radial angle relative to the azimuthal segments as seen from the front of the detector (d).*

Expanding this to examine the difference in superpulses produced for gamma-ray interactions $90^o$ apart at a set depth, z, allows for examination of the symmetry of the crystal. Figure 4.17 (a) shows the difference between 5 pairs of superpulses produced at positions $90^o$ apart on the x=0 and y=0 lines. The positions relative to the crystal are shown in Figure 4.17 (b). Across all of the data sets the size and shape of the change in the signals observed on the azimuthal segments is consistent as all represent the same radial change. The differences in the point contact are all similar in shape with slight changes in magnitude based on position suggesting differing rates of change across the crystal. The size of the difference in the longitudinal segments remains small compared to the noise level and is similar across all positions. There are some small differences in shape evident in segments 17 and 19, particularly for r=21 mm, which are at least partly due to differences in the cross talk induced in the x=0 and y=0 positions. The overall similarity across all segments suggests good symmetry of the crystal. The small but consistent difference seen in the longitudinal segments is indicative of a systematic shift between the x and y axis. While this could be a small asymmetry in the crystal, it is likely to be due to the positioning error of the crystal. The position of the crystal is based on the 1 mm by 1 mm singles scan of the front face of the crystal, given the predicted sub mm position resolution of SIGMA it is likely sensitive to the error in the x and y alignment.

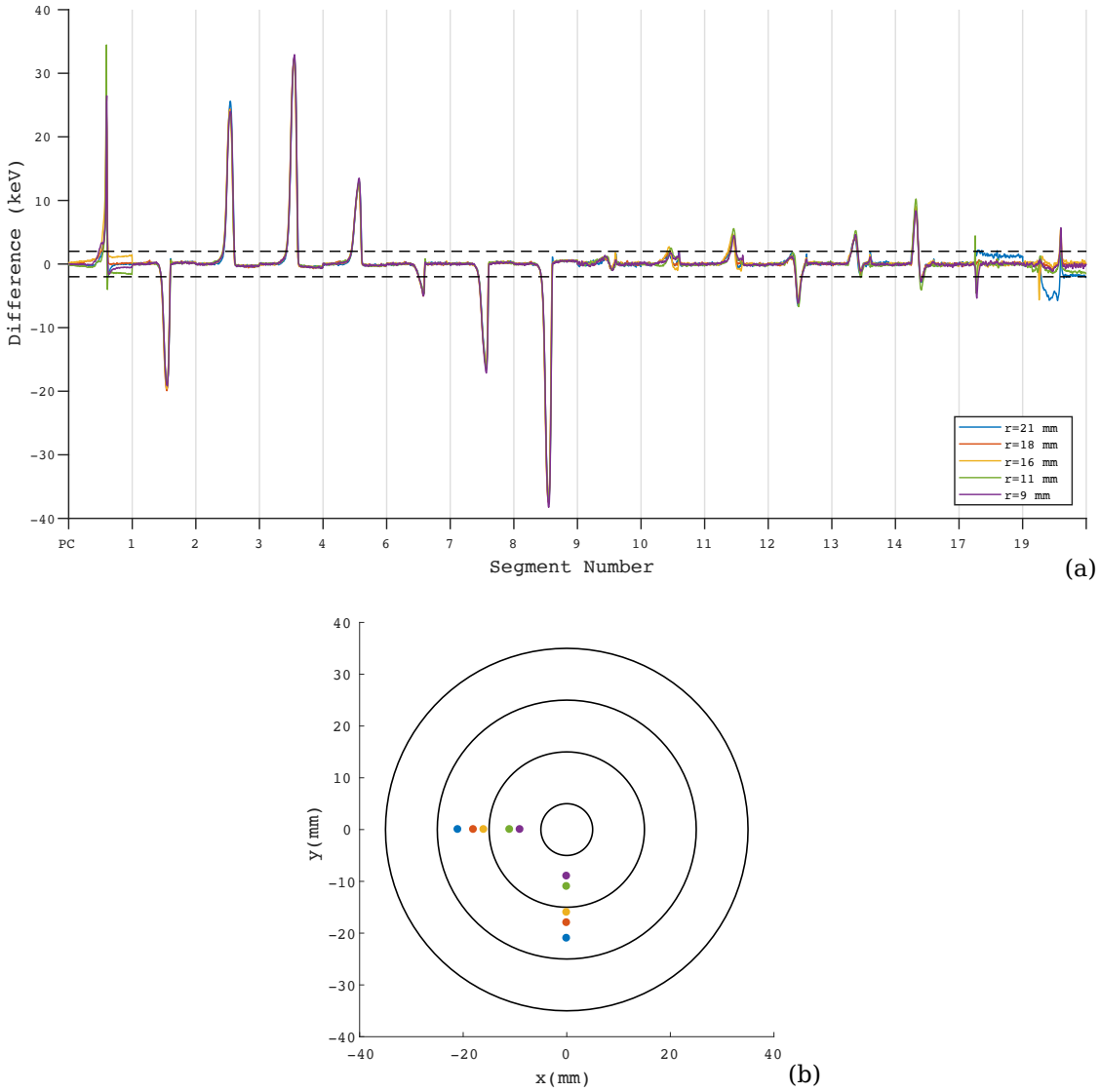


*Figure 4.17: The difference between 5 pairs of superpulses from positions at 90º from each other in the x=0 and y=0 lines (a). The positions relative to the crystal (b).*

For a set radius from the centre of the crystal, as the location of an event moves azimuthally around the crystal, the size of the image charge produced in each azimuthal segment varies in a sinusoidal pattern. An example of this is shown in Figure 4.18 for 3 of the azimuthal segments at a single depth. Using the angular definition given in Figure 4.16 (d), it is clear that the amplitude of the image charges is maximum when the event occurs directly over the active area of the segment and minimum at the other side of the crystal, when the event is furthest from that segment. Due to the sinusoidal nature of the change there are two radial locations for each amplitude of the image charge other than the maximum and minimum for each segment. This means the radial position cannot be determined by a single azimuthal pulse. As each sinusoid

is centred in a difference angular location, a second azimuthal pulse can be used to determine which radial position is correct. Figure 4.18 also shows that even at their smallest, the image charges produced in the azimuthal segments are still observable above the noise level.

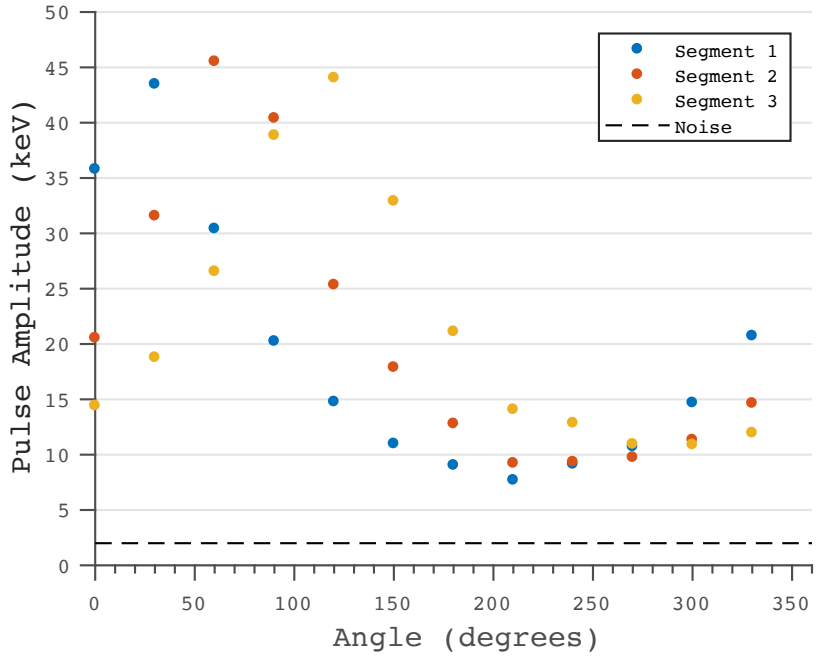


*Figure 4.18: Amplitude of the image charges in segments 1,2 and 3 as a function of angle at a depth of 4-7 mm.*

The sinusoidal variance with angle of the image charge amplitude in azimuthal segments is still seen as the depth of the gamma-ray interaction increases, provided they occur outside of the azimuthal segment charge collection area. As the depth increases eventually, near the rear of the crystal, it will reach a point where the secondary charge is collected by an azimuthal segment, at which point a real charge will be seen rather than an image charge. The amplitude of the image charges produced in Segment 3 for 3 depths are shown in Figure 4.19. A general pattern of decreasing amplitude with depth is visible though the difference in amplitude is small compared to the noise level and not consistent for all points. This suggests that the amplitude of the image charges is not enough to determine depth alone but could be used alongside other pulse information to help determine the location of an event.

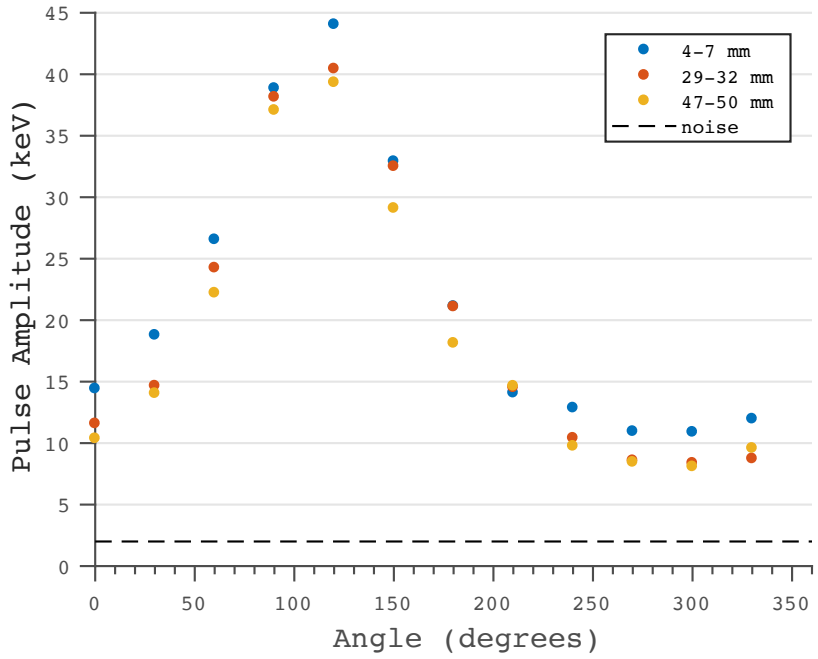


*Figure 4.19: Amplitude of the image charges produced in Segment 3 as a function of angle for 3 gamma-ray interaction depths within the crystal volume.*

## 4.5 Data Trends

The analysis of the coincidence data has highlighted several trends in the behaviour of SIGMA and the pulses created across all segments. These are described below.

- There is a measurable difference, well above the noise level, in at least two segments of the superpulse for events which occur in the same segment at a separation of 2 mm and above in a single dimension. As the difference is large enough to be observed in multiple segments this is highly suggestive that distinguishing events with a smaller separation may be possible. This is in line with the predicted sub mm position resolution for SIGMA.

- The point contact always shows a measurable difference in pulse shape above the noise level, but is never the only segment to do so and does not always show the largest change. While the point contact pulse is extremely useful for the positioning of an event, it is not the only useful pulse and all of the segment pulses should be used to achieve the best possible position resolution.

- For events which undergo the same positional change in different areas of the crystal, the size of the change in the superpulses can vary. This means the rate of change for each segment pulse varies across the crystal volume, resulting in varying levels of position resolution as predicted in the simulation [WHBB$^+$18].

- For events which occur in a single segment there is often a greater difference in the image charge induced in the neighbouring segment than in the secondary charge collecting segment itself. This means there is a greater rate of change for the image charge and that the image charge can offer greater positional information than the secondary charge collecting segment.

- The image charges produced in the azimuthal segments appear to show little change for a radial only change in position close to the front of the detector. The azimuthal segments show the greatest change in pulse shape for azimuthal and depth positional change.

- The signals from azimuthal segments show strong symmetry about the centre of the detector for the opposite azimuthal segment, confirming that all of the azimuthal segments operate in the same way. This also confirms the symmetry of the segments and the crystal.

- The signals from longitudinal segments show some small change with x and y position with the largest change being in the segments closest to the secondary charge collecting segment. The longitudinal segments show significant change with depth of the event, with increasing depth resulting in fewer image charges being produced in the longitudinal segments.

- The well contact, Segment 19, consistently shows the second largest large change behind the point contact with one dimensional change in x or y position and depth. This is partly due to the well contact running most of the length of the crystal meaning it is a neighbouring segment to all of the other segments in the crystal. This makes the well contact an important segment for positioning.

- As predicted the sensitivity of the segments to different forms of positional change varies with the segment type. Due to this no single segment can give a full picture of the position of an event. As the SIGMA segmentation scheme was designed to do, instead of one segment pulse offering 3 dimensional position resolution, the pulses from each segment are used together to form a combined picture of the event location with different segments focused on the position resolution in different dimensions of the crystal. Using this technique we get a position based on multiple pulses rather than a single pulse.

- As the change in position reduces, so does the size of the difference in the super-pulses. This highlight the need for low noise in all segments in order to achieve the greatest possible position resolution.

# 5 Discussion and Conclusions

This thesis reports on experimental characterisation measurements that have been made of the first p-type SIGMA detector. A scanning system allowing the precise placement of a collimated beam of 60 keV and 662 keV gamma rays was used to probe the crystal structure and pulse response. An array of BGO detectors and a secondary collimator were used in the scanning system to locate gamma-ray interactions in three dimensions within the crystal, information that was used to create an average pulse response for a range of selected positions.

## 5.1 Initial performance

When the SIGMA detector arrived in Liverpool in April 2018, initial analogue measurement of the energy resolution of each segment were performed to determine the intrinsic spectroscopic performance. The shaping times of the analogue spectroscopy amplifier were optimised individually to produce an energy resolution of 0.89 keV at 122 keV and 2.21 keV at 1332 keV for the point contact. The outer segments produce an average energy resolution of 1.42 keV at 122 keV and 2.62 keV at 1332 keV. These measurements comfortably passes the acceptance criteria for the detector, which is set at an average of 2 keV at 122 keV and 3 keV at 1332 keV across all segments. The only segment to fail the individual segment limits was Segment 9. An exception was made for Segment 9 as it is surrounded by the holding structure of the crystal, introducing additional noise.

The initial performance of the SIGMA detector displays better energy resolution than the comparable n-type ICPC detector of a similar geometry. The ICPC showed poor intrinsic energy resolution due to charge trapping and recombination [SCC+17]. Even with the development of an algorithm to correct for these effects, the ICPC still does not match the intrinsic energy resolution achieved by SIGMA. The superior intrinsic performance of SIGMA suggests that trapping and recombination do not have a large effect.

A signal from Segment 5 was initially observed during the first power cycle of the detector but was lost before measurements could be taken. Crosstalk was seen in Segment 13 for all events in the form of low energy mirroring of peaks. Higher energy peaks in Segment 19 displayed a double-peaking effect caused by the merging

of segments 18 and 19. The efficiency of the detector was measured as 40.9 ± 0.1 %, in agreement with the 41 % specified by the manufacturer.

## 5.2 Crystal geometry

The University of Liverpool scanning system was used to acquire SIGMA data for gamma-ray interactions at known x-y positions using collimated $^{241}$Am and $^{137}$Cs sources. The $^{241}$Am scan data acquired from the front and side of the crystal shows the position of the crystal relative to the cryostat as well as the holding structure around Segment 9. The segment boundaries are also visible as regions of increased counts indicating reduced attenuation of gamma rays which can be attributed to the contacts being thinnest at the segment boundaries. The difference in contact thickness between the segments and the boundaries was estimated from analysis of the acquired data to be between 180 - 350 $\mu$m. The active area of the visible segments was also measured along with the dimensions of the full crystal. The longitudinal segments each measured 10.0 ± 0.7 mm in width, with the full height of the crystal being 79.0 ± 0.9 mm; close to the 80 mm specified by the manufacturer. The rear width of the crystal was measured as 70.0 ± 0.7 mm and the front width as 47.0 ± 0.7 mm. When compared to the initial design, only the front face of the crystal shows a significant change from the 49 mm specified, suggesting the loss of mass due to crystal reprocessing is mostly from the front face and is not uniform as initially assumed. The $^{241}$Am scan data was also used to produce a risetime matrix examining the differences in risetime across the front face of the crystal.

The $^{137}$Cs singles scanning allowed for the crystal to be probed at depth. This allowed the active area of the azimuthal segments to be investigated. By determining the sensitive regions represented by the longitudinal segments, an indication of the change in the well contact with depth was developed. Slices, showing the counts per position, through the centre of the detector in both x and y were used to confirm the symmetry of the crystal. The point contact scan data was used to create a coordinate system for the crystal relative to the scanning table, which was a foundation step in the acquisition of coincidence data. Two methods of fold calculation were assessed for identifying single interactions. During the fold analysis crosstalk was identified in segments 9 and 14 in addition to Segment 13.

## 5.3 Coincidence Data

The same scanning system used for the singles scanning measurements was also used to acquire coincidence data using a collimated $^{137}$Cs source. A secondary lead collimator was employed to only allow gamma rays that scattered at 90$^o$ in the SIGMA crystal at pre selected heights to enter one of 32 BGO detectors surrounding the SIGMA detector.

Data were collected for a total of 680 individual x-y-z gamma-ray positions, in radial and linear patterns, to investigate the response of the crystal across all segments. By forming a superpulse of the average response at a single gamma-ray interaction location across all of the active segments, comparison of the response at different locations could be made. The symmetry of the crystal was investigated using this method. The reflection observed in the pulse height of opposing azimuthal segments as the interaction position moves across the centre of the crystal indicates good symmetry at the rear of the crystal and between the azimuthal segments. Comparison of the x=0 and y=0 line data also revealed good symmetry of the crystal in the x and y planes. A small systematic shift was identified in the longitudinal segments but this is likely to be due to the high position sensitivity of the detector compared to the error in the positioning of the crystal.

A measurable difference above the noise level of the segments in the pulse response, for locations with a separation of 2 mm in one dimension was seen. The difference was large enough to suggest that differentiation of pulses with an even smaller separation could be made, potentially down to the sub mm position resolution predicted by simulation for the SIGMA detector. The difference in superpulse shape was seen in the point contact and at least one other segment, highlighting the importance of the use of the full superpulse. When examining the difference in pulse shapes for events in a single segment, the image charge produced in a neighbouring segment often shows a greater change than the secondary charge collecting segment. As Segment 19 (the well contact) runs most of the length of the crystal, it is a neighbouring segment to all of the other segments in the crystal making it particularly important for positioning. For events with the same spatial difference in a single dimension, in different locations of the detector, different levels of change are seen across the full superpulse. This suggests there are different rates of change for the pulse shape in each segment and as such the position resolution achievable varies across the crystal volume.

The change in pulse shape with position for the segments showed a strong correlation with the segment type. As expected, the azimuthal segments were particularly sensitive to radial change and the longitudinal segments more sensitive to depth. This was part of the SIGMA segmentation design, to gain different positioning information from different segments. Only by using the pulses from all of the segments can a full picture of the location of an interaction be deduced, meaning all segments must be active and operational for SIGMA to work at peak positioning performance. The level of difference seen between superpulses reduces the closer the events occur to one another and so the smaller the separation in drift time between events. To achieve the best position resolution the noise level needs to be as low as possible across all segments to identify the small differences seen in multiple segments.

## 5.4 Future Uses

As a large volume HPGe detector offering improved energy and position resolution over other detectors of this type, there are many potential future uses for the SIGMA detector. The small size of the point contact offers low noise and excellent energy resolution, particularly at low energies. This makes SIGMA appropriate for applications requiring good energy discrimination including background rejection [DRQ+10]. The large volume offers good efficiency with fewer readout channels and less complexity than other segmented detectors. The combination of excellent energy and position resolution makes SIGMA ideal as a tracking detector, this matched with the large volume also offers the possibility of use as a single crystal Compton camera. All of these factors mean SIGMA could have a role in a wide range of experimental, medical, industrial and security applications.

One of the main proposed application for SIGMA is as the third phase of DEGAS, as part of the DESPEC experiment [FAI18b]. While the first two phases of DEGAS have been designated as EUROBALL and AGATA type detectors respectively, the third phase of DEGAS is still under consideration and will focus on a long-term development program of a novel detector. The future aim for SIGMA is to prove its viability for this role by meeting the requirements laid out in[DEG14]. This work has shown that the first SIGMA prototype detector does not meet the energy resolution requirement of 2.0 keV at 1332 keV for the third phase but is close at 2.21 keV at 1332 keV. As the first detector of its kind, it would be expected that small improvements will be made with successive models and, with the gap being so small, SIGMA could achieve the required performance.

## 5.5 Future Work

This work has concentrated on the first experimental characterisation of a novel prototype detector. There is still much work to be done with SIGMA to determine its full potential for gamma-ray tracking and imaging applications. This section will discuss some of the next steps to be taken and identifies areas of future work with SIGMA.

### 5.5.1 Electrical issues

For this particular SIGMA crystal, there are several electrical contacting issues which is to be expected at this stage of detector prototyping. In discussions with the manufacturer, they have expressed an interest in attempting to fix some of these issues. When the detector first arrived in Liverpool a signal was seen in Segment 5 and the noise levels in segments 15 and 16 were low. This means the loss of signal and the increase in noise, observed in these segments following the movement of the detector, are likely to be electrical issues rather than a problem with the crystal. The crosstalk

in segments 9, 13 and 14 could also be lessened or removed by increasing the distance between the wires in the cryostat or by shielding the wires from one another [San07].

### 5.5.2 Comparison to Simulation

Work is currently ongoing to produce a simulation of the SIGMA detector using the AGATA Detector Library (ADL) [BBR16]. Comparison of the experimental pulses to the simulated pulses from the same locations can now begin. This comparison will highlight aspects of the simulation which can be amended by small parameter changes, such as electron and hole mobility, to bring the simulation into good agreement with the experimental data [Col13]. Once this is achieved and the simulation has been validated, the pulse shapes for all locations within the crystal can be calculated, creating a simulated pulse shape database for PSA. Using PSA, the position resolution can be assessed across all areas of the crystal by examining the rate of change in pulse shape with position.

### 5.5.3 Crosstalk Correction

In order to gain a full understanding of the pulse shapes created by the SIGMA detector crosstalk corrections must be made. There are two known types of crosstalk which can occur in segmented HPGe detectors, proportional and differential. Proportional crosstalk describes energy from a hit segment being passed to another segment, resulting in a loss of energy in the hit segment and energy collected in an additional segment. While the loss in energy in the hit segment is mostly corrected for by the gain matching of the segments, it can become an issue at higher folds where energy is summed over multiple segments. This form of crosstalk can be effectively corrected for by observing the baseline shifts in none hit segments, or by measuring the energy deposited in fold 2 events as discussed in [BRW$^+$09]. At present proportional crosstalk has been identified in SIGMA in segments 9, 13 and 14, as discussed in Sections 2.5 and 3.6.

Differential crosstalk describes the induction of a signal in a segment proportional to the differential of the signal in a hit segment. This is harder to identify than proportional crosstalk as it is transient, resulting in no residual charge being collected in the effected segments. While it does not effect the measured energy of the hit segment, it does effect the pulse shapes produced. In order to use PSA to its full ability in the positioning of events, the differential crosstalk needs to be quantified and corrected for as described in [BRP06].

### 5.5.4 Compton Imaging

When a gamma ray scatters before being fully absorbed in a detector, the Compton scattering equation can be used to predict the angle of scatter based on the energies deposited in the detector, as described in [Sei10]. While this is often achieved with

2 separate detectors, an absorber and scatterer, Compton imaging can also be performed with a single large volume detector, if it is possible to separate the gamma-ray interaction locations [MAB+11]. Compton imaging relies on the measured energies of the two interactions as well their positions, as such the better the energy and position resolution of the detector, the more accurately a source can be located. As a large volume HPGe detector with excellent energy resolution and, once a simulation has been verified, excellent position resolution using PSA, SIGMA has the potential for use as a single crystal Compton camera.

Data has been taken for the assessment of SIGMAs ability to position sources using Compton imaging. This includes multiple sources of different energy, at a selection of distances from both the other sources and the SIGMA detector. A mix of point sources and line sources were used. Sources were also placed at a range of positions relative to the detector, including in line with the front face and at the side of the detector. Once PSA is available for SIGMA, this data can be analysed to assess SIGMAs performance in locating source positions, determining source geometry, using energy gating to differentiate sources and determining the effectiveness of Compton imaging relative to the crystal orientation.

### 5.5.5 Tracking Algorithm Assessment

It is often the case that only events which deposit their full energy in the detector are of interest. Selection of these events can be achieved by gating on the energy deposited in a single interaction, though this greatly reduces the number of accepted events as many gamma rays scatter before being fully absorbed, particularly at higher energies. If the gamma rays of interest are low in abundance it is advantageous to be able to use as many events as possible. Gamma-ray tracking algorithms are designed to reconstruct the path of a single gamma ray through scattering and absorption to allow the full energy for the event to be reconstructed, leading to a much greater number of retained events. Two of the most popular gamma-ray tracking methods, forward tracking [DDLM10] and backtracking [vdMC02], use the Compton scattering equation to determine the most probable path for a gamma ray.

The improved energy and position resolution of SIGMA over other large volume HPGe detectors means that Compton scattering based tracking algorithms should perform better with SIGMA. To determine which tracking algorithms offer the best performance for SIGMA, the validated SIGMA simulation will be used to test existing algorithms and assist in parameter optimisation. This work will be used to determine the most effective current tracking algorithm for use with the SIGMA detector, and may highlight the need for a new tracking algorithm to be designed specifically for SIGMA.

### 5.5.6 Array Design

With a validated simulation, work can begin to design an array of SIGMA detectors for nuclear structure physics experiments such as DESPEC at FAIR, GSI. This will involve the design of spherical and cubic arrays with a set internal radius based on the experimental requirements. Design will focus on the optimisation of array efficiency and solid angle coverage, as well as the testing of tracking algorithms across multiple detectors. In future, multiple SIGMA detectors may be produced to allow experimental measurements to be taken with a small array of detectors and validate this area of simulation.

# Bibliography

[A+12] S. Akkoyun et al. Agata-advanced gamma tracking array. *Nuclear Instruments and Methods in Physics Research A*, 668:26–58, 2012.

[AME20] AMETEK Inc. *MAESTRO Multichannel Analyzer Emulation Software*, 2020 (Accessed 09/11/20). https://www.ortec-online.com/products/application-software/maestro-mca.

[BBR16] B. Bruyneel, B. Birkenbach, and P. Reiter. Pulse shape analysis and position determination in segmented hpge detectors: The agata detector library. *The European Physical Journal A*, 52(70), 2016.

[BNL+17] T.D. Bucher, S.P. Noncolela, E.A. Lawrie, T.R.S. Dinoko, J.L. Easton, N. Erasmus, J.J. Lawrie, S.H. Mthembu, W.X. Mtshali, O. Shirinda, and J.N. Orce. Proportional crosstalk correction for the segmented clover at ithemba labs. *Physica Scripta*, 92(11), October 2017.

[BRP06] B. Bruyneel, P. Reiter, and G. Pascovici. Characterisation of large volume hpge detectors. part ii: Experimental results. *Nuclear Instruments and Methods in Physics Research A*, 569:774–789, December 2006.

[BRW+09] B. Bruyneel, P. Reiter, A. Wiens, J. Eberth, H. Hess, G. Pascovici, N. Warr, S. Aydin, D. Bazzacco, and F. Recchia. Crosstalk corrections for improved energy resolution with highly segmented hpge-detectors. *Nuclear Instruments and Methods in Physics Research A*, 608:99–106, 2009.

[Cha67] G.T. Chapman. Gamma-ray attenuation coefficients for germanium. *Nuclear Instruments and Methods*, 52:101–103, 1967.

[Col13] S. J. Colosimo. *The Characterisation of AGATA High Purity Germanium Detectors for Pulse Shape Analysis.* PhD thesis, University of Liverpool, Oliver Lodge Laboratory, 2013.

[CRHL11] R.J. Cooper, D.C. Radford, P.A. Hausladen, and K. Lagergren. A novel hpge detector for gamma-ray tracking and imaging. *Nuclear Instruments and Methods in Physics Research A*, 665:25–32, 2011.

[DBB+10] D. Darrientos, A.J. Boston, H.C. Boston, B. Quintana, I.C. Sagrado, C. Unsworth, S. Moon, and J.R. Cresswell. Characterisation of a broad energy germanium (bege) detector. *Nuclear Instruments and Methods in Physics Research A*, 648:228–231, August 2010.

[DCG+17] M. Doncel, B. Cederwall, A. Gadea, J. Gerl, Kojouharov, S. Martin, R. Palit, and B. Quintana. Performance and imaging capabilities of the degas high resolution gamma ray detector array for the despec experiment at fair. *Nuclear Instruments and Methods in Physics Research A*, 873:36–38, November 2017.

[DCM+15] M. Doncel, B. Cederwall, S. Martin, B. Quintana, A. Gadea, E. Farnea, and A. Algora. Conceptual design of a high resolution ge array with tracking and imaging capabilities for the despec (fair) experiment. *IOP science*, 2015.

[DDLM10] F. Didierjean, G. Duchene, and A. Lopez-Martens. The deterministic annealing filter: A new clustering method for gamma-ray tracking algorithms. *Nuclear Instruments and Methods in Physics Research A*, 615:188–200, 2010.

[DEG14] Technical report for the design, construction and commissioning of the despec germanium array spectrometer - degas. Technical report, FAIR PAC NUSTAR, 2014.

[DRQ+10] M. Doncel, F. Recchia, B. Quintana, A. Gadea, and E. Farnea. Experimental test of the background rejection, through imaging capability, of a highly segmented agata germanium detector. *Nuclear Instruments and Methods in Physics Research A*, 622:614–618, October 2010.

[Eva55] R.D. Evans. *The Atomic Nucleus*. Tata McGraw-Hill Publishing Company Ltd, 1955.

[FAI18a] FAIR. *FAIR - Facility for Antiproton and Ion Research in Europe*, 2018 (Accessed 30/01/18). http://www.fair-center.eu.

[FAI18b] FAIR. *HISPEC (HIgh-Resolution In-flight SPECtroscopy)/DESPEC (DEcay SPECtroscopy)*, 2018 (Accessed 31/01/18). http://www.fair-center.eu/for-users/experiments/nustar/experiments/hispecdespec.html.

[G+03] H. Geissel et al. The super-frs project at gsi. *Nuclear Instruments and Methods in Physics Research B*, 204:71–85, 2003.

[GGL94] A. Georgiev, W. Gast, and R.M. Lieder. An analog-to-digital conversion based on a moving window deconvolution. *IEEE Transactions on Nuclear Science*, 41:1116–1124, Aug 1994.

[He01] Z. He. Review of the shockley-ramo theorem and its application in semiconductor gamma-ray detectors. *Nuclear Instruments and Methods in Physics Research A*, 463:250–267, 2001.

[IEE96] Ieee standard test procedures for germanium gamma-ray detectors. *IEEE Std 325-1996*, 1996.

[Jud19] D. Judson. *Nuclear Physics Research Group Software, MTsort Sorting Program*, (Accessed 13/11/19). http://ns.ph.liv.ac.uk/software.html.

[Kno10] G.F. Knoll. *Radiation Detection and Measurement*. John Wiley & Sons, Inc., 4th edition, 2010.

[Koh12] A. Kohler. No more breaks for electrons. *Nature Materials*, 11:836–837, 2012.

[Lee90] I.-Y. Lee. The gammasphere. *Nuclear Physics A*, 520:c641–c655, 1990.

[Leo94] W.R. Leo. *Techniques for Nuclear and Particle Physics Experiments*. Springer-Verlag Berlin Heidelberg GmbH, 1994.

[LMHK+04] A. Lopez-Martens, K. Hauschild, A. Korichi, J. Roccaz, and J-P. Thibaud. $\gamma$-ray tracking algorithms: a comparison. *Nuclear Instruments and Methods in Physics Research A*, 533:454–466, 2004.

[MAB+11] S. Moon, B.Q. Arnes, A.J. Boston, H.C. Boston, J.R. Cresswell, T. Davinson, A. Gadea, L.J. Harkness, D.S. Judson, I. Lazarus, P.J. Nolan, R.D. Page, A.H. Prieto, and J. Simpson. Compton imaging with agata and smartpet for despec. *Journal of Instrumentation*, 6, December 2011.

[MGL+00] L. Mihailescu, W. Gast, R.M. Lieder, H. Brands, and H. Jager. The influence of anisotropic electron drift velocity on the signal shapes of closed-end hpge detectors. *Nuclear Instruments and Methods in Physics Research A*, 447:350–360, 2000.

[Mir20] Mirion Technologise Inc. *Mirion Technologies*, 2020 (Accessed 09/11/20). https://www.mirion.com/.

[MIR18] MIRION Technologies (CANBERRA). *User Manual EGPC 70x80 SEG19 SIGMA*, April 2018.

[Nuc19] Nuclear Physics Group, Science and Technology Facilities Council. *Welcome to MIDAS the Multi Instance Data Acquisition System*, (Accessed 13/11/19). http://npg.dl.ac.uk/MIDAS/.

[R+21] D.C. Radford et al. *SigGen and FieldGen software*, (Accessed 01/03/21). https://github.com/radforddc/icpc_siggen.

[Rad18] D.C. Radford. *Notes on the use of the program gf3*, 2000 (Accessed 28/11/18). https://radware.phy.ornl.gov/gf3/.

[Rub06] B. Rubio. Decay spectroscopy (despec) at the new fair-nustar facility. *International Journal of Modern Physics E*, 15, 2006.

[S+11] P.-A. Söderström et al. Interaction position resolution simulations and in-beam measurements of the AGATA HPGe detectors. *Nuclear Instruments and Methods in Physics Research A*, 638:96–109, 2011.

[San07] Stephen Sangwine. *Electronic Components and Technology*. CRC Press, third edition edition, 2007.

[SCC+17] M. Salathe, R.J. Cooper, H.L. Crawford, D.C. Radford, J.M. Allmond, C.M. Campbell, R.M. Clark, M. Cromaz, P. Fallon, P.A. Hausladen, M.D. Jones, A.O. Macchiavelli, and J.P. Wright. Energy reconstruction of an n-type segmented inverted coaxial point-contact hpge detector. *Nuclear Instruments and Methods in Physics Research A*, 868:19–26, 2017.

[Sei10] Carolyn E. Seifert. *Semiconductor Radiation Detector Systems, Chapter 13 Compton Imaging: Principles and Practice*. CRC Press, 2010.

[Sim97] J. Simpson. The euroball spectrometer. *Zeitschrift für Physik*, 358:139–143, 1997.

[TL15] N. Tsoulfanidis and S. Landsberger. *Measurement and Detection of Radiation*. CRC Press, 4th edition, 2015.

[vdMC99] J. van der Marel and B. Cederwall. Backtracking as a way to reconstruct compton scattered $\gamma$-rays. *Nuclear Instruments and Methods in Physics Research A*, 437:538–551, 1999.

[vdMC02] J. van der Marel and B. Cederwall. $\gamma$-ray tracking in germanium: the backtracking method. *Nuclear Instruments and Methods in Physics Research A*, 477:391–396, 2002.

[WHBB+18] J.P. Wright, L.J. Harkness-Brennan, A.J. Boston, D.S. Judson, M. Labiche, P.J. Nolan, R.D. Page, F. Pearce, D.C. Radford, J. Simpson,

and C. Unsworth. Position resolution simulations for the inverted-coaxial germanium detector, sigma. *Nuclear Instruments and Methods in Physics Research A*, 892:84–92, June 2018.